

# Marshall Plan Research Paper

## Shallow Water Bathymetry with Single and Multi-view Photogrammetry Unmanned Aerial Systems

### Autor

Ing. Erik Frühwirth, BSc.

### Registration number

1810362002

### Spatial Information Management

Carinthia University of Applied Sciences

School of Engineering & IT

Department of Geoinformation & Environmental Technologies

### Supervisors

FH-Prof. Mag. Dr. Gernot Paulus, MSc, MAS, Department of Geoinformation and Environmental Technologies, Carinthia University of Applied Sciences, Villach, Austria

FH-Prof. Dr.-Ing. Karl-Heinrich Anders, Department of Geoinformation and Environmental Technologies, Carinthia University of Applied Sciences, Villach, Austria

Prof. Dr. Douglas (Doug) Stow, Department of Geography, San Diego State University, San Diego, USA

## **Abstract**

Using photogrammetry for shallow water bathymetry can reduce the costs for data collection. Finding a way to reduce errors caused by light refraction occurring during the transition between air and water is necessary to produce valid bathymetric height data. To achieve refraction correction, already different approaches exist. Although their quality and applicability have to be further tested. In this work, one approach using an iterative, camera orientation and point cloud based algorithm and three approaches using bathymetric scaling were applied to four different SfM data sets.

Three refraction correction techniques are DSM-based and tackle the reflection problem with a refraction index, factor, or linear regression function. The index is based on the calculated value at 90° nadir position and clear water as the second medium. While no additional data is needed for the explained approach, the refraction correction factor and the regression correction function is derived from extra measured underwater reference points.

One refraction correction uses the extra information of the camera orientation and does the correction directly on the point cloud via a Python script.

Further, this work also inspects if different image acquisition methods can improve the process and the produced result. Therefore, two different sensor systems were used to conduct a field experiment. For one dataset a Sony Alpha 7RIII was used to capture nadir images. The other data set was captured with a Pentacam, which consists of five camera sensors taking pictures simultaneously. One is mounted in nadir position while the other four take images in an oblique view. This gives the possibility to create different data compositions consisting of a combination of both view angles, only nadir images or only images taken in an oblique angle.

The theoretical calculations show the importance of considering the camera's view angle for the refraction correction process. This information can then be used to select a better fitting correction factor than the clear water index and to optimize the Multiview camera setup. The use of oblique images requires further reference data or adjustments in the iterative refraction correction method via Python script. The final outcome from this refraction correction technique proved to be the best result of our examination.

# Table of content

<b>1. Introduction</b>	<b>1</b>
1.1. Motivation	2
1.2. Problem Statement / Research Question	2
1.3. Methodological considerations	4
1.4. Expected Results	5
1.5. Structure of this thesis	6
<b>2. Theoretical Background</b>	<b>7</b>
2.1. Theoretical background SfM Photogrammetry	7
2.2. Two Media Photogrammetry	8
2.2.1. Theoretical background Two Media SfM Photogrammetry for bathymetry	8
2.2.2. Refraction correction with clear water refraction index	10
2.2.3. Empirical refraction correction with reference points	11
2.2.4. Multi-View refraction correction (pyBathySfM)	12
2.2.5. Refraction correction with machine learning	12
2.3. Airborne laser scanning (Lidar)	13
2.4. Low-cost 3D Scanner	14
2.5. Echo sounding	14
2.6. Spectral-depth relationship	15
2.7. Overview and Best practice	16
<b>3. Approach</b>	<b>18</b>
3.1. Conceptual workflow structure	18
3.2. Data capture	19
3.2.1. UAS	19
3.2.2. DGNS point measurements	22
3.3. Photogrammetric processing	23
3.3.1. Image selection and SfM processing	23
3.3.2. Sensor combinations and Outputs	24
3.4. Refraction correction	24
3.4.1. Considerations of the Influence of camera angles on refraction	24
3.4.2. Iterative camera orientation and point cloud based developed by (Dietrich 2017a)	28
3.4.3. Bathymetric scaling for refraction correction on DSM's	29

3.5. Comparison and validation .....	29
3.6. Software and Hardware .....	30
<b>4. Project area .....</b>	<b>32</b>
4.1. Lidar Data .....	33
<b>5. Project Implementation .....</b>	<b>34</b>
5.1. Data preparation .....	34
5.1.1. Images .....	34
5.1.2. GCP's / DGNSS-points categorization.....	34
5.2. Data processing .....	36
5.2.1. SfM processing .....	36
5.2.2. Water surface elevation .....	39
5.2.3. Extracting DEM height-information at DGNSS Points.....	40
5.2.4. Application of the clear water refraction index and refraction factor....	40
5.2.5. Empirical correction with a linear equation.....	42
5.2.6. Multi-View refraction correction (pyBathySfM) .....	44
5.2.7. Empirical error statistic.....	46
5.2.8. Comparison of the different DSM's .....	46
5.2.9. Comparison with the Lidar data .....	47
<b>6. Results .....</b>	<b>48</b>
6.1. Captured Data .....	48
6.1.1. UAV captured images.....	48
6.1.2. DGNSS measured points.....	49
6.1.3. Raw SfM data and GCP point comparison .....	49
6.1.4. Water surface height.....	50
6.2. SfM evaluation .....	51
6.2.1. Orthomosaic .....	53
6.2.2. 3D Point clouds.....	55
6.2.3. Digital Surface Model.....	56
6.3. SfM refraction correction.....	57
6.4. DSM data comparison .....	62
6.5. Lidar data comparison .....	66
<b>7. Discussion.....</b>	<b>68</b>
7.1. Refraction influence on our UAS image capturing setup .....	68
7.2. Field data acquisition .....	68

7.3. Data preparation .....	69
7.4. SfM Data processing and refraction correction .....	69
7.5. Benefit of the two different camera setups.....	70
<b>8. Conclusion and Further Work.....</b>	<b>72</b>
<b>Appendix A: Orthomosaic .....</b>	<b>82</b>
<b>Appendix B: SfM water depth DSM uncorrected .....</b>	<b>86</b>
<b>Appendix C: SfM DSM uncorrected comparison.....</b>	<b>91</b>
<b>Appendix D: Comparison of SfM DSM refraction corrected and uncorrected</b> <b>95</b>	
<b>Appendix E: SfM DSM refraction corrected sensor comparison .....</b>	<b>105</b>
<b>Appendix F: Comparison, SfM data with Lidar data .....</b>	<b>110</b>
<b>Appendix G: Error histogram and scatterplot.....</b>	<b>113</b>
<b>Appendix H: Agisoft Metashape Professional Report SN .....</b>	<b>120</b>
<b>Appendix I: Agisoft Metashape Professional Report PA .....</b>	<b>128</b>
<b>Appendix J: Agisoft Metashape Professional Report PN .....</b>	<b>136</b>
<b>Appendix K: Agisoft Metashape Professional Report PO .....</b>	<b>144</b>

## List of Figures

Figure 1: Overview of Project Workflow .....	4
Figure 2: Left: Stereo Photogrammetry with a single stereo pair of photographs (b: intra-axial distance), Right: Multi-view stereophotogrammetry (SfM) with multiple, overlapping photographs (Luhmann 2003, pp. 104–105).....	8
Figure 3: Trigonometry of the refraction angles for a single point/camera combination. Own modification (Dietrich 2017a, p. 2, Figure 1, Table 1) .....	9
Figure 4: Different refraction effect of visible light during the transition from air to water (own illustration).....	10
Figure 5: Examples of used wavelength for Lidar (Teledyne optech 2020).....	13
Figure 6: Using: (a) single beam and (b) multibeam (Church et al. 2012, p. 319, Figure 24.2).....	14
Figure 7: Left: The electromagnetic spectrum and atmospheric transmittance with typical spectral sectors for different sensors, right: The acoustic spectrum with typical acoustic sector for echo sounding. Own modification (Albertz and Wiggenghagen 2009, p. 69).....	16
Figure 8: Conceptual workflow structure (own illustration) .....	18
Figure 9: Leica Hexa Copter AX20 with a mounted Leica GS18 RTK and Sony Alpha 7RIII, Left: ready for take-off. Right: during data acquisition with the camera in nadir position (own images) .....	19
Figure 10: Calculated footprint of the estimated camera directions by Agisoft Metashape Professional captured with the five sensors on the Pentacam during one trigger event at a flight height of 89,79m above watersurface (own illustration) .....	20
Figure 11: Illustration of the different overlap possibilities (own illustration) .....	21
Figure 12: Refraction effect at 80m flight altitude and 1m water depth (own illustration) .....	25
Figure 13: Sketch to represent the nine calculated points at nadir view (own illustration) .....	26

Figure 14: Sketch to represent the nine calculated points for 25° off-nadir view, left: horizontal sensor position, right: vertical sensor position (own illustration).....	26
Figure 15: Overview of lake Weissensee (Amt der Kärntner Landesregierung 2020) .....	32
Figure 16: Orthomosaic Weissensee, shallow east shore and deeper water body (Amt der Kärntner Landesregierung 2020) .....	33
Figure 17: Orthophoto of the SN dataset with the classification of the DGNS measured points (own illustration).....	35
Figure 18: SN footprint with labeled footprint size and overlap (Background SN Orthomosaic, SN =Sony Nadir) (own illustration).....	38
Figure 19: PN footprint with labeled footprint size and overlap (Background PN Orthomosaic, PN =Pentacam Nadir) (own illustration).....	39
Figure 20: Illustration of the refraction correction model with clear water index in the ArcMap ModelBuilder (own illustration).....	41
Figure 21: Illustration of the refraction correction model with individual factor in the ArcMap ModelBuilder (own illustration).....	42
Figure 22: Linear regression function for the different data sets, (SN =Sony Nadir, PA= Pentacam All, PN= Pentacam Nadir, PO =Pentacam Oblique).....	43
Figure 23: Illustration of the refraction correction model with the regression function in the ArcMap ModelBuilder (own illustration).....	44
Figure 24: Uncorrected SfM derived heights compared to GCP heights (own illustration).....	50
Figure 25: Camera location and image overlap Agisoft Metashape Professional Report, left SN.....	51
Figure 26: Sections of the orthomosaic from the four data sets: a) SN =Sony Nadir, b) PA= Pentacam All, c) PN= Pentacam Nadir, d) PO =Pentacam Oblique (own illustration).....	53
Figure 27: Detailed image section of one Ground Control Point plate (1mx1m) represented in an orthomosaic for each data set with a 2cm/pixel resolution (own	

illustration), (SN =Sony Nadir, PA= Pentacam All, PN= Pentacam Nadir, PO =Pentacam Oblique) .....	55
Figure 28: Sections of the water depth height SfM DSM from the four data sets: a) SN =Sony Nadir, b) PA= Pentacam All, c) PN= Pentacam Nadir, d) PO =Pentacam Oblique (own illustration).....	57
Figure 29: Error histograms and scatterplots for all four datasets corrected with the calculated factor (SN =Sony Nadir, PA= Pentacam All, PN= Pentacam Nadir, PO =Pentacam Oblique) (own illustration) .....	60
Figure 30: Error histograms and scatterplots for the PA=Pentacam All datasets corrected with the four different correction methods (own illustration) .....	61
Figure 31: Sections of Pentacam refraction corrected DSMs minus Pentacam uncorrected DSMs a) PN clear water index corrected – PN uncorrected, b) PA derived factor corrected – PA uncorrected c) PA regression function corrected – PA uncorrected d) PO iterative Python script (index = 1,4) corrected - PO uncorrected (PA= Pentacam All, PN= Pentacam Nadir, PO =Pentacam Oblique, CWI = clearwater index, CF = calculated factor, LRF= linear regression function, PS 1,4 = Python script with refraction factor 1,4) (own illustration).....	63
Figure 32: Sections of: a) SN clear water index corrected – SN uncorrected, b) SN factor corrected – SN uncorrected c) SN regression function corrected – SN uncorrected, d) SN iterative Python script corrected - SN uncorrected (SN= Sony Nadir, CWI = clearwater index, CF = calculated factor, LRF= linear regression function, PS CWI= Python script with clearwater index) (own illustration) .....	64
Figure 33: Sections of sensor comparison for different refraction approaches: a) Sony Nadir DSM minus Pentacam Nadir both corrected via clearwater index, b) Sony Nadir DSM minus Pentacam All both corrected via linear regression function derived from underwater reference points (SN= Sony Nadir, PA= Pentacam All, CWI = clearwater index, LRF= linear regression function) (own illustration).....	65
Figure 34: Lidar DEM height offset corrected(1,3m) minus a) SfM Sony Nadir derived factor corrected DSM b) SfM Pentacam all derived factor corrected DSM (SN= Sony Nadir, PA= Pentacam All, CF = calculated factor) (own illustration).....	67

Figure 35: Sony nadir Orthomosaic (own Illustration).....	82
Figure 36:Pentacam all images orthomosaic (own Illustration) .....	83
Figure 37: Pentacam nadir orthomosaic (own illustration).....	84
Figure 38: Pentacam Oblique Orthomosaic (own illustration) .....	85
Figure 39: Water depth Sony Nadir DSM uncorrected (own illustration with hillshade effect).....	87
Figure 40: Water depth Pentacam All DSM uncorrected (own illustration with hillshade effect).....	88
Figure 41: Water depth Pentacam Nadir DSM uncorrected (own illustration with hillshade effect) .....	89
Figure 42: Water depth Pentacam Oblique DSM uncorrected (own illustration with hillshade effect) .....	90
Figure 43: Sony Nadir DSM minus Pentacam all DSM both uncorrected (own illustration).....	92
Figure 44:Sony Nadir DSM minus Pentacam nadir DSM both uncorrected (own illustration).....	93
Figure 45:Sony Nadir DSM minus Pentacam oblique DSM both uncorrected (own illustration).....	94
Figure 46: Pentacam Nadir clear water index corrected DSM minus Pentacam Nadir uncorrected DSM (own illustration) .....	96
Figure 47: Pentacam All derived factor corrected DSM minus Pentacam All uncorrected DSM (own illustration) .....	97
Figure 48: Pentacam All linear regression function corrected DSM minus Pentacam All uncorrected DSM (own illustration) .....	98
Figure 49: Pentacam Oblique iterative Python script (index = 1,337) corrected DSM minus Pentacam Nadir uncorrected DSM (own illustration) .....	99
Figure 50: Pentacam Oblique iterative Python script (index = 1,4) corrected DSM minus Pentacam Nadir uncorrected DSM (own illustration) .....	100

Figure 51: Sony Nadir clear water index corrected DSM minus Sony Nadir uncorrected DSM (own illustration) .....	101
Figure 52: Sony Nadir derived factor corrected DSM minus Sony Nadir uncorrected DSM (own illustration) .....	102
Figure 53: Sony Nadir linear regression function corrected DSM minus Sony Nadir uncorrected DSM (own illustration) .....	103
Figure 54: Sony Nadir iterative Python script corrected DSM minus Sony Nadir uncorrected DSM (own illustration) .....	104
Figure 55: Sony Nadir DSM minus Pentacam Nadir both corrected via clearwater index (own illustration) .....	106
Figure 56: Sony Nadir DSM minus Pentacam All both corrected via derived factor from underwater reference points (own illustration) .....	107
Figure 57: Sony Nadir DSM minus Pentacam All both corrected via linear regression function derived from underwater reference points (own illustration) .....	108
Figure 58: Sony Nadir DSM minus Pentacam Oblique both corrected via iterative correcting Python script (own illustration) .....	109
Figure 59: Lidar DEM height offset corrected(1,3m) minus SfM Sony Nadir factor corrected DSM (own illustration) .....	111
Figure 60: Lidar DEM height offset corrected(1,3m) minus SfM Pentacam all factor corrected DSM (own illustration) .....	112
Figure 61: Error histograms and scatterplots for uncorrected SfM data (SN =Sony Nadir, PA= Pentacam All, PN= Pentacam Nadir, PO =Pentacam Oblique) .....	114
Figure 62: Error histograms and scatterplots for refraction correction via clear water index (SN =Sony Nadir, PA= Pentacam All, PN= Pentacam Nadir, PO =Pentacam Oblique), (own illustration) .....	115
Figure 63: Error histograms and scatterplots for refraction correction via calculated factor (CF),(SN =Sony Nadir, PA= Pentacam All, PN= Pentacam Nadir, PO =Pentacam Oblique), (own illustration) .....	116

Figure 64: Error histograms and scatterplots for refraction correction via linear regression function (SN =Sony Nadir, PA= Pentacam All, PN= Pentacam Nadir, PO =Pentacam Oblique), (own illustration) .....	117
Figure 65:Error histograms and scatterplots for refraction correction via python script using the clearwater index (SN =Sony Nadir, PA= Pentacam All, PN= Pentacam Nadir, PO =Pentacam Oblique, CWI= clearwater index), (own illustration) .....	118
Figure 66: Error histograms and scatterplots for refraction correction via Python script for the PO (PO =Pentacam Oblique) data set with three different option (own illustration).....	119

## List of Tables

Table 1: Refraction index for clear freshwater at sea level (1bar) own table with data from (Harvey et al. 1998, 770–773, Table 4-7) .....	11
Table 2: Comparison of bathymetric methods, Own modification (Woodget et al. 2015b, p. 48; Xu 2010; Kasvi et al. 2019; Dietrich 2017a; Marks and Smith 2008; Kongsberg 2020).....	17
Table 3:Theoretical calculations of the occurring light-beam angles at the air-water transition, the resulting apparent depth and the value for the correction factor to correct the refraction at the given point of the image in nadir view.....	27
Table 4:Theoretical calculations of the occurring light-beam angles at the air-water transition, the resulting apparent depth and the value for the correction factor to correct the refraction at the given point of the image in oblique view. ....	28
Table 5: Calculated refraction factor, (SN =Sony Nadir, PA= Pentacam All, PN= Pentacam Nadir, PO =Pentacam Oblique).....	42
Table 6: Overview used image data for SfM processing .....	49
Table 7: DGNSS point measurements and numbers by category .....	49
Table 8: Error statistic for raw SfM data on land and under water, (SN =Sony Nadir, PA= Pentacam All, PN= Pentacam Nadir, PO =Pentacam Oblique).....	50
Table 9: Error statistic water surface height .....	50

Table 10: Agisoft error statistic, Root Mean Square Error (RMSE) .....	52
Table 11: Highest possible orthomosaic resolution for the four different data sets, (SN =Sony Nadir, PA= Pentacam All, PN= Pentacam Nadir, PO =Pentacam Oblique) ..	54
Table 12: Point cloud density and number for the four different data sets, (SN =Sony Nadir, PA= Pentacam All, PN= Pentacam Nadir, PO =Pentacam Oblique) .....	56
Table 13: DSM resolution for the four different data sets, (SN =Sony Nadir, PA= Pentacam All, PN= Pentacam Nadir, PO =Pentacam Oblique).....	56
Table 14: Depth error statistic comparison for different refraction approaches on four different data sets.....	58
Table 15: Height differences at the DGNSS measured points on land with possible explanations of height deviation .....	66

## List of Abbreviations

UAS	Unmanned Aerial System
UAV	Unmanned Aerial Vehicle
RTK	Real Time Kinematic
Lidar	Light detection and ranging
SfM	Structure from Motion
DSM	Digital Surface Model
GPS	Global Positioning System
GNSS	Global Navigations Satellite System
DGNSS	Differential Global Navigations Satellite System
SN	Sony Nadir
PA	Pentacam all images
PN	Pentacam nadir images
PO	Pentacam oblique images
RMSE	Root Mean Square Error
CWI	clearwater index
CF	Calculated factor

LRF

Linear Regression function

PS CWI

Python script with clearwater index

PY 1,4

Python script with refraction factor 1,4

## 1. Introduction

During the last decade, a technological revolution in geomatics has transformed digital elevation modeling, geomorphological terrain analysis as well as hydrographic surveying. The acquisition of topographic and bathymetric data has been transformed mostly by a new generation of remote sensing technologies. For terrestrial surveying, airborne and terrestrial laser scanning and digital photogrammetry have revolutionized the quality of digital surface models (DSMs) on extending their spatial extent, resolution, and accuracy. Also, the acquisition of remotely sensed data from a range of cheap, lightweight platforms, such as Unmanned Aerial Vehicles (UAV) is becoming more commonplace and reduces surveying costs. In the bathymetric field, besides the laser scanning, advances in hydrographic surveying through single and multibeam echo sounder make it possible to construct continuous high-fidelity terrain models of freshwater and marine environments in a high resolution (Westoby et al. 2012, p. 300).

In this master thesis, the usage of Unmanned Aerial Systems (UAS) for shallow water lake bathymetry should be tested. Therefore, a new camera system should be used and compared with the currently used single sensor capturing setup. The new camera systems consist of five cameras. One captures a nadir image, and the other four take oblique images. The five shots were taken simultaneously, which gives the afterward possibility to combine different pictures from different angles from one UAV flight for the SFM process.

Further, various methods for refraction correction will be applied to the generated data sets. In the beginning, methods that can be applied to the derived DSM are tested. In this category, the refraction correction with the clearwater index, the refraction correction with a calculated factor, and the refraction correction with a linear equation can be named. While for the application of the clearwater index, no further measurement data is required, the other two approaches are based on calculations based on underwater reference points. A completely different way will be the application of the algorithm developed by Dietrich (Dietrich 2017a). He implemented an iterative calculation of the original water-depth within a Python script. This correction is applied directly to the 3D point cloud.

## **1.1. Motivation**

The EU Water Framework Directive is an agenda for maintaining and improving the quality of aquatic ecosystems in Europe. It places ecology at the center of the responsible authorities and ministries. Especially in aquatic ecology, the exact knowledge of the sole morphology is fundamental. The agenda states that the bathymetry condition should be monitored at regular intervals (EU 2000). A detailed resolution of the underlying terrain model is necessary to map these areas since inaccuracies in shallow water areas are particularly noticeable in the habitat description (Hauer et al. 2009). Using transverse profiles, the terrain model will be interpolated between these cross-sections. However, in very simple waterbeds, the error caused by such interpolation is lower, but in more complex systems, there can be plenty of limitations (Conner and Tonina 2014). As a result, many EU member states have difficulty meeting their obligation to monitor and implement remediation programs in areas where water does not meet the criteria (Pinz 2011). Therefore, there is an increased need for water body structures measurements, particularly the form of rivers and seas and their beds. Waters are dynamic systems and subject to constant changes. Flood events or structural modifications to streams always change to the bottom course. So, the bottom course must be regained regularly, promptly, and cost-effectively. UAS might provide a new, reliable as well as cost-efficient solution for bathymetric mapping in shallow water areas.

## **1.2. Problem Statement / Research Question**

Bathymetry is used to measure water depths, for example, in lakes or the ocean. In shallow waters, it is difficult to map the depths in a high resolution. In the past, methods like single beam echo sounder or green laser scanner were used for bathymetry. But these methods are time-consuming and expensive (Bangen et al. 2014).

A low-cost method for computing DSM data in the terrestrial field is the use of data acquisition through UAS and digital photogrammetry. Unfortunately, this approach cannot be easily applied for bathymetry because of light refraction arising when light crosses from one media to another.

To better understand the effect of light refraction on UAV captured images, specific calculations for single images will be conducted. This calculation will answer the first research question: Which influence does the refraction of light have on our particular camera sensor setup?

The main goal of this master theses will be to investigate different approaches for refraction correction methods for UAS multi-view photogrammetry. The first research question on this topic will be which of the refraction correction methods works best for our captured data sets. What limitations do these methods have? Further, the result's evaluation should demonstrate each technique's advantages and disadvantages during the data processing workflow. In addition, the outcoming bathymetric results will be discussed.

Further, this master theses will compare two different images capturing systems. Consequently, an additional research question will be whether the nadir camera system or the multi-directional camera system works best for UAS multi-view photogrammetry and which advantages or possibilities a multi-directional camera system has compared to a one-directional camera system in this use case scenario?

To sum up, the key research questions concerning the proposed project are:

- 1) Is it important to consider the influence of the refraction of light on UAS based bathymetric surveys?
- 2) Which refraction correction methods for UAS multi-view photogrammetry is most suitable?
  - a. Iterative camera orientation and point cloud based developed by (Dietrich 2017a)
  - b. Bathymetric scaling for refraction correction on DSM's:
    - i. Freshwater index
    - ii. Empirically derived factor function based on additional reference data
    - iii. Empirically derived depth dependent linear function based on additional reference data
  - c. What is the difference of Single-nadir-view and Multi-view sensor systems, in the context of shallow water bathymetry?

### 1.3. Methodological considerations

This research project consists of five phases, namely literature review, system design, field experiment, implementation and validation. Figure 1 gives an overview of the proposed research structure.

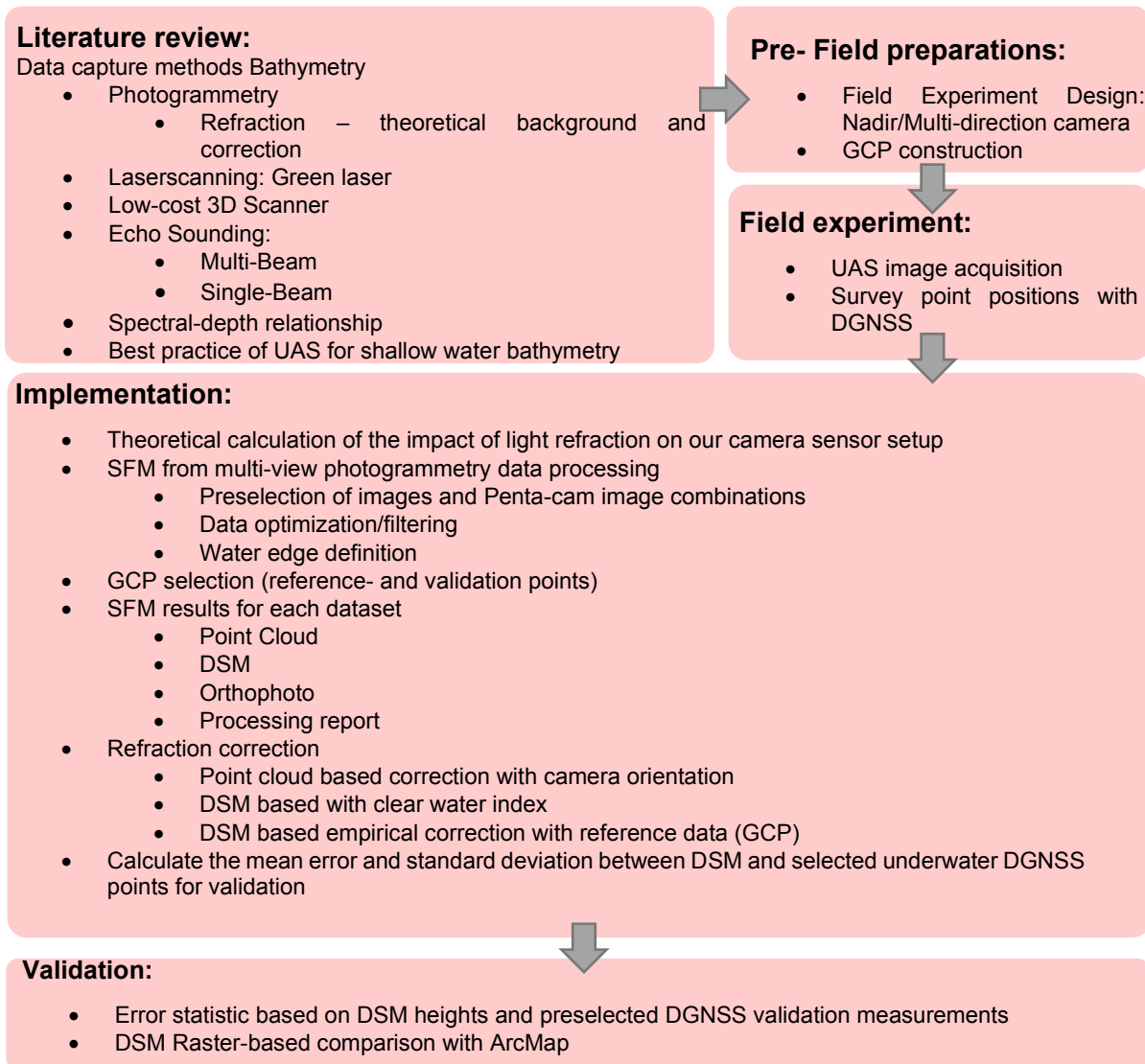


Figure 1: Overview of Project Workflow

This work's first prerequisite was a comprehensive literature review focusing on all available methods for shallow water bathymetry, their accuracy, and the theoretical background of light refraction. Further, the processes of generating bathymetry from

different data sources and merging bathymetric data with terrestrial data were investigated.

For this master thesis, data from lake Weissensee was processed. The lake Weissensee is located in Carinthia and the photogrammetric data as well as the ground control point data were captured within that master thesis. Terrestrial Lidar data of the test site was provided by "Amt der Kärntner Landesregierung".

A workflow for capturing the data with an Unmanned Aerial system and a multi-view camera system was designed containing all the steps necessary to perform photogrammetry water depth measurements. During the flight, a nadir image, as well as a multi-directional image was captured for later data comparison of the two sensors.

Ground Control Point (GCP) targets were placed on land as well as underwater. Those points as well as further single-point measurements were then surveyed with a Differential Global Positioning System (DGNS) and used as reference and validation points.

For the correction of refraction, the iterative algorithm of Dietrich (2017) and different methods for scaling were used. Two of the scaling methods depend on reference data. However, some preprocessing steps were needed to apply these methods. After that, a validation of the two camera systems and the four refraction correction methods was conducted. The obtained result was then validated with the reference measurements and a conducted error statistic. Additionally, a comparison between the uncorrected DSM's of the two different camera systems, between the uncorrected and the corrected of each camera system and between the corrected DSM's of the two camera systems was done. To reduce the number of comparisons, the best result of each refraction correction approach was selected and compared.

#### **1.4. Expected Results**

As a result, a literature review, including all methods for shallow water bathymetry is expected. The theoretical background of the photogrammetric process and the refraction of light during two media photogrammetry will also be a part of this thesis.

After testing various approaches for refraction correction with two different sensors, the best method for each sensor will be demonstrated. Additionally, the advantages or weaknesses of each correction method under certain circumstances and scenarios (water depth, ground condition, etc.) should be highlighted.

Further, it will be shown if the Pentacam (a multi-directional camera system, 4 sensors off-nadir, 1 sensor in nadir direction) can perform better than the Sony Alpha 7RIII (1 sensor in nadir direction) for capturing bathymetry. Moreover, a workflow for the Pentacam with criteria for image and sensor selection will be presented since there are several options to combine the images captured from five different oriented sensors.

## **1.5. Structure of this thesis**

The first chapter includes the motivation, problem statement and research question, the methodological considerations, the expected results, and the thesis structure. The theoretical background is described in chapter two and consists of the different technologies and methods used to capture bathymetry. In chapter three, the approach is further described. This chapter includes the conceptual workflow structure as well as the planning steps for the UAV field mission. It also describes several preprocessing steps, the correction approaches, the quantitative evaluation methods and the used software and hardware. The following chapter four includes a description of the project area and information about additional used data. After the implementation in chapter five, we will present the results in the following section six. In chapter seven, the results are discussed. Chapter eight then contains the conclusion and further work followed by the references.

## **2. Theoretical Background**

In this section, the needed know-how for this research is provided. Information from related literature and best practice studies should explain how photogrammetry works (see chapter 2.1) and how it can be used for bathymetry (see chapter 2.2), which other method exists for capturing bathymetry (see chapter 2.3-2.5), what are the best practice scenarios for each method (see chapter 2.6) and finally how a multisource DSM can be generated (see chapter 2.7).

### **2.1. Theoretical background SfM Photogrammetry**

Photogrammetry is the science and technology of making measurements from photographs and other image sources (Longley et al. 2016, p. 185). For single images, only 2D measurements are possible if there is no further geometric information available. For example, orthophotos can be generated with the extra information of the digital elevation model (Luhmann 2003, p. 103).

Stereo photogrammetry relies on two overlapping images (Figure 2, Left) with a defined intra-axial distance ( $b$ ). The spatial intersection of image rays allows to generate 2.5-D and 3-D information (Luhmann 2003, p. 103).

Multi-view stereophotogrammetry, specifically Structure-from-Motion (SfM) differs from the stereophotogrammetry by solving the geometry of the scene automatically, camera positions and orientation by simultaneously using a highly redundant, iterative bundle adjustments procedure, based on a database of features automatically extracted from a set of multiple overlapping images (Figure 2, Right) (Dietrich 2017a, p. 355)); ((Westoby et al. 2012, p. 301).

In the case of aerial capturing, it is usual to have a 60% overlap along each flight line and a 30% overlap between flight lines (Longley et al. 2016, p. 185).

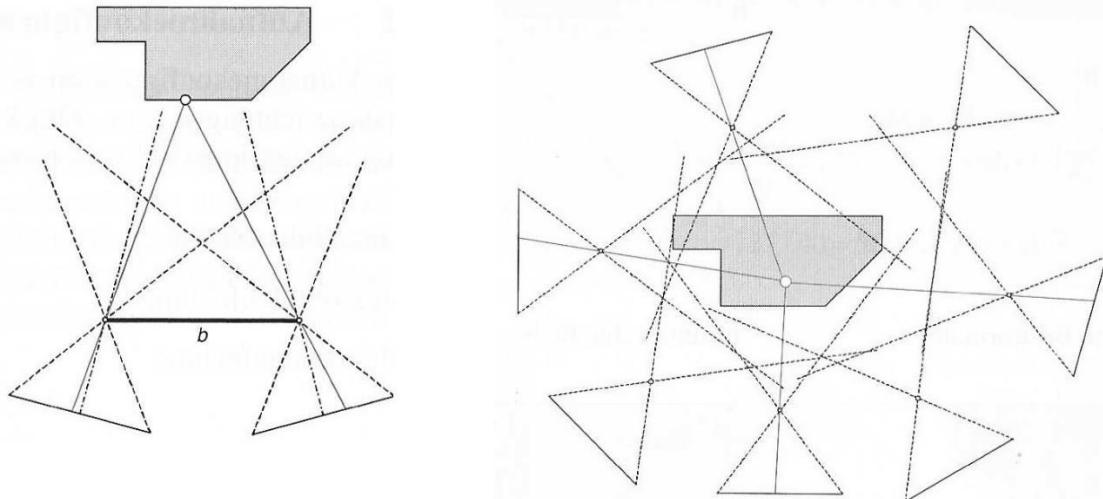


Figure 2: Left: Stereo Photogrammetry with a single stereo pair of photographs ( $b$ : intra-axial distance), Right: Multi-view stereophotogrammetry (SfM) with multiple, overlapping photographs (Luhmann 2003, pp. 104–105)

## 2.2. Two Media Photogrammetry

When using two media photogrammetry, the refraction of the light has to be considered. In the following, the theoretical background behind two media photogrammetry in general and photogrammetry for bathymetry is explained. Afterward, different methods to deal with refraction correction for capturing bathymetry are described in this chapter.

### 2.2.1. Theoretical background Two Media SfM Photogrammetry for bathymetry

With stereophotogrammetry and multi-view stereophotogrammetry, it is possible to capture bathymetry for shallow water. The two methods only work in clear water areas (TEWINKEL 1963); (Woodget et al. 2015a). The major problem of the two media photogrammetry is the refraction of the light caused during the transition from one media to another. In the case of bathymetry, it is the transition from air to water media. When this effect occurs, the light gets bent, which causes in-water measurements to appear shallower, referred to as the apparent depth. In Figure 3, the refraction

trigonometry of a single measurement point/camera combination can be seen (Dietrich 2017a, p. 355).

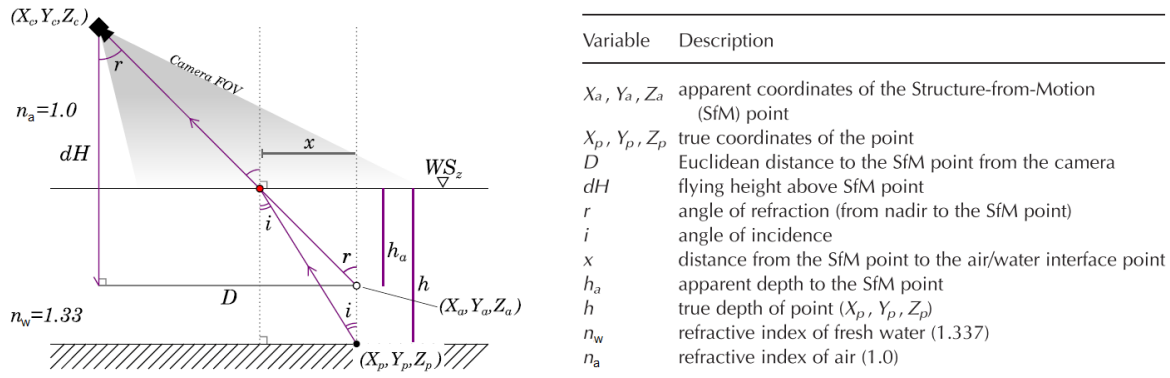


Figure 3: Trigonometry of the refraction angles for a single point/camera combination. Own modification (Dietrich 2017a, p. 2, Figure 1, Table 1)

With Snell's law, it is possible to calculate the underwater point's actual depth (Equation (5)).  $n_w$  is the refractive index of freshwater and  $n_a$  is the refractive index of air to correct the refraction and get the right water depth.

$$n_w \sin i = n_a \sin r \quad (1)$$

While the value for air can be assumed with the value 1.0 (Dietrich 2017a), the index for water varies with different factors (Schiebener et al. 1990) & (Harvey et al. 1998). The refractive index of water can be formulated as a function of temperature, density, and wavelength. The refractive index of water ( $n_w$ ) depends on the optical wavelength as well as water temperature, salinity and depth (Grenzdörffer and Naumann 2016, p. 848).

In conventional stereophotogrammetry, the direct application of Snell's Law is complicated by the fact that the point is seen from two overlapping images. Therefore, the positions of the cameras are different, and this results in different angles for  $r$  and  $i$  for each taken photograph. The different angles necessitate that the equations be solved for each camera, resulting in slightly different outcomes for the actual depth (Dietrich 2017a, p. 356).

### 2.2.2. Refraction correction with clear water refraction index

This method uses a simplified version of Snell's Law (Equation (2)) to apply the refraction correction to the calculated raw water depth ( $h_a$ ) with the refraction index for clear freshwater ( $n_w$ ) (Woodget et al. 2015a).

$$h = n_w * h_a \quad (2)$$

This simplification is based on the assumption that the angles ( $r$  and  $i$ ) are less than  $10^\circ$ ; thus, Snell's Law can be substituted using the "small angle substitution" ( $\sin(\theta) \cong \tan(\theta)$ ). This allows calculating the water depth by multiplying the refractive index of water with the apparent depth. (Woodget et al. 2019)

Light gets refracted at different angles, depending on the wavelength of the light. This effect is illustrated in Figure 4. Because of this effect, photographs get more and more blurry the deeper the waterbody is.

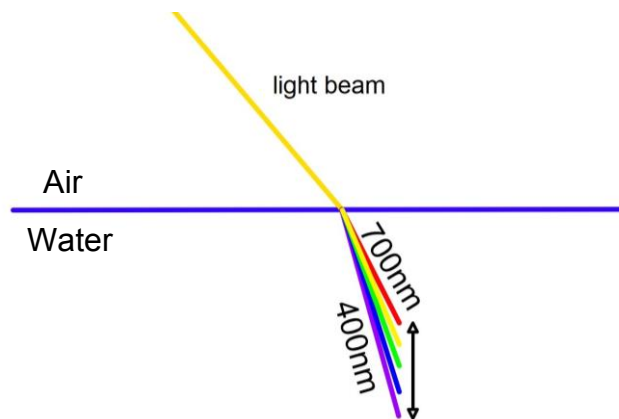


Figure 4: Different refraction effect of visible light during the transition from air to water (own illustration)

Since photogrammetry uses cameras that detect the visible spectrum with an estimated wavelength between 400nm and 700nm, possible values for  $n_w$  (freshwater) are between 1.331 and 1.338 (Harvey et al. 1998). Table 1 gives an overview of the possible refraction indexes for clear freshwater at an air pressure of 1bar.

Table 1: Refraction index for clear freshwater at sea level (1bar) own table with data from (Harvey et al. 1998, 770–773, Table 4-7)

Temperature/Wavelength	488nm	514.5nm	589nm	632.8nm
0°C	1.338	1.337	1.334	1.333
10°C	1.338	1.336	1.334	1.332
20°C	1.337	1.336	1.333	1.332
30°C	1.336	1.335	1.332	1.331

For the photogrammetric refraction correction of freshwater values between 1.33 (Agrafiotis and Georgopoulos 2015, p. 5) and 1.34 (Woodget et al. 2015b, p. 55) has been commonly used.

This technique performs best for a water depth less than 0.2 m and images captured close to nadir. In combination with oblique pictures and a greater water depth a more advanced refraction correction procedure is recommended (Woodget et al. 2015b, p. 62).

If this method should be applied on saltwater  $n_w$  can be calculated empirically with equation (3). Where  $n_w$  = refractive index of water,  $d$  = water depth (m),  $\lambda$  = wavelength (nm),  $T$  = water temperature (°C) and  $S$  = water salinity (%) (from (Höhle, J. 1971) cited after (Grenzdörffer and Naumann 2016, p. 848)

$$n_w = 1.338 + 4 * 10^{-5} * (486 - \lambda + 0.003d + 50S - T) \quad (3)$$

### 2.2.3. Empirical refraction correction with reference points

For the empirical correction with control points, reference points are needed. Those could be either measured with GPS with an RTK service or with a total station (Grenzdörffer and Naumann 2016). Further, the data collected with the measurement methods explained in Chapter 2.3 and 2.5 can also be used if their accuracy is high enough.

The collected UAS photogrammetric data is then compared against the reference data. For this step, the assumed as well as the real water depth has to be calculated using the water-surface height. Using the simplified version of Snell's law (Equation (2)) the new refraction correction factor can be calculated.

Another method is to derive the empirical refraction coefficient through a regression analysis of the point cloud against the reference data. It is necessary to compute the regressions for all different datasets (Grenzdörffer and Naumann 2016).

#### **2.2.4. Multi-View refraction correction (pyBathySfM)**

This refraction correction is based on a workflow that includes a Python script "**pyBathySfM**" developed by Dietrich in 2017. The script uses the camera orientation for refraction correction on a photogrammetric data set. The algorithm calculates the real z values iterative. For each point in the submerged portion of the data set, the software calculates the refraction correction equations that follow for each camera that can capture that individual point and iterates through all the possible point-camera combinations (Dietrich 2017a, p. 357).

To have all the input data, it is necessary to export a georeferenced (or scaled) point cloud dataset, which requires the following column headers: "x", " y", " sfm\_z" and "w\_surf". Additionally, a file with the camera orientation is mandatory. This data can be calculated in Agisoft Metashape and consist of the camera positions (x,y,z) and orientations (pitch, roll, yaw). A third required input file delivers the information of the used sensor properties to the script. The headers need to be named "focal", meaning the camera's focal length in millimeters. The next two columns consist of the physical sensor dimensions in millimeters "sensor\_x" and "sensor\_y". All these input files must be in .csv-format (Dietrich 2017b).

#### **2.2.5. Refraction correction with machine learning**

This approach uses machine learning with an adopted vector regression method to address the refraction problem. Therefore, data from different test sites characterized by different types of seabed's and depths are used to train the computer. The experimental results from Agrafiotis et al. 2019 indicated the high potential for machine and deep learning architecture in bathymetric applications (Agrafiotis et al. 2019, p. 14).

### 2.3. Airborne laser scanning (Lidar)

Lidar (light detection and ranging, also known as airborne laser swath mapping, or ALSM) (Longley et al. 2016) uses differences in laser return times and wavelengths to produce an accurate topographic survey. Terrestrial Lidar is very accurate and therefore, commonly used for high-resolution topographic surveys (Alvarez et al. 2018).

For a single band Lidar system, it is essential to use the right wavelength depending on the surface nature (Figure 5). With a water-penetrating laser system (green laser), large areas of a water system can be surveyed. This technique is the core of Airborne Hydro Mapping. This method allows measuring the depth of shallow water and additional indicators such as water level (Jocham et al. 2014). Depending on the water depth, the optimal wavelength is between 420nm and 510nm for deep water like open oceans and between 520nm and 580nm for shallower water like coastal waters (Chen et al. 2019, p. 8). For reasons of cost, in deeper areas the method is supplemented with an echo sounder (Jocham et al. 2014).

At a global scale or for diverse surfaces, a Lidar system with multiple bands is the optimal configuration for obtaining the best detection (Chen et al. 2019, p. 8).

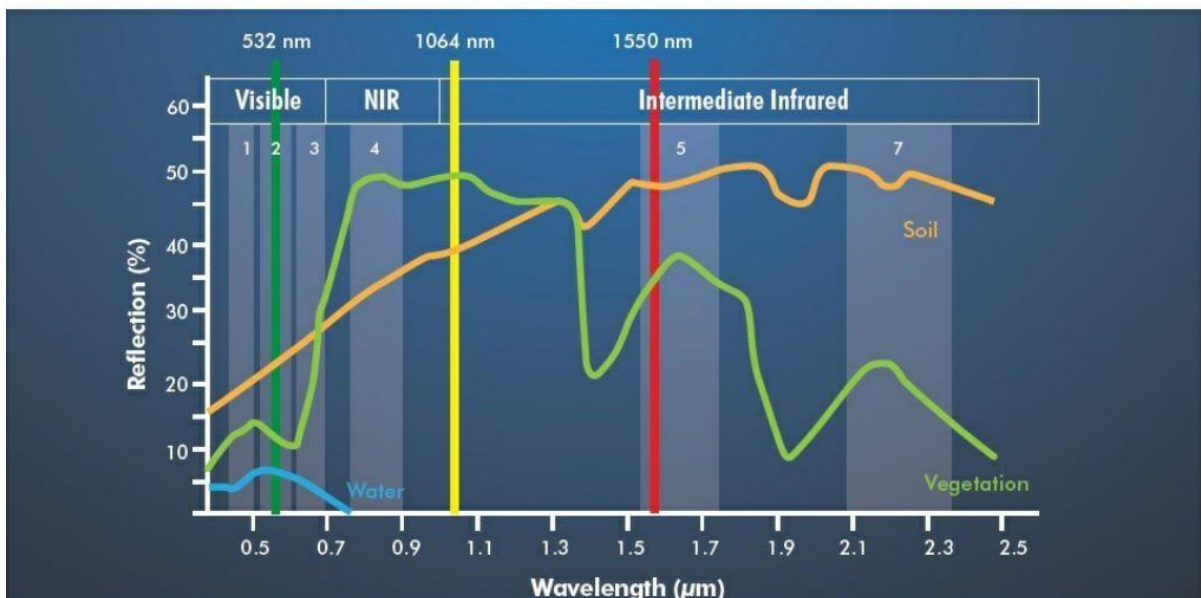


Figure 5: Examples of used wavelength for Lidar (Teledyne optech 2020)

With advancing technologies, Lidar systems become smaller in size. The actual model from Riegl, the VQ-840-G bathymetric laser scanner, is small and light enough to be mounted on smaller UAV's. It only weighs about 12kg and can scan up to a water depth, which is as deep as 2.5 times the Secchi depth (Riegl 2019). The Secchi depth is the depth at which a weighted, black-and-white disk with a diameter of 20 cm disappears from view (Dodds 2002, p. 40). This Lidar module achieves an accuracy of 20mm (Riegl 2019).

## 2.4. Low-cost 3D Scanner

The goal of this approach was to test the potential of a low-cost 3D sensor for shallow-water bathymetry. Therefore, the Microsoft camera "Kinect for Xbox 360" was used. This device uses a light beam at a wavelength of 830 nm that can penetrate water to project a speckle pattern on the captured scene. An infrared sensor captures the distortion of the pattern and calculates three coordinates (x,y,z) for each pixel. As a result, a maximum water depth of 30cm can be achieved for bathymetry with this sensor (Klopfer et al. 2017, p. 1392).

## 2.5. Echo sounding

The echo sounder uses acoustic instruments for measuring bathymetry (Church et al. 2012, p. 319). This device can be mounted on a ship and is capable of producing accurate depth measurements (Figure 6) (Xu 2010).

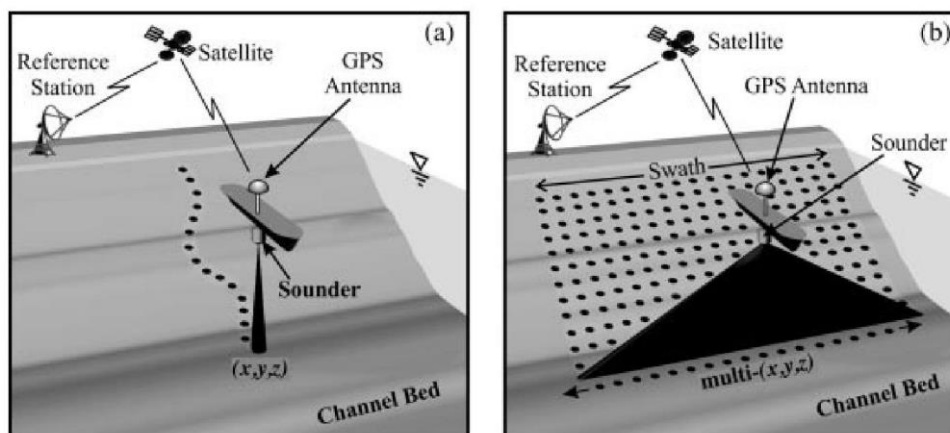


Figure 6: Using: (a) single beam and (b) multibeam (Church et al. 2012, p. 319, Figure 24.2)

In shallow water, single beam echo sounding can be used. Single-beam systems measure point per point beneath the research vessel. They are relatively easy to use and low-cost, but only provide depth information along the track line of the ship (Alvarez et al. 2018). It is a single-point profile measurement and performs up to a minimum water depth of 0,2m (Kasvi et al. 2019). This can provide profiles to identify the bedform (Alvarez et al. 2018).

Multibeam echosounder systems measure a whole swath of the underwater floor and retrieve a high-resolution bathymetry (Alvarez et al. 2018). This technology's downsides that it is limited by its minimal water depth of 2m and therefore not practicable for shallow water (Xu 2010). The rising inefficiency causes this depth limitation and therefore, costs are rising the shallower the water depth gets, turning this method inapplicable in shallow waters. Also, this technology requires significant investment in technologies. Therefore, multibeam echo sounders have been used mostly for ocean bathymetry and in some bigger fluvial and lake environments (Alvarez et al. 2018).

## **2.6. Spectral-depth relationship**

Spectrally based bathymetric mapping is based on retrieving information on water depth from passive remotely sensed data. The solar radiation propagated through the Earth's atmosphere interacts with the water surface, water column and substrate. The reflected amount of energy can be recorded with a detector via remote sensing. This is done by capturing several different wavelength bands. The total radiance captured in one band can be conceptualized as the sum of four reflected components: from the bottom, within the water column, from the water surface, into the view scattered light by the atmosphere. All these components influence the captured signal and therefore, ideally, would be taken into account. The bottom reflected radiance itself depends not only on the water depth but also on the ground's reflectance characteristics. To apply this method, certain circumstances must be given. The water depth must be shallow and the water itself must be clear. Also, the bottom substrates must be bright and highly reflective and favorable illumination must be given. Further reflections of the water surface and atmospheric effects should be as low as possible. To retrieve

bathymetric information, a calibration data set of ground control points is necessary (Legleiter 2013, p. 765).

## 2.7. Overview and Best practice

There are several different methods to capture bathymetric data. Depending on the needs, various methods can be chosen. After each technique has been described separately in detail, this chapter should give a better overview for selection. To capture the data, the sensors use various spectral sectors (Figure 7). Those sensors can be categorized into two groups: the first ones are passive sensors that are recording the emitted radiation. The second ones are active sensors transmitting electromagnetic radiation and measuring the radiation that is scattered back to a receiver after interacting with objects on the surface (Longley et al. 2016, p. 180).

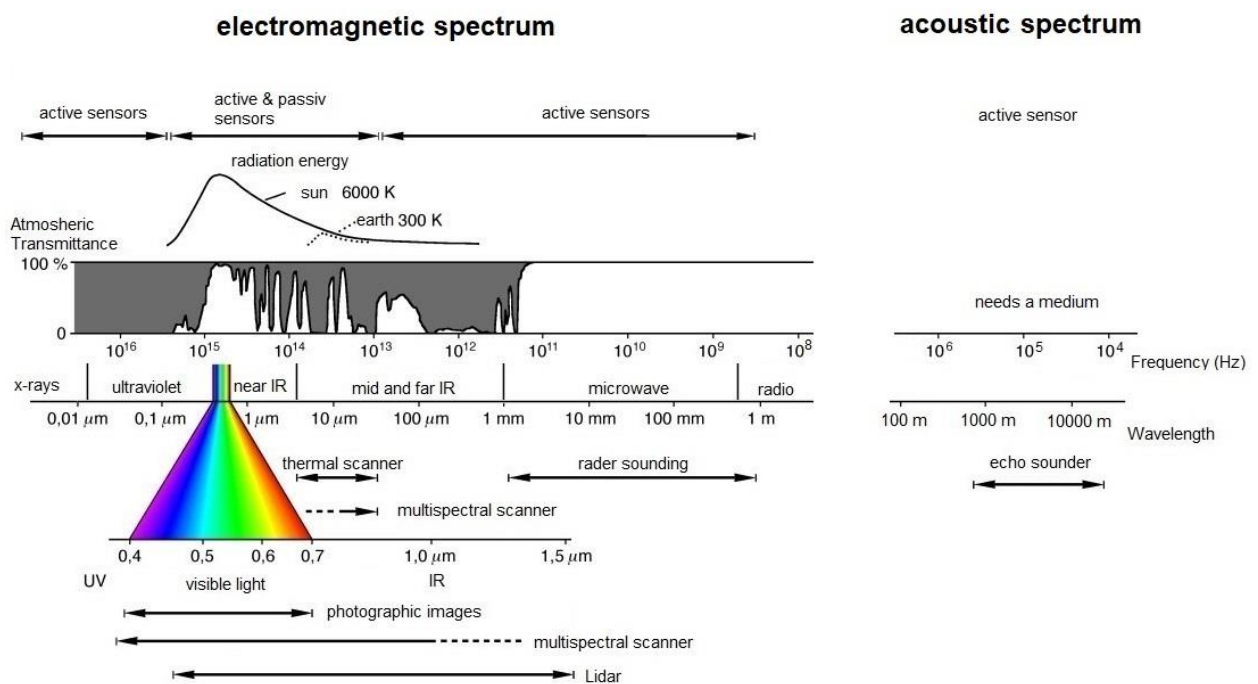


Figure 7: Left: The electromagnetic spectrum and atmospheric transmittance with typical spectral sectors for different sensors, right: The acoustic spectrum with typical acoustic sector for echo sounding. Own modification (Albertz and Wiggenghagen 2009, p. 69)

The capabilities vary with every technology. Table 2 gives an overview of several methods used for bathymetry. Besides the technical capabilities, also the expenditure (equipment, time and labor) is different for every technology.

Table 2: Comparison of bathymetric methods, Own modification (Woodget et al. 2015b, p. 48; Xu 2010; Kasvi et al. 2019; Dietrich 2017a; Marks and Smith 2008; Kongsberg 2020)

Approach	Typical mean height error	Typical spatial resolution	Typical max water depth	Typical min water depth (m)	source
Digital photogrammetry	5cm -17cm	5cm-100cm	(1 time the Secchi depth)	0	(Westaway 2001) (Westaway et al. 2003) (Lejot et al. 2007) (Feurer et al. 2008) (Lane et al. 2010) (Dietrich 2017a) (Kasvi et al. 2019) (Paulus et al. 2019)
Bathymetric Lidar	10cm-30cm	100cm	2.5 times the Secchi depth	0	(Kinzel et al. 2007) (Feurer et al. 2008) (Bailey et al. 2010)
low-cost 3D Scanner	0,7cm	0,1cm (at object distance 0,5m) - 7,5cm (at object distance 5m)	0.3m	0	(Klopfer et al. 2017)
Single beam echo sounder	Depending on depth (e.g. 2cm at depth range from 0.2m to 1.4m)	Variable/ 1 Point per measurement	>5500m	(500kHz) 0.2m	(Marks and Smith 2008) (Kasvi et al. 2019) (Kongsberg 2020)
Multibeam echo sounder	Depending on depth (e.g. 2cm at depth range from 0.2m to 1.4m)	Depending on depth	(500 kHz) 50m (12 kHz) 11000m	(500kHz) 0,2m (12 kHz) 20m	(Marks and Smith 2008) (Kongsberg 2020)
Spectral-depth relationship	10cm	5cm -400cm	1.0 m	0	(Winterbottom and Gilvear 1997) (Westaway et al. 2003) (Carbonneau et al. 2006) (Lejot et al. 2007) (Legleiter 2012)

### 3. Approach

In this chapter, the theoretical background is described for solving the research problems. Also, the conceptual workflow structure is defined, followed by the description of the UAV Mission planning.

#### 3.1. Conceptual workflow structure

Figure 8 shows the conceptual workflow. It describes the steps from the different data sets to the result evaluation and can be divided into four main parts: Data capturing, data preparation, refraction correction, and evaluation.

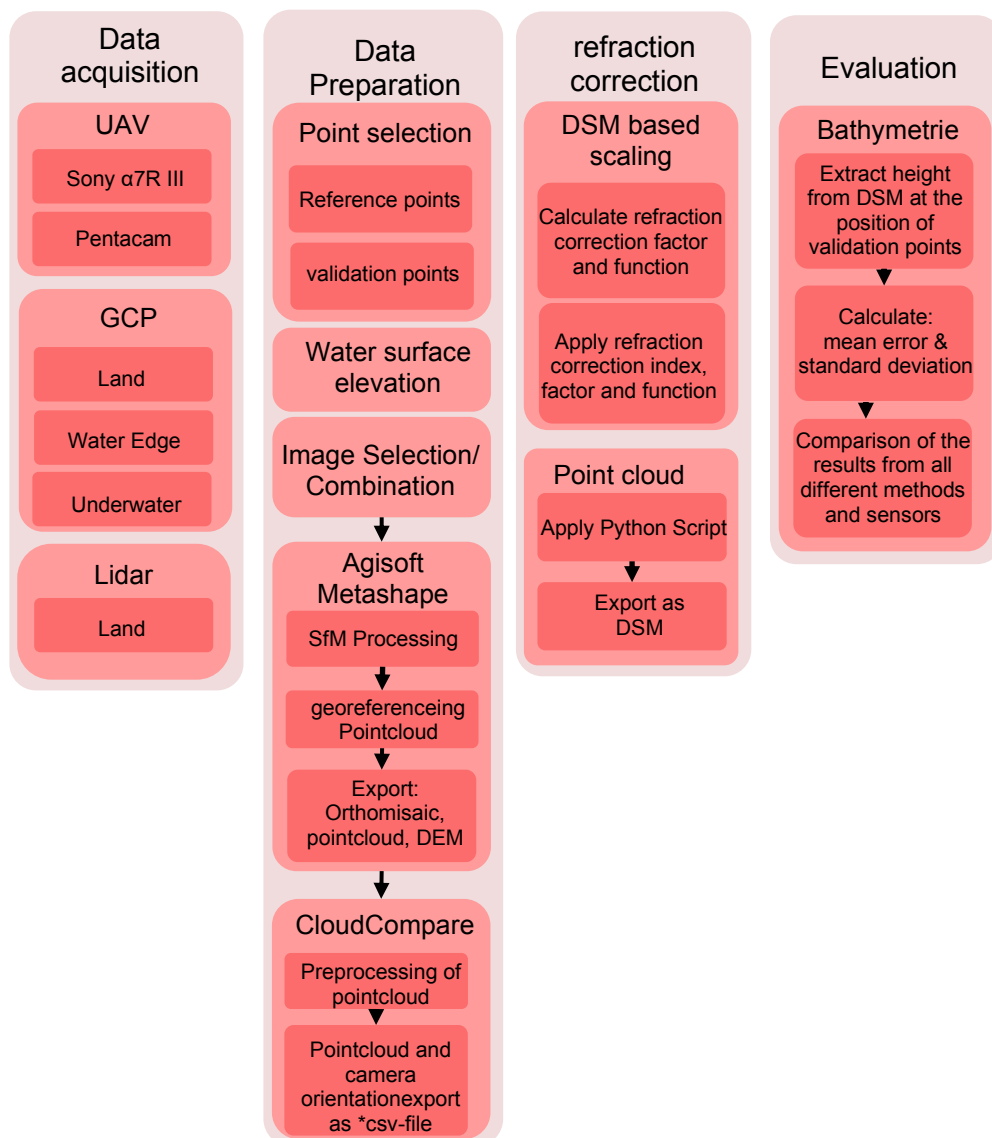


Figure 8: Conceptual workflow structure (own illustration)

## 3.2. Data capture

### 3.2.1. UAS

The aerial images were taken with a Leica Hexa Copter AX20 with a mounted Leica GS18 RTK (Figure 9). On this UAV, different Sensors can be mounted.



*Figure 9: Leica Hexa Copter AX20 with a mounted Leica GS18 RTK and Sony Alpha 7RIII, Left: ready for take-off. Right: during data acquisition with the camera in nadir position (own images)*

A Sony Alpha 7RIII with 42,4 MP was used to capture the nadir images. To take images continuously in nadir direction and to compensate any movement of the UAV, an additional 3-axis gimbal was mounted in between the UAV and the camera. It has a sensor size of 35,9mm x 24,0mm and can take pictures with a maximum resolution of 7952 x 5304 pixels. The size of one pixel on the sensor is 4,51 $\mu$ m x 4,51 $\mu$ m. This camera was equipped with a Sony lens with 55mm focal length and a maximum aperture of 1,8. The UAV was capturing the images in a flight height of 80m above the water level. This results in a Ground Sample Distance of 0,66 cm/px. The photos were taken with an overlap of 70% in flight direction and 70% vertical to the flight direction (Figure 11). During the flight 245 images were collected.

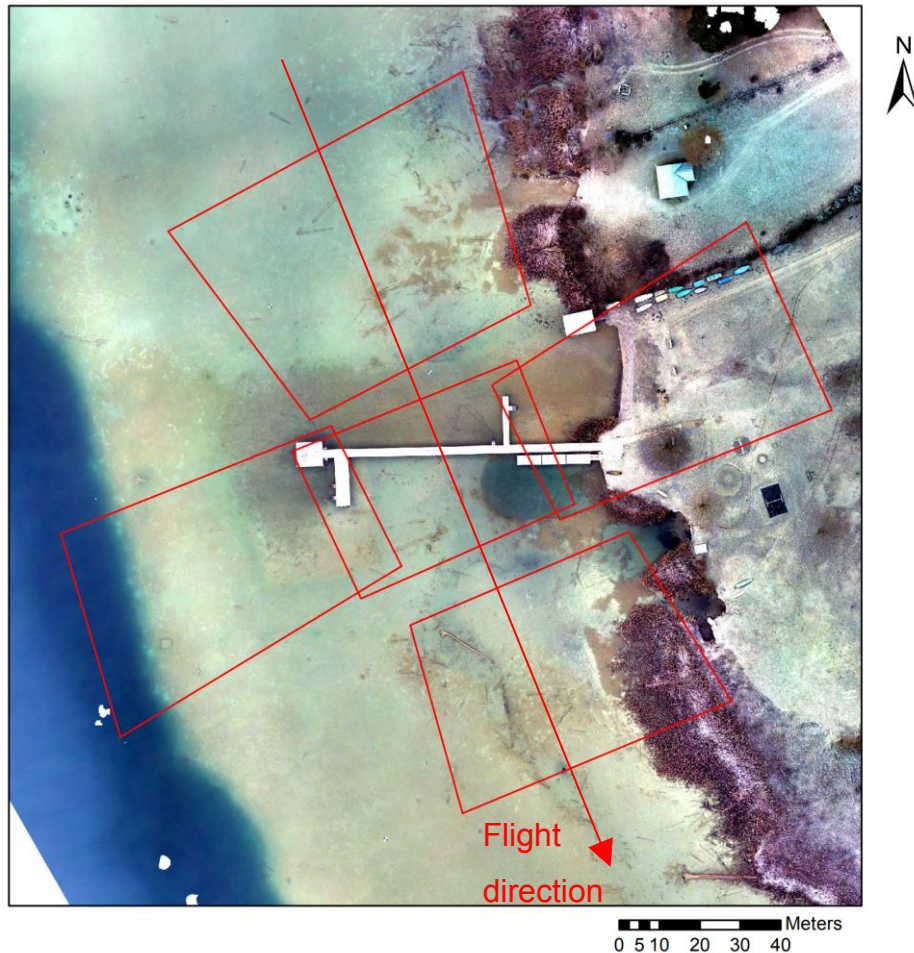


Figure 10: Calculated footprint of the estimated camera directions by Agisoft Metashape Professional captured with the five sensors on the Pentacam during one trigger event at a flight height of 89,79m above watersurface (own illustration)

The multi-directional Pentacam is based on five Sony ILCE-QX1 sensors with 20,1 MP combined with five lenses with 35mm focal length. Because of its bigger size it is mounted without any additional stabilization hardware directly on the UAV. Figure 10 shows the calculated footprint of one trigger event. This footprint was created with the Agisoft Metashape Professional Python script "footprints\_to\_shapes" (PolarNick239 2020). The two sensors in flight direction are mounted horizontally, while the two sensors looking to the sides are mounted in vertical positions. Because the UAV is not stopping for every shot and the Pentacam is not mounted on a gimbal, a slight tilt in flight direction occurs since the UAV must lean to the side it is moving to go into that direction. The sensor is 23,2mm x 15,4mm in size and the maximum resolution is 5456

x 3632 Pixel. The size of one pixel on the sensor is  $4,25\mu\text{m} \times 4,25\mu\text{m}$ . The setup of this camera system is on camera capturing nadir images while the other four are placed 25 degree off nadir. During the image capturing, the UAV reached a flight height of 80m above water level. This setup results in a ground sample distance of 0,97 cm/px. The overlap in flight direction was 80% and the overlap of the different flightpaths was 70% (Figure 11). Combined 1820 images could be collected with the five sensors.

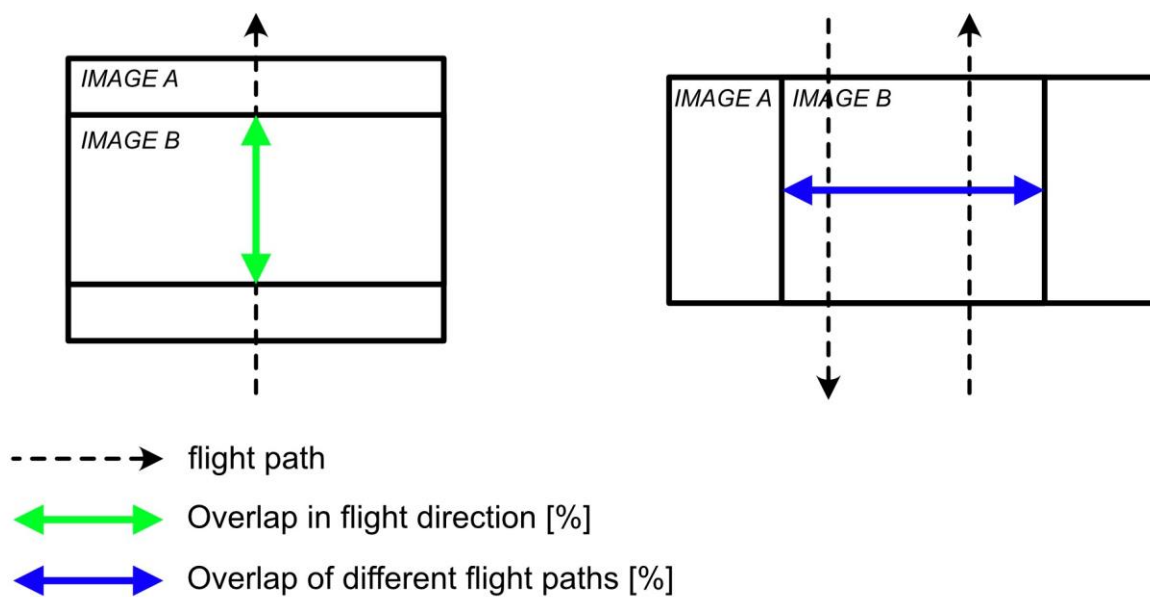


Figure 11: Illustration of the different overlap possibilities (own illustration)

To plan a UAV Mission, several steps are necessary. Depending on the UAV and the flight sight, different prerequisites are required for the UAV as well as for the pilot. The used Leica Hexa Copter AX20 is registered in the class C UAV, which means it is allowed to fly over settlements. Furthermore, the pilot needs a license from the Austro control to legally operate the UAV(Austro Control 2020).

Another critical factor that should be taken into consideration while photogrammetry mission planning is optimal site conditions. Since photogrammetry depends on the visible structure of the bottom of the water body, clear water is very important. High levels of suspended sediment (cloudy water) or tannic conditions (dark brown water) will reduce the measurable depth. Further, a flat-water surface with as less waves as

possible is crucial. Both wind-driven waves and hydraulic waves (rives and standing waves) will increase the "noise" in generated point cloud (Dietrich 2017b). To reduce reflections on the surface, overcast weather conditions are optimal (Grenzdörffer and Naumann 2016, p. 846).

The first field experiments were executed on the 5. December 2019. The weather conditions were below 0 °C and the surface of the lake was not frozen. There was no wind and the lake had a calm plane surface. The water was clear and therefore, a good view to the bottom of the examined area was given.

Ground control plates were placed on land as well as underwater. They were dropped from a canoe. The underwater plates were constructed with a small buoy. The positions of this plates were then used as reference and validation points.

After transferring the photos to a computer, a visual verification is necessary to remove unnecessary images right away. This can be for example images taken before takeoff and landing.

### **3.2.2. DGNS point measurements**

The reference and validation points were measured with a GNSS system from Leica with RTK service. Beforehand the exact site circumstances were observed to plan the capturing method for the GCP's. Here the water depth and lake bottom conditions are crucial. It must be considered when selecting the right equipment for in-water measurements.

All reference and validation points were collected with the GNSS antenna mounted on a 2,2m long pole. Therefore, only shallow water regions with a lower water depth of 2,2 m could be measured. On land and in the shallower water area near the boardwalk this was done per foot, in the deeper areas the points were collected by driving a canoe to the chosen spot. The with and black GCP plates had a size of 1mx1m and were placed on land as well as underwater. For easier aiming underwater, a funnel was mounted to hit the exact center of the plate with the pole of the DGNS device. The measurements were taken from all placed ground control plates on land and under water. For the underwater validation supplementary validation points were collected

from the natural lake bottom. Additionally, water edge points were collected to establish the water surface elevation (Dietrich 2017b)

This reference data is not only crucial for empirical evaluation of the different capturing and correction methods but also for the empirical determination of the refraction correction factor (Grenzdörffer and Naumann 2016, p. 848).

After importing and visualizing the collected data on a map they had to be categorized into the different using purposes (validation or reference points) and their location (underwater or on land points).

### **3.3. Photogrammetric processing**

#### **3.3.1. Image selection and SfM processing**

The unselected images from the UAV field experiment must be prepared before they can be processed. Therefore, it is necessary to remove all pictures which were not meant to be used in the next processing steps. For example, all images taken during the UAV starting and landing phase can be deleted. Also, different image combinations are possible and will be tested during the next step for the dataset captured with the Pentacam.

For the photogrammetric processing of digital images and 3D spatial data generation, Agisoft Metashape Professional is used. The generated point cloud will then be georeferenced with the on-land measured reference GCP's. Afterward, the program allows exporting a point cloud as well as the DEM. For the later applied correction process, it is also necessary to export the calculated/estimated camera positions and orientations as csv-file. To inspect the quality of the created SfM data a report can be created within the program.

### **3.3.2. Sensor combinations and Outputs**

The SfM processing was conducted with 4 different datasets of images. The first dataset is created from Images captured with the Sony alpha 7RIII which pointed in nadir direction. This data set will be further on referred to the abbreviation SN. The three other datasets consist of different image view angle combination from the Sony ILCE-QX1 sensors of the Pentacam. One was created with all views (PA), for one only the nadir images was used (PN) and the last one was processed from only oblique views (PO). For each of those 4 data sets a point cloud, an Orthomosaic and a DSM were created.

### **3.4. Refraction correction**

Before the refraction correction can be conducted the , the water surface elevation knowledge is mandatory to calculate the apparent water depths and subsequently, the true water depths. (Woodget et al. 2019) Therefore, one of the key variables for accurate and reliable refraction correction is the water surface elevation.

#### **3.4.1. Considerations of the Influence of camera angles on refraction**

Since we are testing different camera angles and camera constellations, a theoretical calculation of the camera angle's impact was done by using Snell's law. Therefore, a flight high of 80m was assumed. The value for the refraction index of freshwater was 1.337 and for air 1. Since the goal of this calculation was to show the different impacts of the angle of the light beam, the ground was estimated as a flat surface at one meter of water depth. Figure 12 shows the differences in water depth outcomes. The black line at 48° illustrates the limit and the point at which total internal reflection occurs (Dietrich 2017a, p. 356).

The second black line at 35° represents the border at which the Python script byBathySfM V4.0 (Dietrich 2019) can optionally cut off the calculation. This option exists because, at higher refraction angles, the corresponding larger point-camera

distance and longer through water distance of the light beam causes a decreased accuracy. (Woodget et al. 2019)

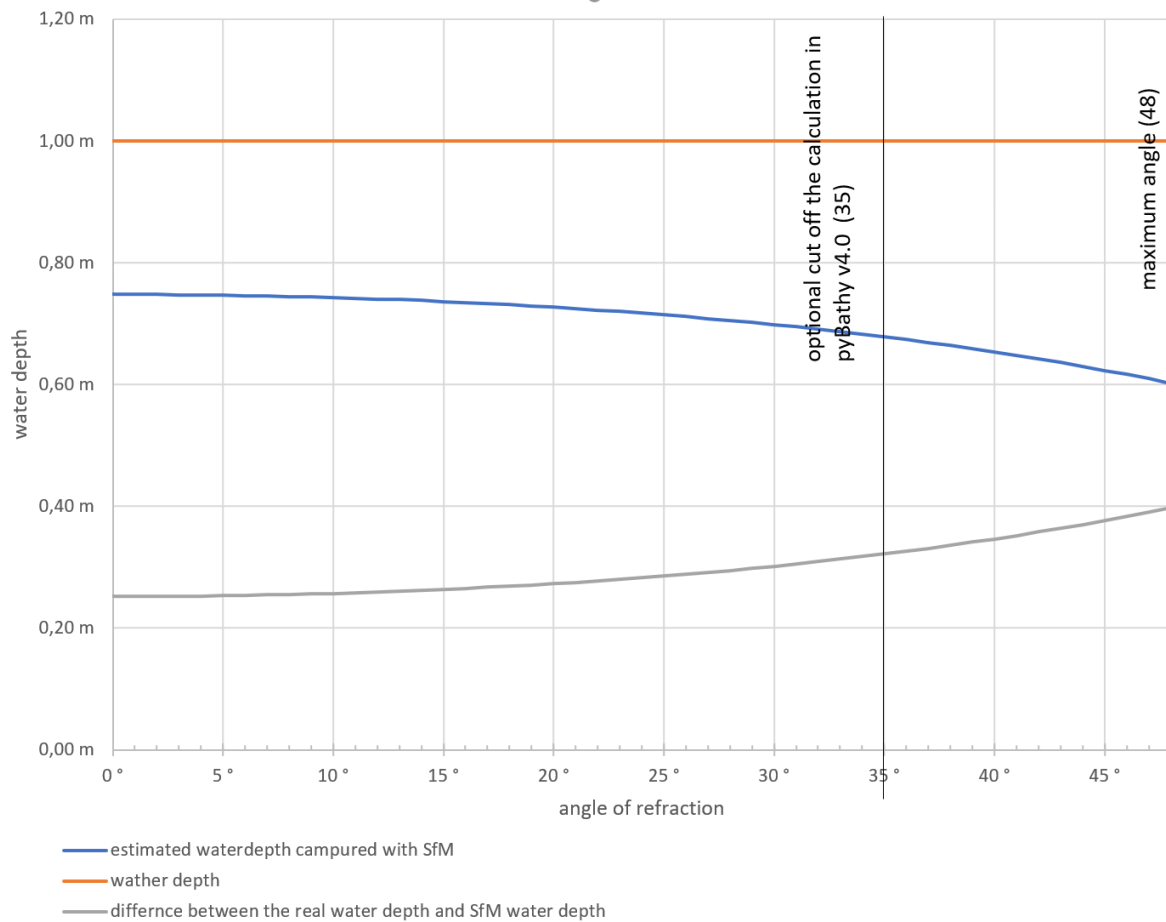


Figure 12: Refraction effect at 80m flight altitude and 1m water depth (own illustration)

Figure 12 also shows why the simplification of Snell's Law using the "small angle substitution" can be used up to an angle of 10°. Up to this point, the height differences are small and thus can be neglected by calculating the water depth with only the refraction index and apparent water depth.

Since a photo captures light beams with different angles, the refraction impact is also different within one image. Further research has been done to investigate the influence of the different light beam angles captured with our camera setup on the estimated water depth and refraction correction factor. At nine different points (four Corner points, four points located at the middle of the sidelines and one point in the middle of the photo) the refracted heights and refraction indices were calculated (Figure 13 &

Figure 14). The assumed conditions were again 80m flight height, 1m water depth, a freshwater index of 1,337 and an index for the air of 1.

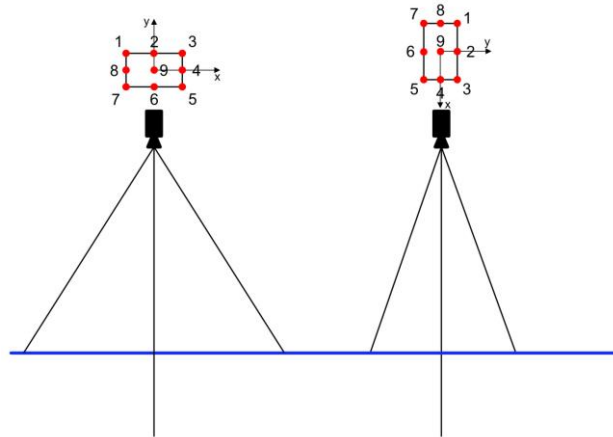


Figure 13: Sketch to represent the nine calculated points at nadir view (own illustration)

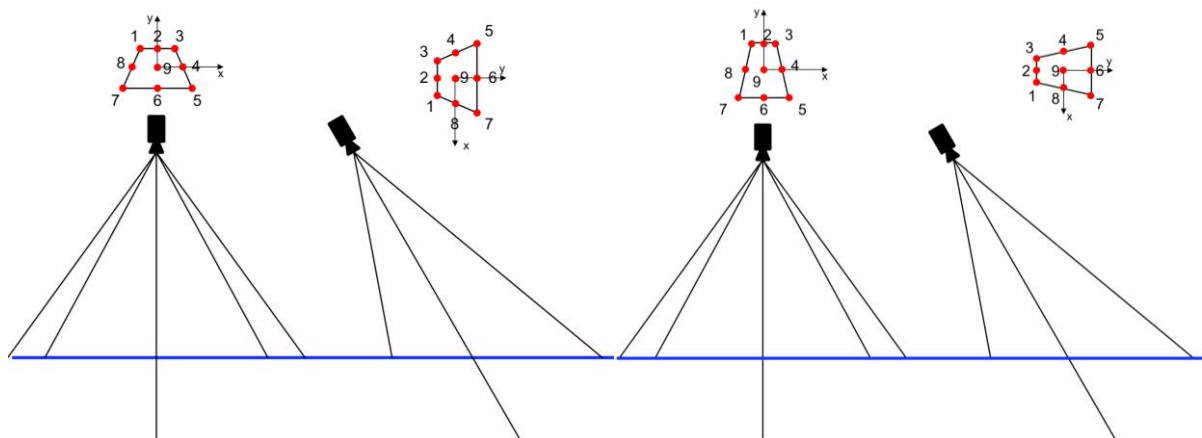


Figure 14: Sketch to represent the nine calculated points for 25° off-nadir view, left: horizontal sensor position, right: vertical sensor position (own illustration)

As Table 3 shows, the angles within one nadir image can vary between  $0^\circ$  and  $21,43^\circ$  for images that would have been captured with the Sony Alpha 7RIII and between  $0^\circ$  and  $21,69^\circ$  for the images that would have been taken with the in nadir direction looking sensor of the Pentacam. The apparent depth derived via photogrammetry at a real water-depth varies between 0,72m and 0,75m for both camera setups in nadir direction. Further, the calculated refraction factor based on the simplified Snell's Law was calculated. Therefore, the value for images taken in nadir direction is between 1,337 (clear water index) and 1,38.

Table 3: Theoretical calculations of the occurring light-beam angles at the air-water transition, the resulting apparent depth and the value for the correction factor to correct the refraction at the given point of the image in nadir view.

camera and orientation	Sony Nadir 0,00°			Pentacam Nadir 0,00°		
point number	r	ha	calculated correction factor at the given point	r	ha	calculated correction factor at the given point
1	21,43 °	0,72 m	1,381646	21,69 °	0,72 m	1,382822
2	12,31 °	0,74 m	1,350948	12,41 °	0,74 m	1,35118
3	21,43 °	0,72 m	1,381646	21,69 °	0,72 m	1,382822
4	18,07 °	0,73 m	1,368012	18,34 °	0,73 m	1,36897
5	21,43 °	0,72 m	1,381646	21,69 °	0,72 m	1,382822
6	12,31 °	0,74 m	1,350948	12,41 °	0,74 m	1,35118
7	21,43 °	0,72 m	1,381646	21,69 °	0,72 m	1,382822
8	18,07 °	0,73 m	1,368012	18,34 °	0,73 m	1,36897
9	0,00 °	0,75 m	1,337	0,00 °	0,75 m	1,337

min	max
-----	-----

The results (Table 4) for our camera setup with an oblique view angle off 25° off-nadir show that a part of the image already has a larger capturing angle than the before recommended 35° degree. The maximum angle occurs at points 5 and 7 with 40.91° at the horizontal image and 45,79° at the vertical image. For such big angles, the simplified Snell's Law using the refraction index of clear water cannot be used anymore. Therefore, a new factor for the occurring angles has been calculated using the simplified Snell's Law. The calculated height differences at 80m flight height and 1m water depth within an image taken in the oblique view are between 0,65m as the minimum and 0,74m as the maximum value. The correction value within a single image is between 1,35 and 1,54 for the horizontal view and between 1,35 and 1,62 for the vertical view.

Table 4: Theoretical calculations of the occurring light-beam angles at the air-water transition, the resulting apparent depth and the value for the correction factor to correct the refraction at the given point of the image in oblique view.

camera and orientation	Pentacam Oblique horizontal 25,00°			Pentacam Oblique vertical 25,00°		
point number	r	ha	calculated correction factor at the given point	r	ha	calculated correction factor at the given point
1	21,80 °	0,72 m	1,383295	13,99 °	0,74 m	1,355171817
2	12,59 °	0,74 m	1,351618	12,59 °	0,74 m	1,351618037
3	21,80 °	0,72 m	1,383295	13,99 °	0,74 m	1,355171817
4	30,65 °	0,70 m	1,436712	27,73 °	0,71 m	1,416060427
5	40,91 °	0,65 m	1,54239	45,79 °	0,62 m	1,618494878
6	37,41 °	0,67 m	1,499396	43,34 °	0,63 m	1,577576677
7	40,91 °	0,65 m	1,54239	45,79 °	0,62 m	1,618494878
8	30,65 °	0,70 m	1,436712	27,73 °	0,71 m	1,416060427
9	25,00 °	0,71 m	1,399579	25,00 °	0,71 m	1,399578592

min	max
-----	-----

### 3.4.2. Iterative camera orientation and point cloud based developed by (Dietrich 2017a)

Dietrich developed this method in 2017 by proposing a multi-angle refraction correction approach (Dietrich 2017a). Instead of using only the height information derived from the SfM-process, Dietrich used the three-dimensional dense point cloud as well as the additional information of the camera position and view angles to apply an interactive refraction correction. During this process, the position of each point in the point cloud is reconstructed. Further, a file with the sensor and focal length of the lens data is needed to apply this refraction approach on a data set. Also, the clear water index is used to calculate the estimated real position of the points. Dietrich provides the Python script pyBathySfM v4.0 (Dietrich 2019) online and offers guidance on the implementation (Dietrich 2017b). The Python script was applied on all four data sets (SN, PA, PN and PO) resulting in four new output data set with the abbreviation PS CWI.

### **3.4.3. Bathymetric scaling for refraction correction on DSM's**

For this approach three different methods will be tested. First the refraction correction index for fresh water will be applied. The Second and third technique will be an empirical refraction correction based on the reference points measured with a DGNSS.

Applying Snell's law's simplification with the assumed SfM height and the real DGNSS height from the underwater reference points, a new refraction correction factor can be calculated. The application to the uncorrected SfM DSM is achieved by multiplying the raster cell values with the derived refraction correction factor.

The refraction function was derived through a regression analysis of points from the preprocessed point cloud and the reference points. The calculated refraction correction function can be applied to the raster data set. (Grenzdörffer and Naumann 2016, p. 848).

### **3.5. Comparison and validation**

At the beginning the resolution of the created orthomosaic's and DSM's were compared. Then the PA DSM was compared with the Lidar data to check the height differences for the captured topography. The Lidar heights at the position of the collected DGNSS points were also exported and compared with the point measurements. The results were visualized in a map with an axial color gradient highlighting the differences between them. Since on land the results of the SfM DSM are quite similar it is enough to compare only one dataset. This is followed by a comparison of the error statistics provided by Agisoft Metashape and of maps representing the subtraction of each of the three Pentacam DSM data sets with the SN DSM. Next the height values at all validation points were extracted and compared with the DGNSS measured ones.

To compare the different refraction correction methods an error static was calculated with the software Microsoft Excel. Therefore, the exported .csv-file containing the different heights at the validation-points were imported to the program to calculate the mean error and standard division for every data set. To make the empirical results visually comparable, error-histograms and scatterplots are created for all data sets

and correction methods (Butler et al. 2002, p. 431). Based on the calculated mean error and standard deviation the best result of each correction approach of the three Pentacam datasets (PA, PN, PO) was compared with the respective SN DSM. Those corrected Pentacam and SN datasets were also compared with the matching uncorrected DSM. The resulting DSM elevation difference models provide information about the spatial distribution of the elevation difference in the test site.

To retrieve additional information of the quality of the created DSM's they were also compared with the Lidar DSM.

### **3.6. Software and Hardware**

One of the needed software for this research will be Agisoft Metashape Professional in version 1.6.5 build 11249. It will be used for the photogrammetric process. This software is only available for commercial use and will be provided by Carinthia University of Applied Sciences (CUAS).

For generating the footprint of the pictures, the Python script "footprints\_to\_shapes" for Agisoft Metashape Professional will be used. It is part of a whole package of Python scripts for Agisoft Metashape and available on GitHub. The scripts can be downloaded for free (PolarNick239 2020).

The 3D point cloud and mesh processing software CloudCompare is an Open-Source project and can be used for free for this work.

As a refraction correction tool, the Python script "pyBathySfM" from James Dietrich (Dietrich 2017a, p. 357) is used. To be able to run that script, Python has to be installed. The scientific Python distribution Anaconda proves most suitable since it provides all the needed libraries ( PyQT5, NumPy, pandas, sympy, matplotlib) for the script.

Microsoft Excel's limitation to load more than 1,048,576 rows, made it necessary to look for another program to modify the larger exported .csv-files. Therefore, the software CSVBuddy in the 64-Bit version was used. It has no file size limit, however the loading and saving time will increase as the file becomes huge.

For the processing steps requiring a high processing power an Intel Xeon CPU E5-2620 v4 with 16 cores and 32 logical processors is used. It has 512GB of Ram and a Nvidia Tesla P100 graphic card with 16GB memory. Less computationally intensive processes like the Python script or excel calculations were done on a local machine with an Intel core i5-3570K with 4 cores and 4 logical processors. It has 24GB ram and an AMD Radon RX 580 graphic card with 8GB memory.

## 4. Project area

The lake Weissensee is located in Carinthia. It spreads 11.6km from east to west and 0.9km from north to south. The western part of the lake is shallower while the eastern part has also a deeper section with steep cliffs (Figure 15). The red box marks the selected area where the field experiment took place.

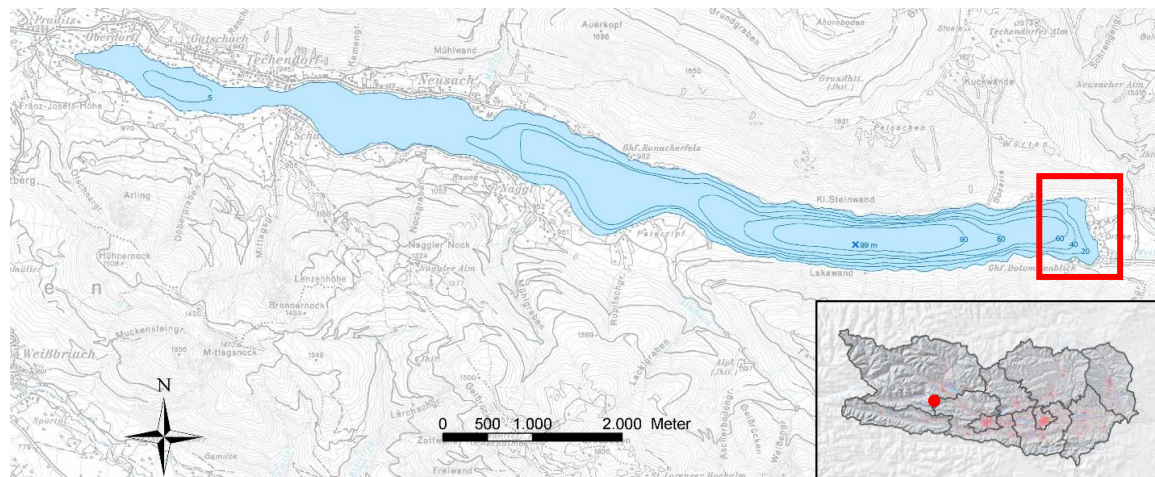


Figure 15: Overview of lake Weissensee (Amt der Kärntner Landesregierung 2020)

The selected eastern shore starts with a shallow water area, which then quickly leads to the deeper water body (Figure 16). The first onsite visit was conducted on the 1. December 2019 to confirm the estimated conditions. The collected data as e.g., roughly measured water depth and ground properties of the lake bottom help to make final adjustments while planning the field experiment.



*Figure 16: Orthomosaic Weissensee, shallow east shore and deeper water body (Amt der Kärntner Landesregierung 2020)*

#### **4.1. Lidar Data**

Further, Lidar data surveyed in the year 2011 with a resolution of 1m/pixel will be used. This data sets in form of a Digital Surface Model (DSM) and Digital Elevation Model (DEM) are provided from "Amt der Kärntner Landesregierung" as raster data. It was captured with a topographic Lidar scanner, therefore we estimated a low accuracy and precision in the areas capturing bathymetry.

## **5. Project Implementation**

This chapter consists of two main phases. Beginning with the data preparation, followed by the different data processing steps necessary for refraction correction and the creation of the validation data.

### **5.1. Data preparation**

Bevor the captured data can be used pre-processing steps are necessary to create the same conditions for every dataset.

#### **5.1.1. Images**

The captured images were stored for each sensor in a separate folder. Before they can be used, a preselection has to be executed. This has to be done because also photos from the take-off and landing phase are stored. While the UAV could manage the trigger for the Sony Alpha 7RIII camera, only one test image from the UAV ground position has to be deleted in this dataset. Because there was no connection for triggering the shutter for the Pentacam via the UAV these sensors constantly took images beginning from the take-off until it landed back on the ground. Due to this circumstance, several not useable or required images were captured. For further processing steps, only images containing sections of the project area were used.

#### **5.1.2. GCP's / DGNSS-points categorization**

The data measured with the DGNSS were exported as a \*.txt-File. In order to use the same selection of reference and control points for all datasets, a preselection and categorization of GPS data is mandatory. Therefore, a map containing all the measured points and a pre-generated orthophoto in lower resolution for better orientation was created in ArcMap. Afterward, the points were categorized into eight "GCP land reference"-points, five "GCP land validation"-points, four "GCP underwater reference"- points, twenty-seven "underwater validation"- points and eleven "wateredge"- points. Since the category "GCP underwater reference" was lacking of

points representing the shallower water areas, a DGNS point from the category "underwater validation" was transferred to the reference data set and labeled as "underwater reference"-point. Since the labeled points "GCP underwater reference" and "underwater reference" were always used as a single group, from now on they will simply be named "underwater reference points". This leads to a better distribution of the five reference points for later calculations. The final distribution of the DGNS points can be seen in Figure 17.

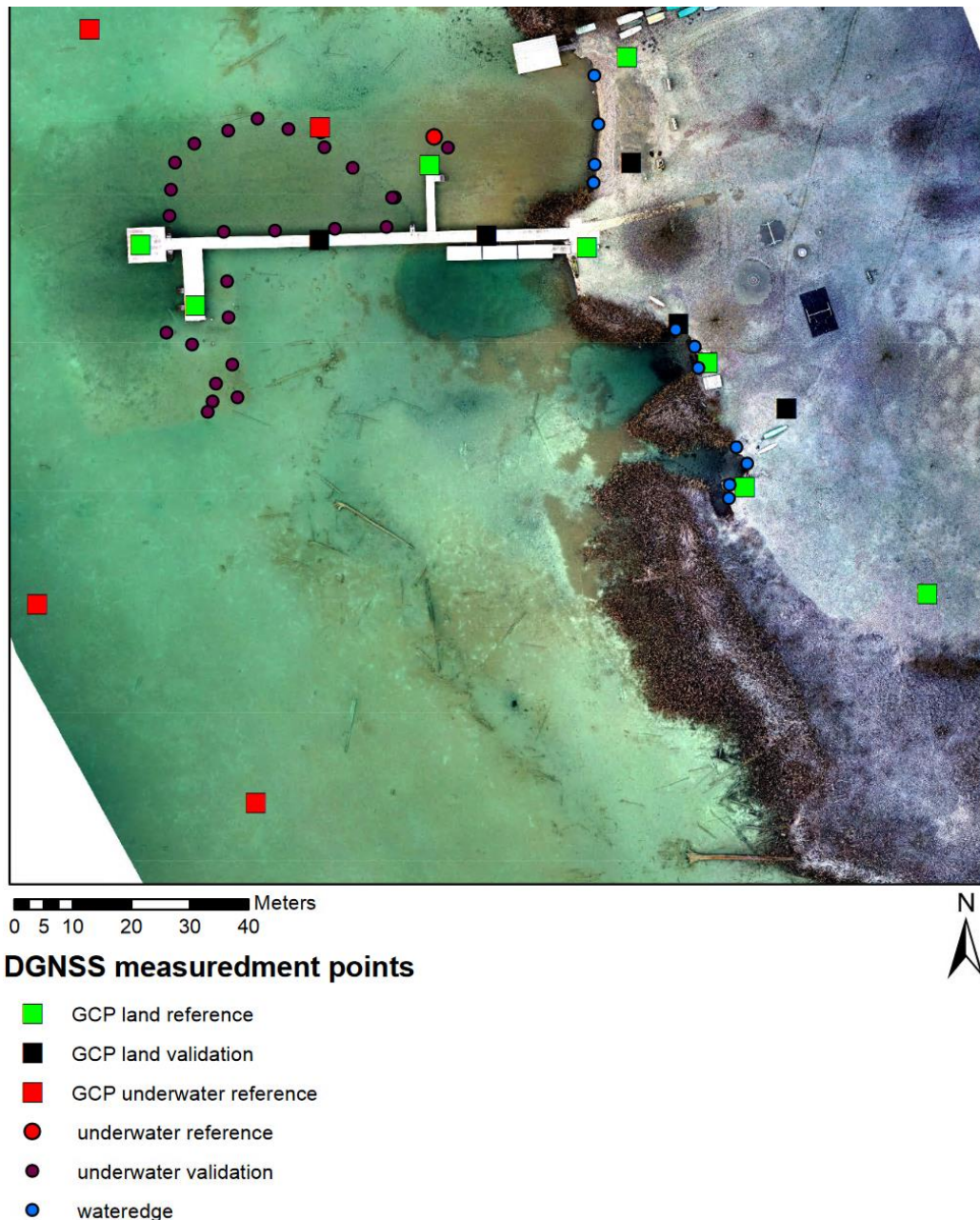


Figure 17: Orthophoto of the SN dataset with the classification of the DGNS measured points (own illustration)

## **5.2. Data processing**

This chapter describes all the processing steps necessary to execute the four refraction correction approaches. Also, the required steps to create the data for the validation process are explained.

### **5.2.1. SfM processing**

The preselected images were imported into Agisoft Metashape. Four different projects were created. The first project was used for the SfM processing of the nadir images of the Sony Alpha 7RIII (SN) camera. The second project contains all images captured during the flight with the Pentacam (PA). In each project, the corresponding images were imported. For the aligning process setting, the accuracy "high" was chosen. The rest of the settings were left as they had been set by default. Then the GNSS measured points with the type "GCP\_land" and "GCP\_water" were loaded into the program. The points were placed on the ground targets on the corresponding images. For the referencing process, only eight points measured on land were used as control points. The rest of the seventeen points were used as checkpoints. When not automatically filled out, the program was fed with the camera specifications in the menu "camera calibration".

After this step, the project PA was split into two further projects: one for only nadir images taken by the Pentacam (PN) and one exclusively for oblique photos taken by the Pentacam (PO). Splitting the project after the referencing step ensures that all further Pentacam projects have the exact same reference basis where all the GNSS points were placed exactly on the same location on the image. The alignment processes were redone since the referencing process influences this step.

As the next step in Agisoft Metashape Professional, the dense point cloud, the DEM and the orthomosaic can be calculated for each data set. This step has been conducted with the quality setting "high". Afterward, the generated data is exported for further processing with CloudCompare and ArcMap Desktop.

In addition, also the estimated coordinates of the cameras (x, y, z) as well as the estimated orientation angles of the cameras (pitch, roll, yaw) were exported as a .csv-file.

To check the captured image's actual footprint, the Python script "footprints\_to\_shapes.py "(PolarNick239 2020) was loaded into the program and executed for each nadir dataset. The resulting shapefiles were then imported into ArcMap. To check if our chosen configuration (described in 4.2.1) for our UAV-data capturing matches with the resulting data, the dimensions of the footprint as well as the overlap were measured. The overlap was then calculated in percentage.

Figure 18 visualizes the measurement for the SN data set. During the inspection of the footprint, it shows that the spacing between the footprints is not homogenous. It appears that every second footprint is closer together. When the estimated square is measured, the reason for this irregularity becomes visible. It seems that the camera was not mounted exactly in nadir direction. Instead, it was also looking slightly to one side. When the UAV flew its path up and down, the camera-view is tilted to each other, and consequently the overlap becomes bigger between those pathlines. For camera-views looking away from each other, the overlap becomes smaller. Since the overlap was chosen generously, such an occurrence should not affect the result. To check the actual flight height, the estimated mean z-value exported from Agisoft Metashape Professional was calculated with a height of 83,41m above the water surface height.

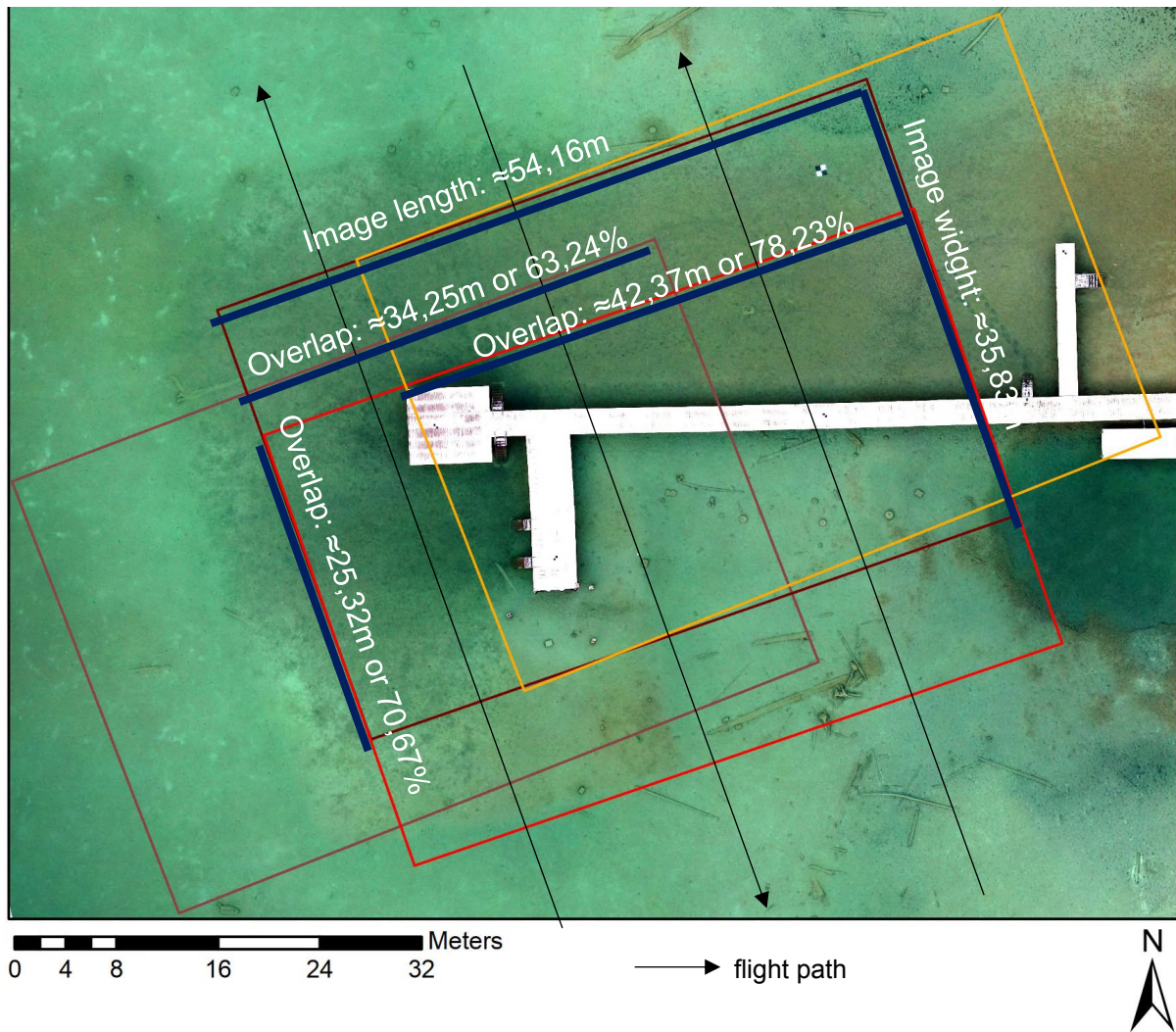


Figure 18: SN footprint with labeled footprint size and overlap (Background SN Orthomosaic, SN =Sony Nadir)  
(own illustration)

The same approach has been conducted for the nadir images of the Pentacam. Because this setup does not have any further hardware to stabilize or correct the camera's orientation, the movement of the UAV had a more significant impact on the camera view direction. This fixed setup results in larger irregularities in the overlap than already found in the dataset from the Sony Alpha 7RIII. Figure 19 represents the result of the footprint analysis for the Pentacam nadir sensor. The actual flight height above the water surface was also calculated from the estimated camera positions exported from Agisoft Metashape Professional. The sensor height for all nadir images results in an average of 89,79m above water level.

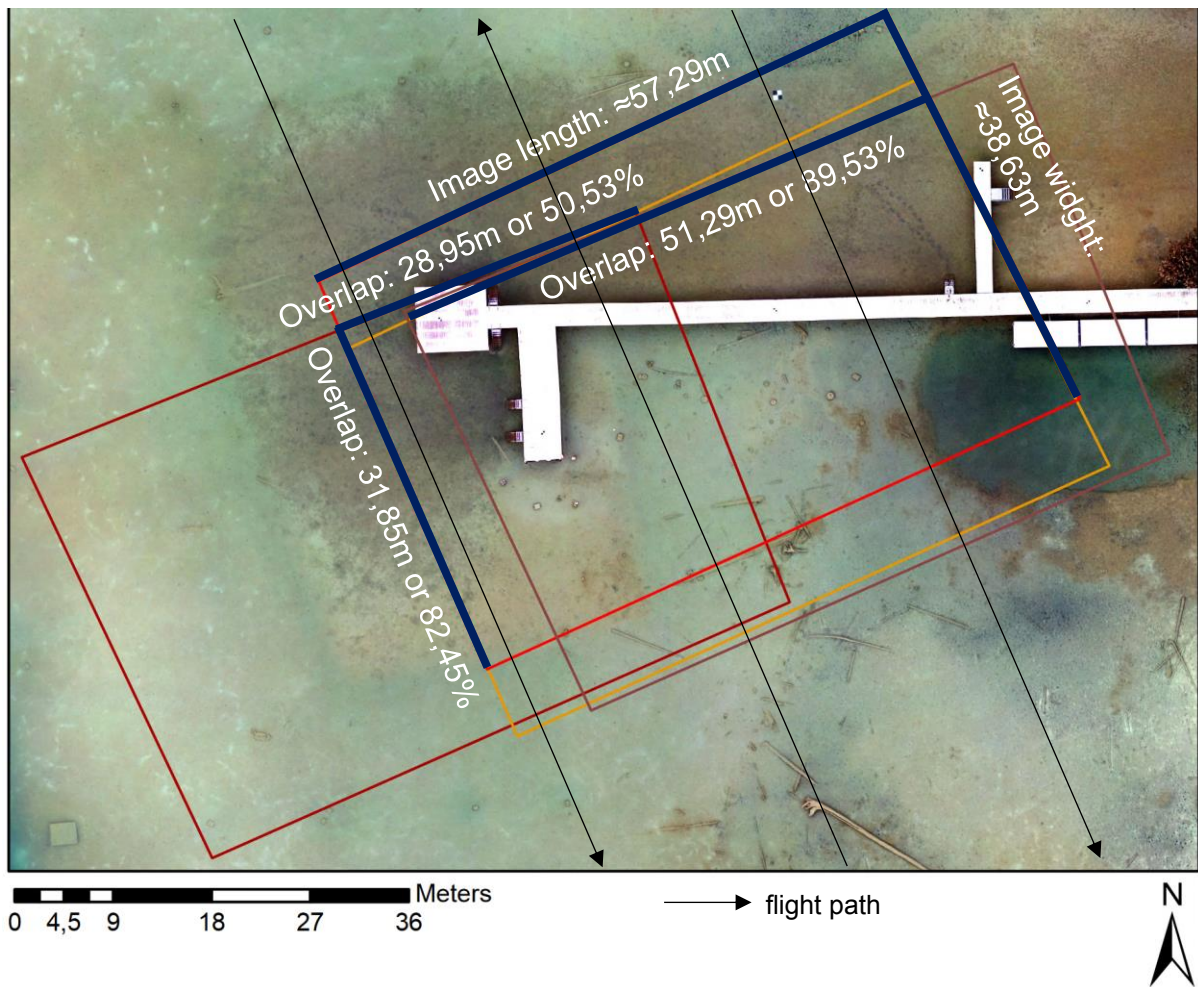


Figure 19: PN footprint with labeled footprint size and overlap (Background PN Orthomosaic, PN =Pentacam Nadir) (own illustration)

## 5.2.2. Water surface elevation

Water surface elevation is a mandatory and critical variable in the refraction correction progress. Any errors in water surface elevations translate directly as an error into the refraction-corrected depths and consequently as an error in the refraction corrected elevations (Woodget et al. 2019).

To minimize the potential of water surface elevation error, the average water level height was calculated from the mean value of 11 GPS Points measured at the water edge. The water elevation is assumed as a flat surface since the data was captured

on a lake with no surface movement during the data capturing process. The calculated mean water surface elevation is 930,618m.

A file containing the information of the water surface is mandatory for later calculations in CloudCompare, since the refraction correction is based on the water depth and not on the absolute height above sea level. Therefore, the water-depth has to be calculated by subtracting the measured absolute height from the water surface height. To generate a flat surface a .csv-file including four points positioned in the corners of the project area as x- and y- values and the average surface height as a z-value were written in Microsoft Excel.

### **5.2.3. Extracting DEM height-information at DGNSS Points**

With the tool "*Add Surface Information*" provided in the 3D analyst Toolbox of ArcMap the z-pixel-value of a DEM can be extracted to the shapefile containing the 26 GNSS measured validation points as well as the five reference points. The optional field "*method*" was kept empty. This ensures that only the z-pixel-value under the GNSS point is extracted and no other adjacent pixels were used for calculating the extracted height. The extracted z-values can then be stored in a new field. The table of the .shp-file can then be exported as an .csv-file. This is necessary to run the error statistics as a measure of accuracy and precision of the SfM data sets in Microsoft Excel.

### **5.2.4. Application of the clear water refraction index and refraction factor**

As described, correcting the water depth with the clear-water refraction index (CWI) can be a simple and quick method to get a corrected height. Before the refraction correction via index can be applied, the water depth has to be calculated. Also the refraction correction should only be applied on raster values smaller than water surface height. Therefore the "Con" function in the "Raster Calculator" tool can be used (Equation (4)).

$$\begin{aligned}
 &NewPixelValue = Con("%input raster%" \\
 &< float("%water surface height%"), float("%water surface height%") \\
 &- ((float("%water surface height%") - "%input raster%") \\
 &* float("%clear water refraction index%")), "%input raster%")
 \end{aligned}
 \tag{4}$$

For this calculation, the “*ModelBuilder*” in combination with the “*Raster Calculator*” was used in ArcMap. Figure 20 illustrates the components used in the ArcMap ModelBuilder. As clear-water refraction index the value 1,337 was used. The water surface height was rounded to three digits to 930,618m. As parameters (P) used in the model, the input raster and output raster were selected since all other input values remained the same for all four different data sets. After the correction was applied, the new z-pixel-values were again added via “*Add Surface Information*” to the 26 GNSS validation points and stored in additional fields.

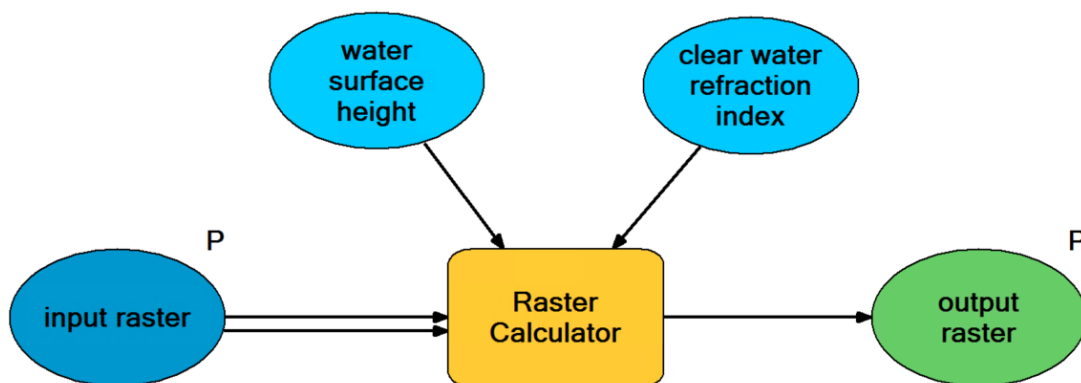


Figure 20: Illustration of the refraction correction model with clear water index in the ArcMap ModelBuilder (own illustration)

A further attempt to correct the refraction with a simple multiplication of the uncorrected water depth with a calculated factor (CF) has been conducted. This was done because the PA and PO data set include images taken in an oblique view and water areas with a greater depth than 0.2m were observed. The result from the first correction already suggests that an adapted refraction correction factor is necessary to improve the result. This factor was derived from the mean correction factor calculated from the height differences between the GPS height and the SfM raw height using the simplified

equation of Snell's law (Equation (2)) of the five underwater reference points. The resulting mean factor used for this refraction correction can be seen in Table 5.

Table 5: Calculated refraction factor, (SN =Sony Nadir, PA= Pentacam All, PN= Pentacam Nadir, PO =Pentacam Oblique)

	SN	PA	PN	PO
mean factor calculated from GCP height	1,321	1,483	1,401	1,475

The Model in ArcMap was adapted so the individual refraction factor can be provided as a parameter (P) (Figure 21). The formula inserted into the “Raster Calculator” remained the same as before (Equation (4)). The raster data sets' new surface information values were then added again to the 26 underwater validation points. After this step, they can be exported as a .csv- file to conduct the error statistics in Microsoft Excel.

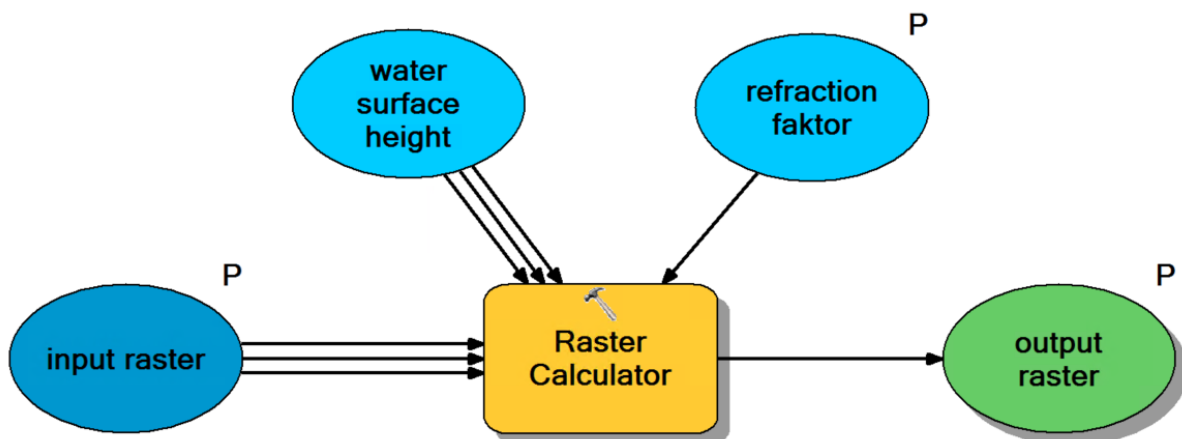


Figure 21: Illustration of the refraction correction model with individual factor in the ArcMap ModelBuilder (own illustration)

### 5.2.5. Empirical correction with a linear equation

In order to derive a regression function, the five underwater reference points were used again to correct the refraction (Figure 22). With this function, it is possible to influence the linear regression angle between the measured and SfM processed elevation.

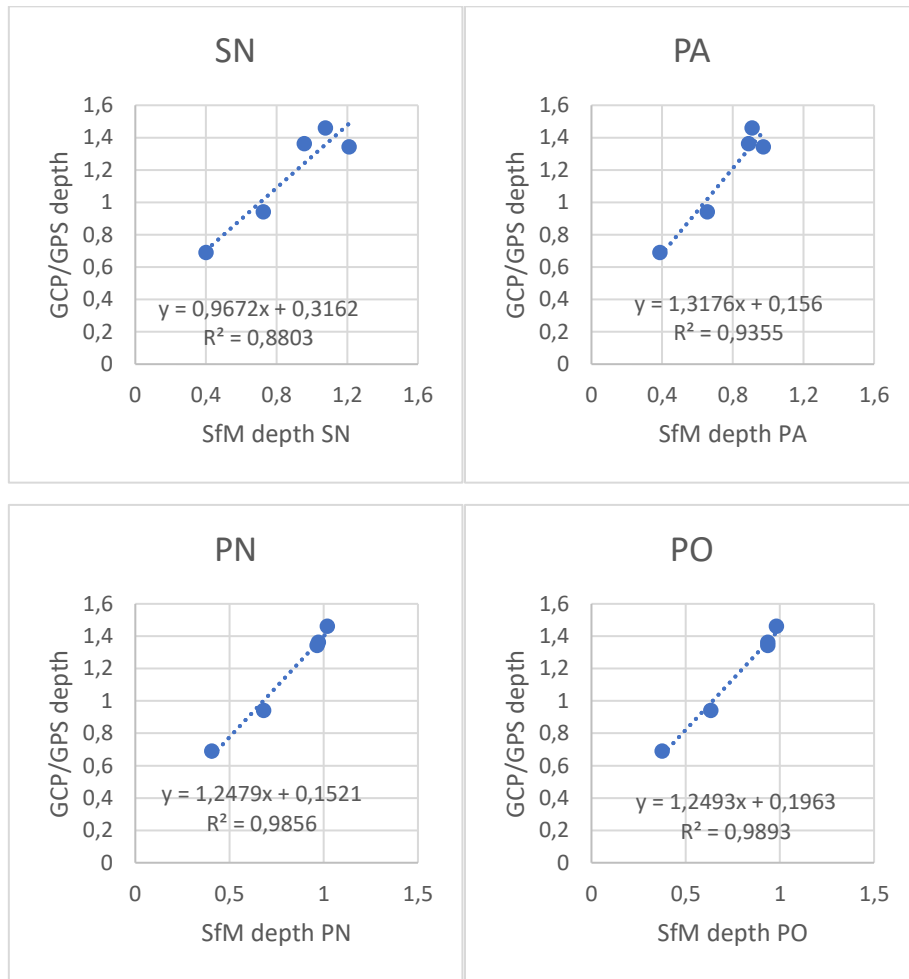


Figure 22: Linear regression function for the different data sets, (SN =Sony Nadir, PA= Pentacam All, PN= Pentacam Nadir, PO =Pentacam Oblique)

To implement this function into the “*ModelBuilder*”, further adaptations had to be done (Figure 23). The additional added parameter (P) “*y-intercept*” and “*slope*” made a further adjustment to the formula used in the “*Raster Calculator*” necessary (Equation (5)). The surface information from the new raster data can then be added to the 26 validation points.

$$\begin{aligned}
&NewPixelValue = Con("%input raster%" \\
&< float(%water surface height%), float(%water surface height%) \\
&- (((float(%water surface height%) - ("%input raster%")) \\
&* float(%Slope%)) + float(float(%y \\
&- intercept%))))), "%input raster%"
\end{aligned}
\tag{5}$$

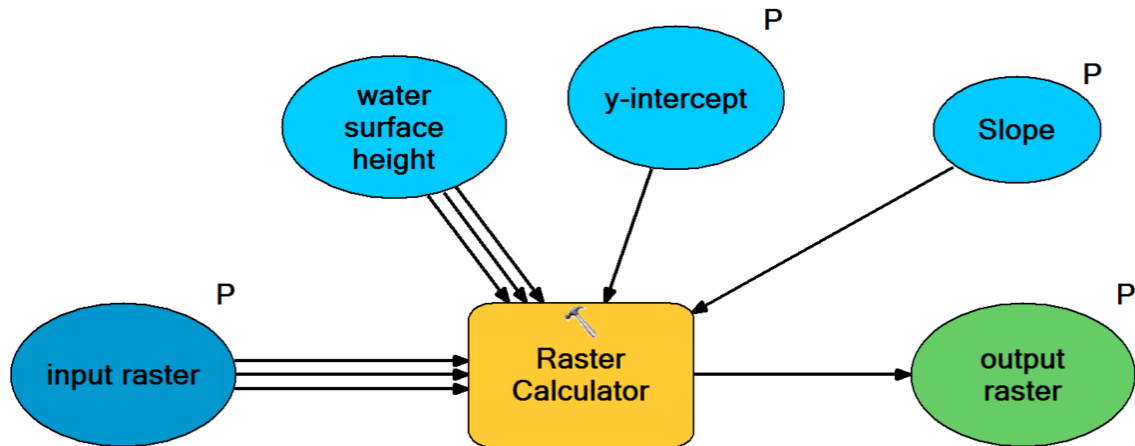


Figure 23: Illustration of the refraction correction model with the regression function in the ArcMap ModelBuilder (own illustration)

### 5.2.6. Multi-View refraction correction (pyBathySfM)

pyBathySfM V4.0 (Dietrich 2019) uses .csv-files as data input. For the preprocessing, the point clouds were imported as “.las-file” into CloudCompare. The following steps were executed as described in the available tutorial on GitHub (Dietrich 2017b) with some necessary adaptations because this tutorial describes the process for a river bathymetry. To provide the water-surface information in CloudCompare a .csv-file is necessary. It has to provide the x-,y- and z- coordinates of several points to create a surface. In our case, four corner points forming a polygon which overspans the whole project area and the water-surface height as z-value were written in a .csv-file. After importing it to CloudCompare, the z-value is added as a scalar field and a mesh Delaunay 2.5 (xy plane) is generated.

Before the first processing steps are conducted on the raw SfM point cloud, any extra scalar fields can be deleted. As a first step, the raw SfM point cloud gets subsampled. This is necessary to limit the influence of noise in the point cloud. Therefore, a minimum elevation filter is used and the point spacing is set to 0,05m. As a next step, the rasterize tool is used again with a 0,05m cell size. To calculate the water depth, both the water surface mesh and the point cloud need to be selected. Then the cloud to mesh distance can be calculated. This adds a new scalar field with the depth to the point cloud. Now all the points with a depth value below 0 are filtered out to keep only underwater points. As the largest negative value -5m is chosen. To clean the extant point cloud and keep the further processed section identical for all four data sets, a polyline is drawn roughly along the waterline and the rest of the underwater data. This polyline can then be used for all datasets. As the last step, the water depth and underwater surface height are summed up to convert them to the surface height. Before the processed point cloud is exported, the generated scalar fields are renamed, and any extra scalar fields generated during the processing steps but not needed for the Python script were deleted to keep the saved .csv-file as small as possible. Since the exported files still had too many rows for MS Excel, the program CSVBuddy was used for additional data changes and checking.

Besides the point cloud, also the corresponding camera orientation and camera information file need to be provided for the Python script. Except for one additional run with the PO data set, the Python script was executed without the option "Filtered depth values". This option was implemented to cut off the calculations if the camera's view angle on one point of the point cloud gets bigger than 35° or the distance between them gets bigger than 100m to improve the outcome (Dietrich 2019). Therefore, the PO data set was the perfect fit to examine the effect of this option for the Python script "byBathySfM V4.0".

The output file of the Python script has then been reimported to CloudCompare. To be able to do further investigations and comparisons the point cloud has to be rasterized. Since the point cloud was subsampled with a 5cm spacing, they are spread evenly but not all grid positions are filled with points. Exporting such a point cloud to a raster-image with the same resolution would lead to empty cells. To fill those empty cells the option "interpolate" at the advanced parameters "empty cells" can be chosen. This

option consists of a linear interpolation with the nearest non-empty neighboring cells within the convex hull of non-empty cells. Since all the points above the waterline were removed, this also includes areas like the jetty. After updating the grid, the DSM can be exported as a raster-file.

The created DSM was then imported into ArcMap Desktop. After defining the projection, the surface information was added to the “.shp-file” of the 26 underwater validation points. Therefore, new extra fields were created. For the purpose of error statistics, the table of the shapefile was exported as a .csv-file and imported to Microsoft Excel.

### **5.2.7. Empirical error statistic**

For the empirical error statistic, the mean error, min error, max error and standard deviation from the height information of each data set in comparison to the DGNSS data at the 26 points underwater validation points were calculated. Further, two types of diagrams were created based on this information. The created error histogram and scatterplot for each data set should visualize the difference in precision and accuracy.

### **5.2.8. Comparison of the different DSM's**

The created SfM-DSMs were also compared with each other. Since during the processing steps a lot of DSMs were created, a selection was necessary to reduce the number of comparisons. For this selection the precalculated error statistic was used to pick the DSM for each correction approach of the Pentacam dataset with the lowest value of mean error and standard deviation. The chosen DSMs were compared with the uncorrected DSMs as well as with the DSMs of the other sensor corrected with the same approach. With the subtraction of dose datasets different DSM elevation difference models were created. This provides the information of the spatial distribution of the elevation difference in the test site.

### **5.2.9. Comparison with the Lidar data**

Comparing the created SfM-DSM with the existing lidar data set serves as an inspection of the generated height information. Therefore, both Lidar datasets (DEM, DSM) were inspected and compared with the clear water index refraction corrected PA DSM. Since the refraction correction had no influence above the water surface, all PA DSM were the same at this section. For this comparison, any other DSM dataset created during the SfM process could have been used because the derived heights were quite similar on the land part. It turned out that the data acquisition was at a time when the trees grew leaves. Therefore, the height difference between this DSM and our SfM-DSM shows more significant deviations on areas trees and bushes. The DEM, on the other hand, misses the height information of the buildings, which were captured with the SfM method. Since the building didn't play a role for this thesis, further comparisons were conducted with the DEM lidar data set.

During this comparison, a height difference between the SfM data and the Lidar data could be observed. Further investigations at the measured DGNSs measured points on land showed an average deviation of roughly 1,3m. To investigate this error and confirm correct DGNSs, measurements at additional points were collected at the test site. These measurements show no evidence that the DGNSs points were incorrect.

## 6. Results

As a result, three different refraction correction approaches were applied on the four different datasets, SN, PA, PN and PO. For the correction with the simplified Snell's law, a second attempt with calculated variables instead of the clear water index was executed. The reason was that especially the datasets containing oblique camera views (PA and PO) had more significant errors than the nadir datasets. This behavior was expected since the precalculations of the different refraction factors in chapter "3.4.1 Considerations of the Influence of camera angles on refraction" show that the camera setup with a 25° oblique view requires a factor between 1,35 and 1,62. By calculating the new factor from the DGNS data and the raw SfM data, better accuracy for data sets with oblique views could be achieved.

After the results of the refraction correction via pyBathySfM were checked, an additional run with the PO data set and a refraction index of 1,4 instead of the default 1,337 was executed. The value 1,4 corresponds to the refraction variable at exact 25° oblique view.

### 6.1. Captured Data

This chapter summarizes all the information about the captured data as well as information about the accuracy and precision of the SfM-Data on land. It also gives a first impression of the underwater height error caused by refraction.

#### 6.1.1. UAV captured images

The final selection includes 242 photos for the Sony Alpha 7RIII and uses 5,92GB of storage. The storage size of a single image varies between 19MB and 33,1MB. For the Pentacam 1397 photos with a single image size between 2,56MB and 9,52MB and an overall storage use of 8,56GB were used. This data set is further split into 289 pictures captured in nadir and 1108 photos taken in an oblique view (Table 6).

Table 6: Overview used image data for SfM processing

	<b>Sony Alpha 7RIII</b>	<b>Pentacam</b>
<b>Nadir images used</b>	<b>242</b>	<b>289</b>
<b>Oblique images used</b>	-	<b>1108</b>
<b>Single image size</b>	<b>19MB-33,1MB</b>	<b>2,56MB-9,52MB</b>
<b>Storage size of all used images</b>	<b>5,92 GB</b>	<b>8,56 GB</b>

### 6.1.2. DGNSS measured points

During the DGNSS measurements 55 points with an estimated accuracy of +/- 1cm were collected. Table 7 shows the final number of the used points in each category.

Table 7: DGNSS point measurements and numbers by category

<b>point category</b>	<b>number measured</b>
<b>GCP land reference</b>	<b>8</b>
<b>GCP land validation</b>	<b>5</b>
<b>GCP underwater reference</b>	<b>4</b>
<b>underwater reference</b>	<b>1</b>
<b>underwater validation</b>	<b>26</b>
<b>wateredge</b>	<b>11</b>
<b>sum</b>	<b>55</b>

### 6.1.3. Raw SfM data and GCP point comparison

The result of the raw SfM data in comparison to the land validation and underwater reference DGNSS point measurements on the metal plates (Figure 24) shows the accuracy of the created SfM-data on land and the refraction effect underwater. While the SfM heights of the different datasets almost match with the DGNSS on land, they are not matching with the points measured underwater( Table 8). The result also indicates that the accuracy and precision of the three Pentacam datasets (PA, PN, PO) on land is slightly better than from the SN data set.

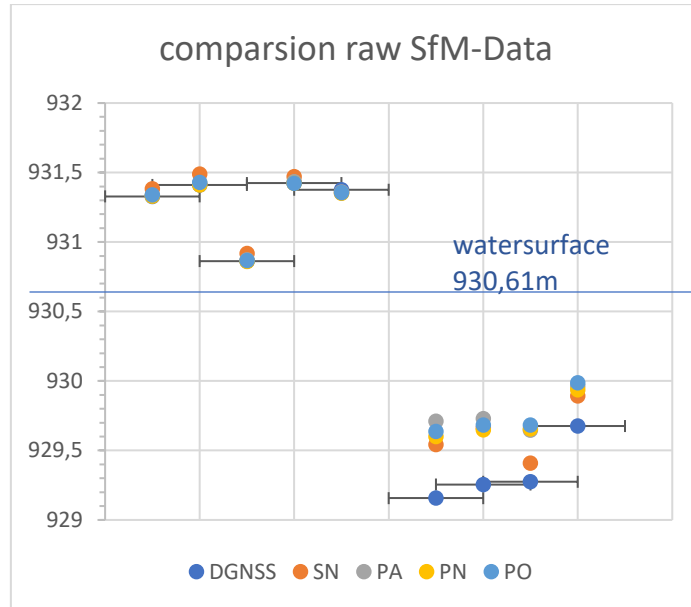


Figure 24: Uncorrected SfM derived heights compared to GCP heights (own illustration)

Table 8: Error statistic for raw SfM data on land and under water, (SN =Sony Nadir, PA= Pentacam All, PN= Pentacam Nadir, PO =Pentacam Oblique)

	mean error	min error	max error	standard deviation
SN land	-0,042m	0,020m	-0,079m	0,037m
SN water	-0,286m	-0,135m	-0,407m	0,132m
PA land	-0,005m	-0,006m	0,015m	0,012m
PA water	-0,422m	-0,288m	-0,553m	0,116m
PN land	0,021m	0,018m	0,051m	0,030m
PN water	-0,369m	-0,261m	-0,442m	0,077m
PO land	-0,002m	0,002m	0,020m	0,015m
PO water	-0,407m	-0,310m	-0,480m	0,071m

### 6.1.4. Water surface height

The mean water surface height derived from eleven DGNSS points at the water edge was calculated with a mean height of 930,62m. Table 9 shows a minimal measured height of 930,59m, a maximum height at 930,64m and the standard deviation calculated with 0,0128m.

Table 9: Error statistic water surface height

	mean height	min height	max height	standard deviation
Water surface height	930,618m	930,592m	930,638m	0,013m

## 6.2. SfM evaluation

For checking the quality of the uncorrected SfM data, the report function of Agisoft Metashape Professional was used. It allows to export a .pdf-file containing different information about the survey data (Figure 25), camera calibration, ground control points, digital elevation model, as well as all the processing parameters. The four complete reports will be attached at the end of this work.

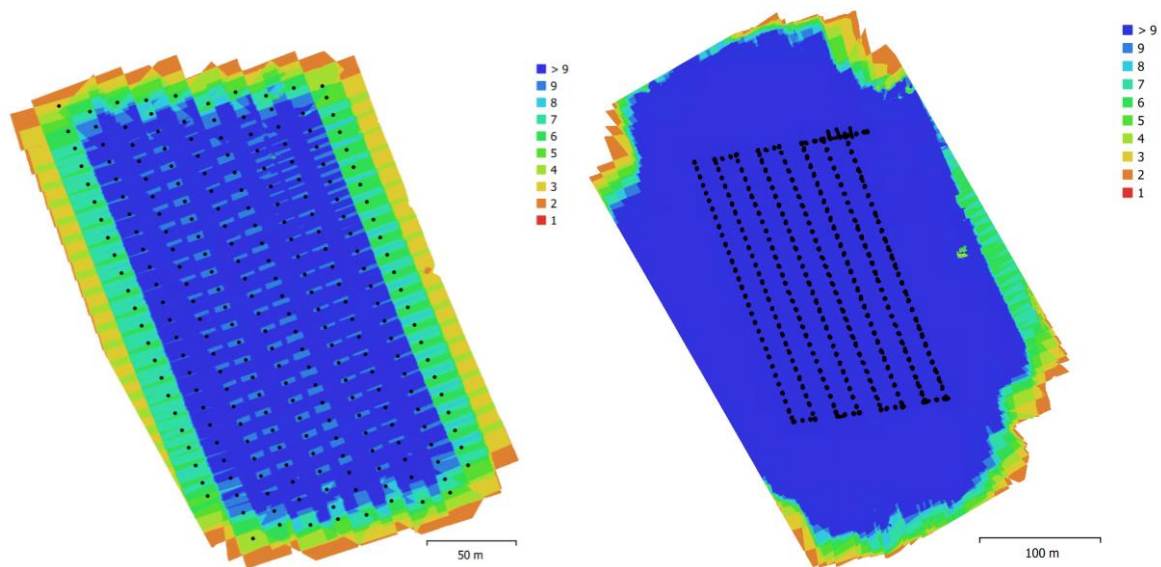


Figure 25: Camera location and image overlap Agisoft Metashape Professional Report, left SN

Table 10 includes all total error values of the reference points for x, y and z for the four different data sets. In Agisoft Metashape Professional, those reference points were called control points. The complete reports can be found in the Appendix H: - Appendix K:.

Table 10: Agisoft error statistic, Root Mean Square Error (RMSE)

<b>RMSE of 8 Control points</b>					
	<b>x error</b>	<b>y error</b>	<b>z error</b>	<b>XY error</b>	<b>Total</b>
<b>SN</b>	<b>1,05cm</b>	<b>0,78cm</b>	<b>2,60cm</b>	<b>1,31cm</b>	<b>2,92cm</b>
<b>PA</b>	<b>0,93cm</b>	<b>0,77cm</b>	<b>1,69cm</b>	<b>1,21cm</b>	<b>2,08cm</b>
<b>PN</b>	<b>0,65cm</b>	<b>0,67cm</b>	<b>0,22cm</b>	<b>0,93cm</b>	<b>0,96cm</b>
<b>PO</b>	<b>1,69cm</b>	<b>1,04cm</b>	<b>1,61cm</b>	<b>1,99cm</b>	<b>2,55cm</b>
<b>RMSE of 9 Check points</b>					
	<b>x error</b>	<b>y error</b>	<b>z error</b>	<b>XY error</b>	<b>Total</b>
<b>SN</b>	<b>14,50cm</b>	<b>4,62cm</b>	<b>19,94cm</b>	<b>15,22cm</b>	<b>25,08cm</b>
<b>PA</b>	<b>6,79cm</b>	<b>11,93cm</b>	<b>28,58cm</b>	<b>13,72cm</b>	<b>31,71cm</b>
<b>PN</b>	<b>6,86cm</b>	<b>12,89cm</b>	<b>23,28cm</b>	<b>16,61cm</b>	<b>27,49cm</b>
<b>PO</b>	<b>8,28cm</b>	<b>12,15cm</b>	<b>27,14cm</b>	<b>14,71cm</b>	<b>30,87cm</b>

To visualize the differences between the four different data sets the SfM DSM derived from the Sony Alpha 7RIII is compared with the three SfM DSM data sets from the Pentacam. The hole maps can be seen in Appendix C: SfM DSM uncorrected comparison (Figure 43-Figure 45). The calculated linear regression functions from each data set are not parallel to each other, resulting in depth-dependent deviations. The DSM from the Sony Alpha 7RIII show higher elevation values in shallower water areas than the DSM from the Pentacam. The most significant difference could be observed between the two data sets consisting of Nadir images.

### 6.2.1. Orthomosaic

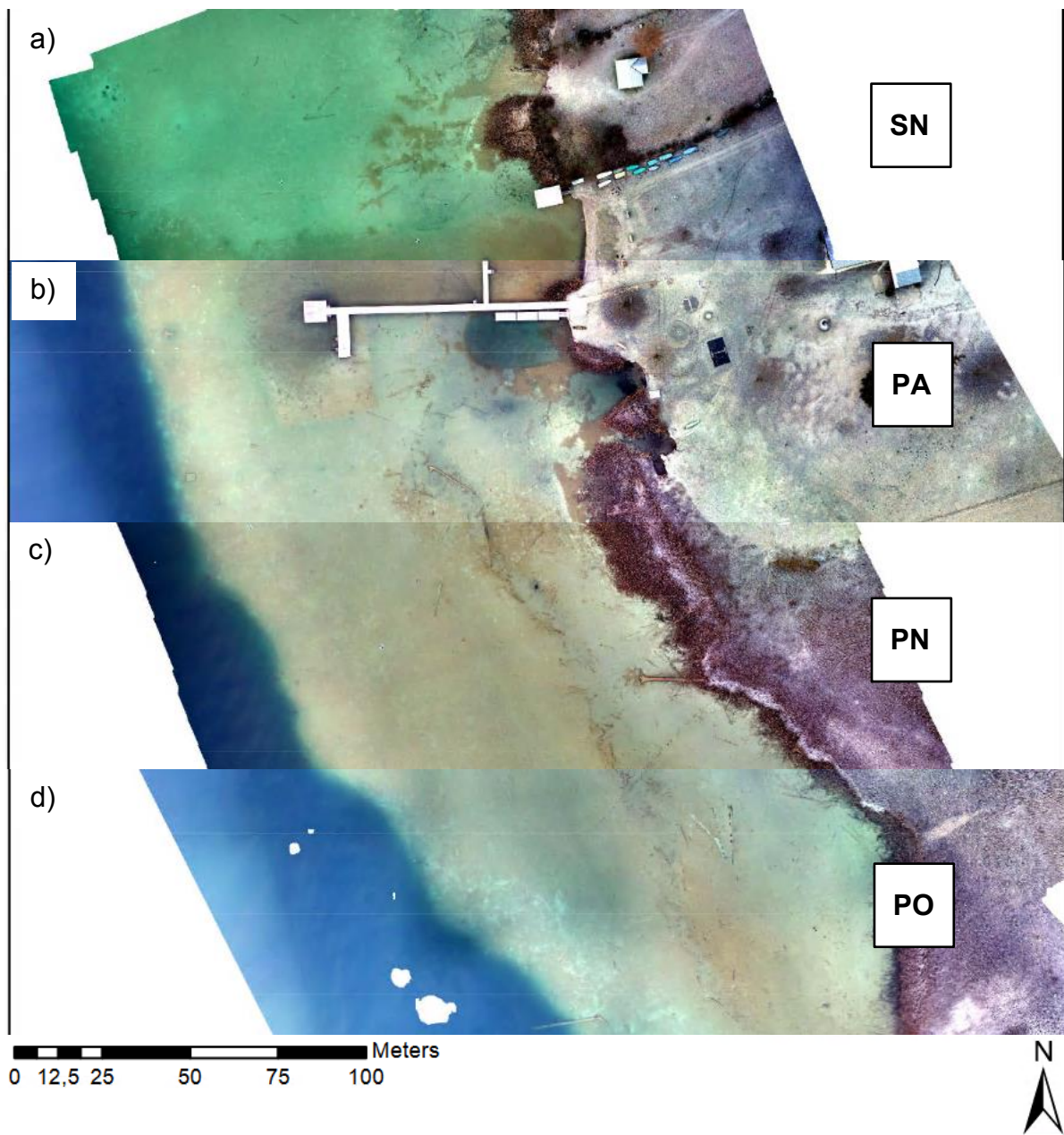


Figure 26: Sections of the orthomosaic from the four data sets: a) SN =Sony Nadir, b) PA= Pentacam All, c) PN= Pentacam Nadir, d) PO =Pentacam Oblique (own illustration)

For every data set, an orthomosaic has been calculated (Figure 26). It gives an overview of the observed area and also can show if the alignment in Agisoft Metashape worked properly. The possible resolutions for building an orthomosaic are listed in Table 11 for each data set. It depends on the ground sampling resolution and therefore, the data set captured with the Sony Alpha 7RIII has a much higher possible

resolution than the data set captured with the Pentacam. Since the distance between the camera and the captured area is bigger when taking images in oblique view, the ground sampling distance is also smaller. This is why the PN data set has a higher possible resolution than the PA or PO data set.

*Table 11: Highest possible orthomosaic resolution for the four different data sets, (SN =Sony Nadir, PA= Pentacam All, PN= Pentacam Nadir, PO =Pentacam Oblique)*

<b>data set</b>	<b>highest possible resolution</b>
<b>SN</b>	<b>0,67 cm/pixel</b>
<b>PA</b>	<b>1,19 cm/pixel</b>
<b>PN</b>	<b>1,07 cm/pixel</b>
<b>PO</b>	<b>1,23 cm/pixel</b>

For the building process, a unified resolution of 2cm/pixel was selected. Figure 27 shows a picture section of one Ground Control Plate (GCP) underwater in more detail for each data set. The expansion of the various orthomosaic differs between each data set (Appendix A: Orthomosaic, Figure 35-Figure 38). This area difference is caused by the slightly different travel path the UAV took while capturing the images with the Sony Alpha 7RII and the Pentacam and the various camera views which have been captured with the Pentacam.

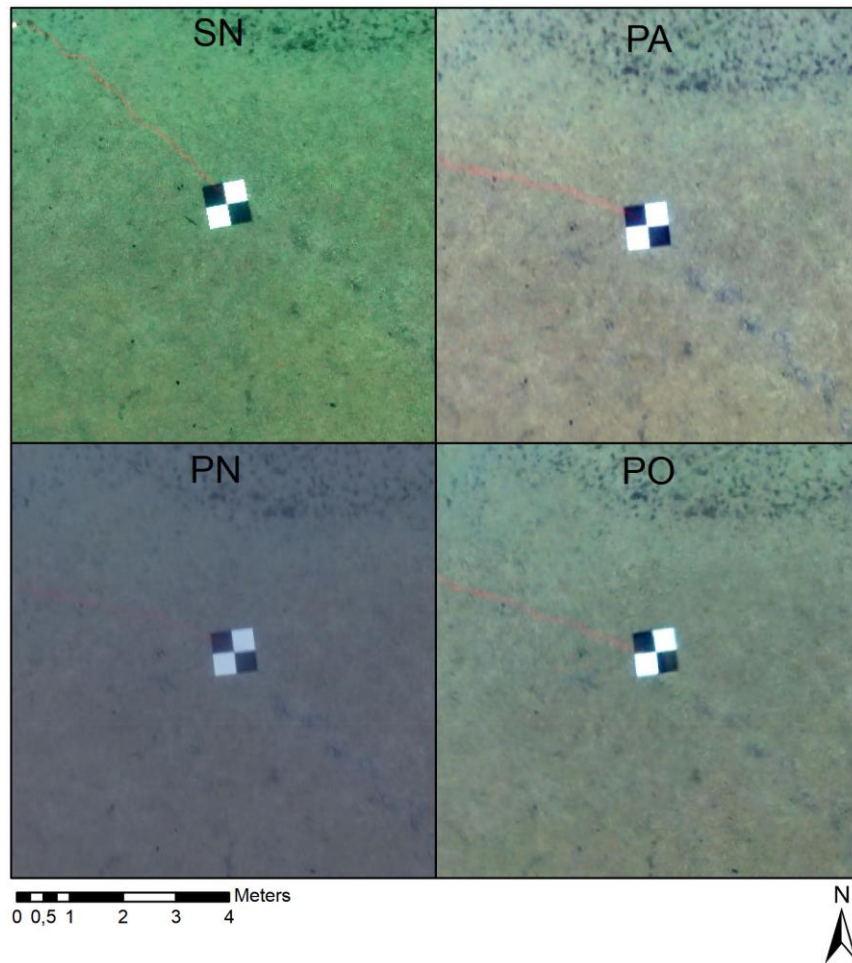


Figure 27: Detailed image section of one Ground Control Point plate (1mx1m) represented in an orthomosaic for each data set with a 2cm/pixel resolution (own illustration), (SN =Sony Nadir, PA= Pentacam All, PN= Pentacam Nadir, PO =Pentacam Oblique)

### 6.2.2. 3D Point clouds

The point clouds for each dataset created in Agisoft Metashape were exported as a “.las”-file. It is based on the dense point cloud which was generated with the setting “high”. This is the second-highest setting that can be chosen in this step. Table 12 represents the different point densities and numbers for all four datasets.

Table 12: Point cloud density and number for the four different data sets, (SN =Sony Nadir, PA= Pentacam All, PN= Pentacam Nadir, PO =Pentacam Oblique)

data set	point density	number of points
SN	0,550 points/cm <sup>2</sup>	424346033 points
PA	0,176 points/cm <sup>2</sup>	209246129 points
PN	0,220 points/cm <sup>2</sup>	174765512 points
PO	0,166 points/cm <sup>2</sup>	201010844 points

### 6.2.3. Digital Surface Model

The DSM was exported in Agisoft Metashape Professional for every data set. Other than the Orthomosaic, the resolution of the DSM is based on the dense cloud which was generated with the setting "high". Therefore, the output of the DSM will be two times lower than the resolution of the Orthomosaic. This setting was a compromise between a high resolution and a data size which was processable with our machines. The exact values can be seen in Table 13.

Table 13: DSM resolution for the four different data sets, (SN =Sony Nadir, PA= Pentacam All, PN= Pentacam Nadir, PO =Pentacam Oblique)

data set	resolution
SN	1,35 cm/pixel
PA	2,38 cm/pixel
PN	2,13 cm/pixel
PO	2,45 cm/pixel

Additionally, a DSM with the water depth values was calculated for better comparability of the different datasets (Figure 28). The maps representing the whole test site can be found in Appendix B:SfM water depth DSM uncorrected: Figure 39 - Figure 42.

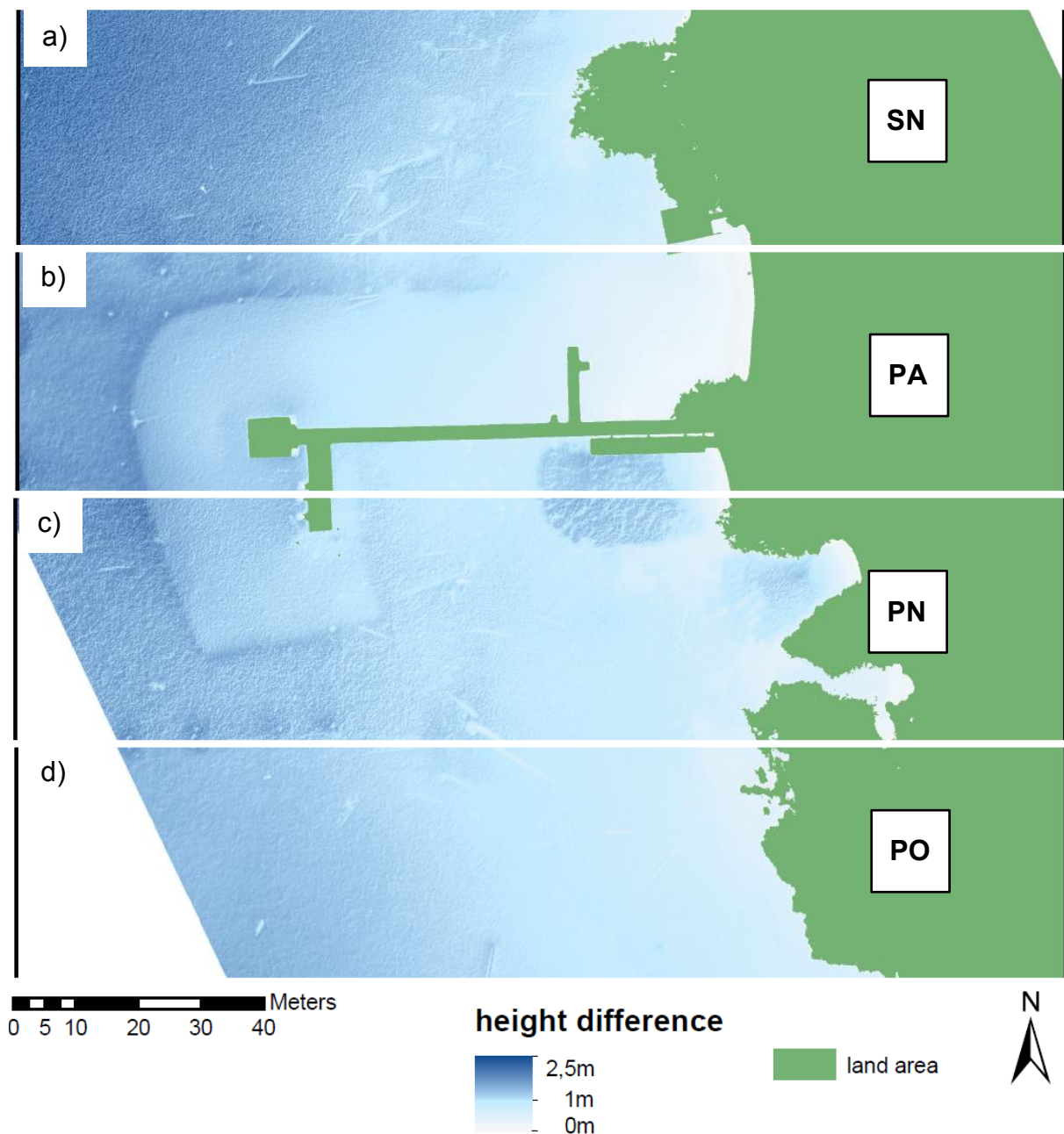


Figure 28: Sections of the water depth height SfM DSM from the four data sets: a) SN =Sony Nadir, b) PA= Pentacam All, c) PN= Pentacam Nadir, d) PO =Pentacam Oblique (own illustration)

### 6.3. SfM refraction correction

Table 14 gives a good overview of the performance of the uncorrected datasets as well as of the different refraction correction approaches applied to the different datasets. Figure 29 graphically presents the refraction correction accuracy and precision as an example for the refraction correction with the calculated factor by

comparing the different datasets and refraction correction approaches. All detailed graphical results for the refraction correction approaches as well as for the uncorrected SfM data can be found in Appendix G: Error histogram and scatterplot.

Table 14: Depth error statistic comparison for different refraction approaches on four different data sets

Dataset and correction approach	mean error	min error	max error	standard deviation [m]
SN uncorrected	0,2459m	0,1295m	0,3242m	0,0458m
PA uncorrected	0,3031m	0,1504m	0,4157m	0,0645m
PN uncorrected	0,2615m	0,1288m	0,3680m	0,0574m
PO uncorrected	0,3111m	0,1638m	0,4293m	0,0641m
SN CWI	-0,0134m	0,0041m	-0,0944m	0,0491m
PA CWI	-0,0899m	-0,0341m	-0,1397m	0,0280m
PN CWI	-0,0343m	-0,0053m	-0,0669m	0,0235m
PO CWI	-0,1006m	-0,0221m	-0,1489m	0,0296m
SN CF	-0,0059m	-0,0022m	-0,0887m	0,0501m
PA CF	0,0090m	0,0004m	0,0495m	0,0225m
PN CF	0,0089m	0,0004m	0,0771m	0,0226m
PO CF	-0,0097m	-0,0037m	0,0654m	0,0260m
SN LRF	0,0274m	-0,0012m	0,1363m	0,0439m
PA LRF	0,0094m	-0,0001m	0,0500m	0,0225m
PN LRF	0,0043m	-0,0007m	0,0734m	0,0241m
PO LRF	-0,0025m	0,0022m	0,0745m	0,0264m
SN PS CWI	-0,0003m	0,0023m	0,1013m	0,0501m
PA PS CWI	-0,0439m	0,0028m	-0,0905m	0,0237m
PN PS CWI	-0,0044m	0,0042m	-0,1042m	0,0557m
PO PS CWI	-0,0471m	0,0004m	-0,0857m	0,0287m
PO PS CWI depth-filtered	-0,0688m	0,0056m	-0,1055m	0,0284m
PO PS 1,4	0,0005m	0,0001m	0,0795m	0,0295m
<p>(SN =Sony Nadir, PA= Pentacam All, PN= Pentacam Nadir, PO =Pentacam Oblique, CWI = clearwater index, CF = calculated factor, LRF= linear regression function, PS CWI= Python script with clearwater index, PS 1,4 = Python script with refraction factor 1,4)  The green filling indicates the two best results for each correction method.</p>				
			best result	second best result

Figure 62 represents the correction with the clear water index (CWI). We observe a higher accuracy for the nadir data sets than for the data sets, including oblique camera images. On the other hand, the precision from the Sony Alpha 7RIII was worse than from all the different data sets of the photos captured with the Sony ILCE-QX1 sensor

on the Pentacam. The Pentacam data set using only the nadir camera view got the most precise output with a standard deviation of 0,034m.

To check how much a calculated refraction index (CF) can influence the output, in Figure 29, the refraction correction error statistic with a calculated mean index of five GPS points is represented. This approach increased the accuracy for all four data sets. For the two data sets taken by the Pentacam also the precision could be improved while it dropped for the Sony Alpha 7RIII data set.

While the regression function's slope matches quite well for the three Pentacam datasets, it did not match the Sony Alpha 7RIII data set. Correcting the refraction with an equation offers an option to influence the slope of the regression function. Figure 64 represents the refraction correction based on a linear regression function (LRF). In our case, the result for the Sony Alpha 7RIII was a too steep regression function. The outcome for the Pentacam data sets on the other hand shows better results with lower mean and standard deviation values.

Figure 65 and Figure 66 show the result of the validation points from the multi-view refraction correction. In Figure 65 the four data sets SN, PA, PN and PO are compared, while in Figure 66 the results of different settings in the pyBathySfM script for the PO data set are represented. Correcting the refraction via Python script results in a similar outcome as the simple correction via clear water index. Both data sets containing only nadir images delivered good results right away. After testing the depth filtering option in the Python script, a third run was executed. This time the precalculated refraction variable corresponded with the value calculated for point 9 of the 25° oblique view in “3.4.1 Considerations of the Influence of camera angles on refraction”. As Figure 66 displays, the option for filtering the depth and distances and cutting off the calculation does not improve the result, while the change of the refraction index results in the best overall output for this multi-view correction approach.

To see the differences of the four correction methods within one data set Figure 30 illustrates the error histograms and scatterplots of the PA dataset.

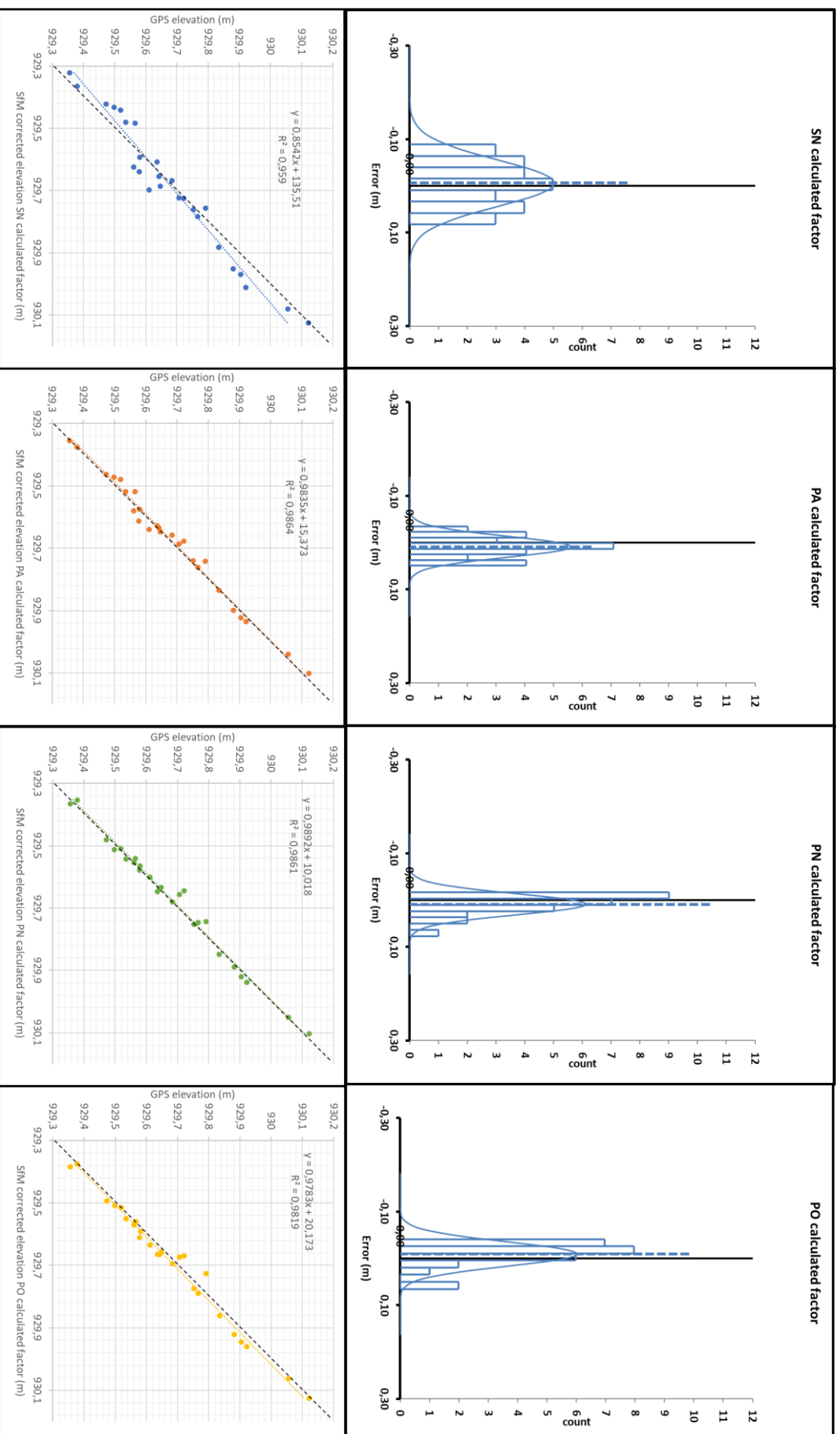


Figure 29: Error histograms and scatterplots for all four datasets corrected with the calculated factor (SN = Sony Nadir, PA = Pentacam All, PN = Pentacam Nadir, PO = Pentacam Oblique) (own illustration)

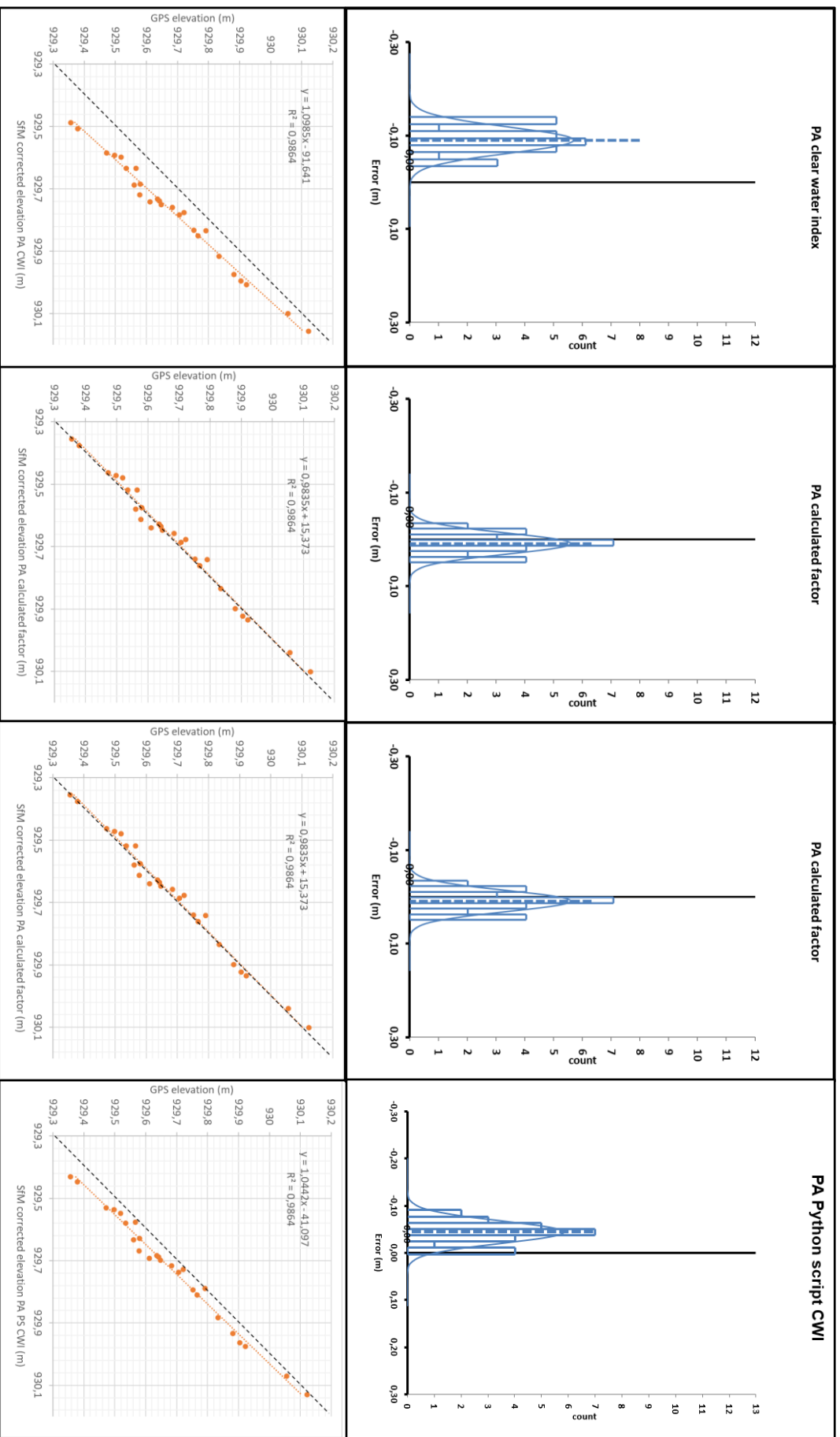


Figure 30: Error histograms and scatterplots for the PA=Penacam All datasets corrected with the four different correction methods (own illustration)

#### **6.4. DSM data comparison**

Based on the results in Table 14 we created DSM comparison maps in ArcMap Professional. The result of the comparison with the uncorrected DSMs shows that the linear regression function caused almost a constant height increasing between 0,2m and 0,3m over the hole bathymetric test site for the SN data set (Figure 32c)). All other maps show an increase of height difference with increasing water depth, which equals the expected results(Figure 31:a)-d) & Figure 32:a),b),d)).

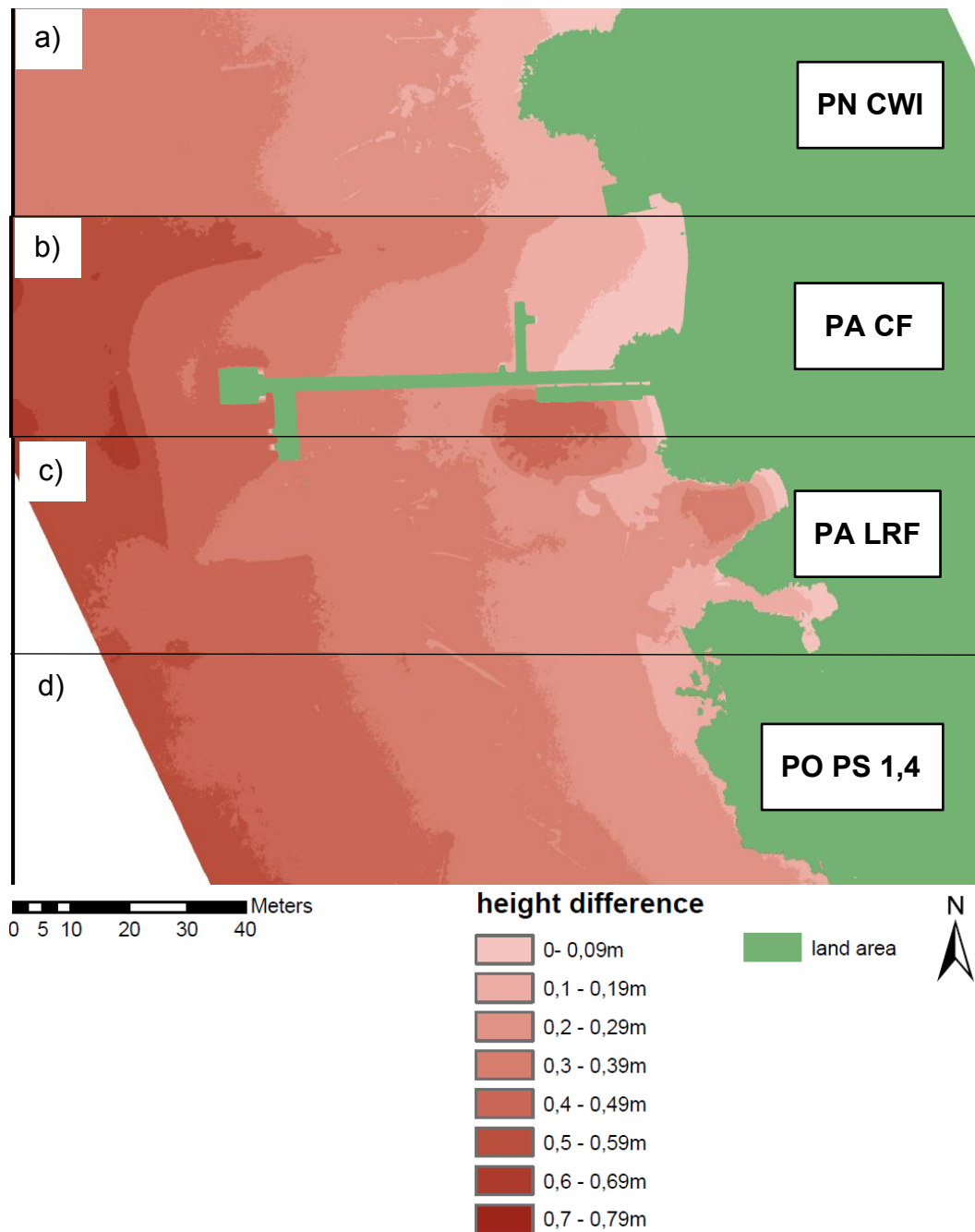


Figure 31: Sections of Pentacam refraction corrected DSMs minus Pentacam uncorrected DSMs a) PN clear water index corrected – PN uncorrected, b) PA derived factor corrected – PA uncorrected c) PA regression function corrected – PA uncorrected d) PO iterative Python script (index = 1,4) corrected - PO uncorrected (PA= Pentacam All, PN= Pentacam Nadir, PO =Pentacam Oblique, CWI = clearwater index, CF = calculated factor, LRF= linear regression function, PS 1,4 = Python script with refraction factor 1,4) (own illustration)

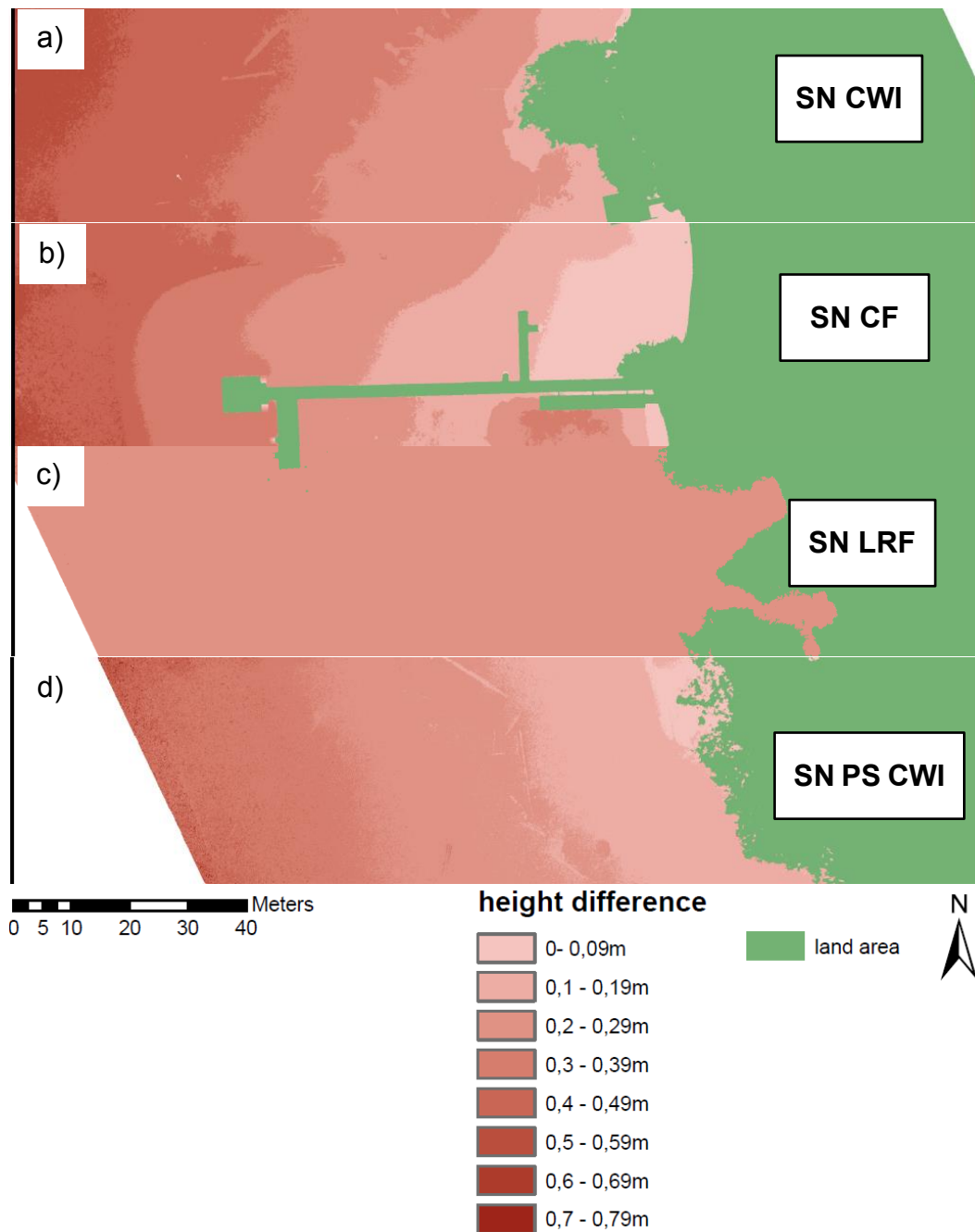


Figure 32: Sections of: a) SN clear water index corrected – SN uncorrected, b) SN factor corrected – SN uncorrected c) SN regression function corrected – SN uncorrected, d) SN iterative Python script corrected - SN uncorrected (SN= Sony Nadir, CWI = clearwater index, CF = calculated factor, LRF= linear regression function, PS CWI= Python script with clearwater index) (own illustration)

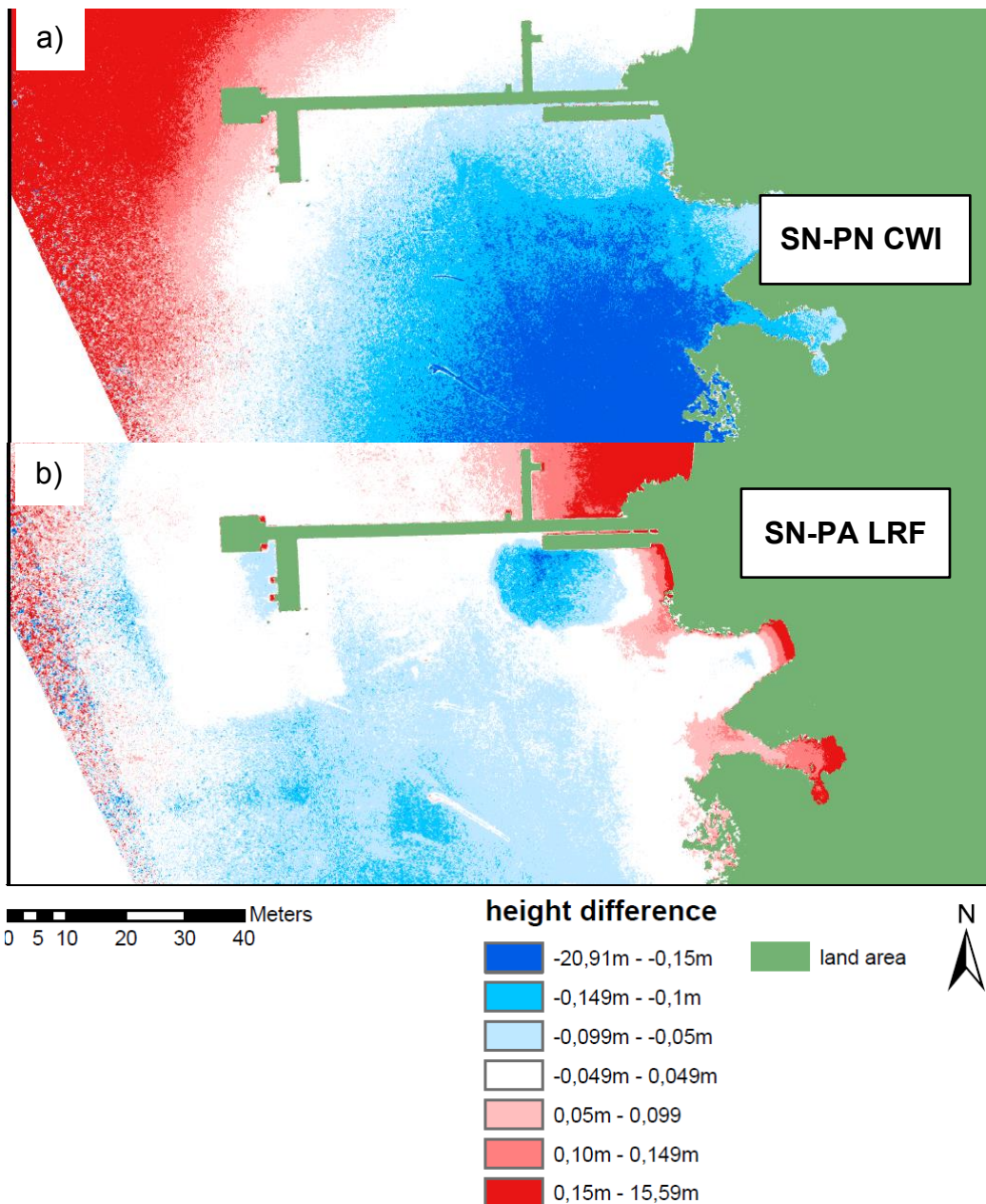


Figure 33: Sections of sensor comparison for different refraction approaches: a) Sony Nadir DSM minus Pentacam Nadir both corrected via clearwater index, b) Sony Nadir DSM minus Pentacam All both corrected via linear regression function derived from underwater reference points (SN= Sony Nadir, PA= Pentacam All, CWI = clearwater index, LRF= linear regression function) (own illustration)

The sensor comparison for each refraction approach shows a concentric height difference starting from the middle of the test area and spreading out to the side. Only in the dataset corrected with the linear regression function this pattern is not as distinctive.

The hole maps for all comparisons can be seen in Appendix D: Comparison of SfM DSM refraction corrected and uncorrected (Figure 46-Figure 52) and Appendix E: SfM DSM refraction corrected sensor comparison (Figure 55 - Figure 58).

## 6.5. Lidar data comparison

Between the SfM derived DSM's and the Lidar DSM and DOM a height difference of roughly 1,3m could be observed. Therefore, the same gap between the DGNS points and the Lidar data was found. Here only three points differ from the 1,3m height gap. One of the points was measured at the edge of the jetty, one was measured on a new paved area at the lakeside and the third at the helicopter landing site. The difference at the edge of the jetty can be explained by the low resolution (1m/pixel) of the Lidar data. Since between the capturing date of the two datasets are eight years, it is likely that changes in the terrain caused different height measurements at the other two points (Table 15).

Table 15: Height differences at the DGNS measured points on land with possible explanations of height deviation

Lidar DSM z value	DGNS z value	z_dif	points that deviate from the ≈1.3m height difference
930,032m	931,329m	1,296m	
930,184m	931,350m	1,166m	at the edge of the jetty
930,054m	931,340m	1,286m	
929,870m	931,173m	1,303m	
930,120m	931,411m	1,291m	
929,571m	931,369m	1,799m	new paved area
929,553m	930,863m	1,310m	
929,660m	930,964m	1,303m	
930,121m	931,424m	1,304m	
929,365m	930,704m	1,339m	
928,955m	930,700m	1,745m	helicopter landing site
929,979m	931,376m	1,397m	
929,696m	931,026m	1,330m	

A second conducted DGNSS measurement approach shows the same height difference. The overall error that causes this height difference could not be found and needs further investigation.

To make the lidar data better comparable the height values of the DEM were raised by 1.3m. Then the factor corrected SN and PA dataset were subtracted from the lidar DEM (Figure 34). Both complete maps can be found in Appendix F: Comparison, SfM data with Lidar data (Figure 59 - Figure 60).

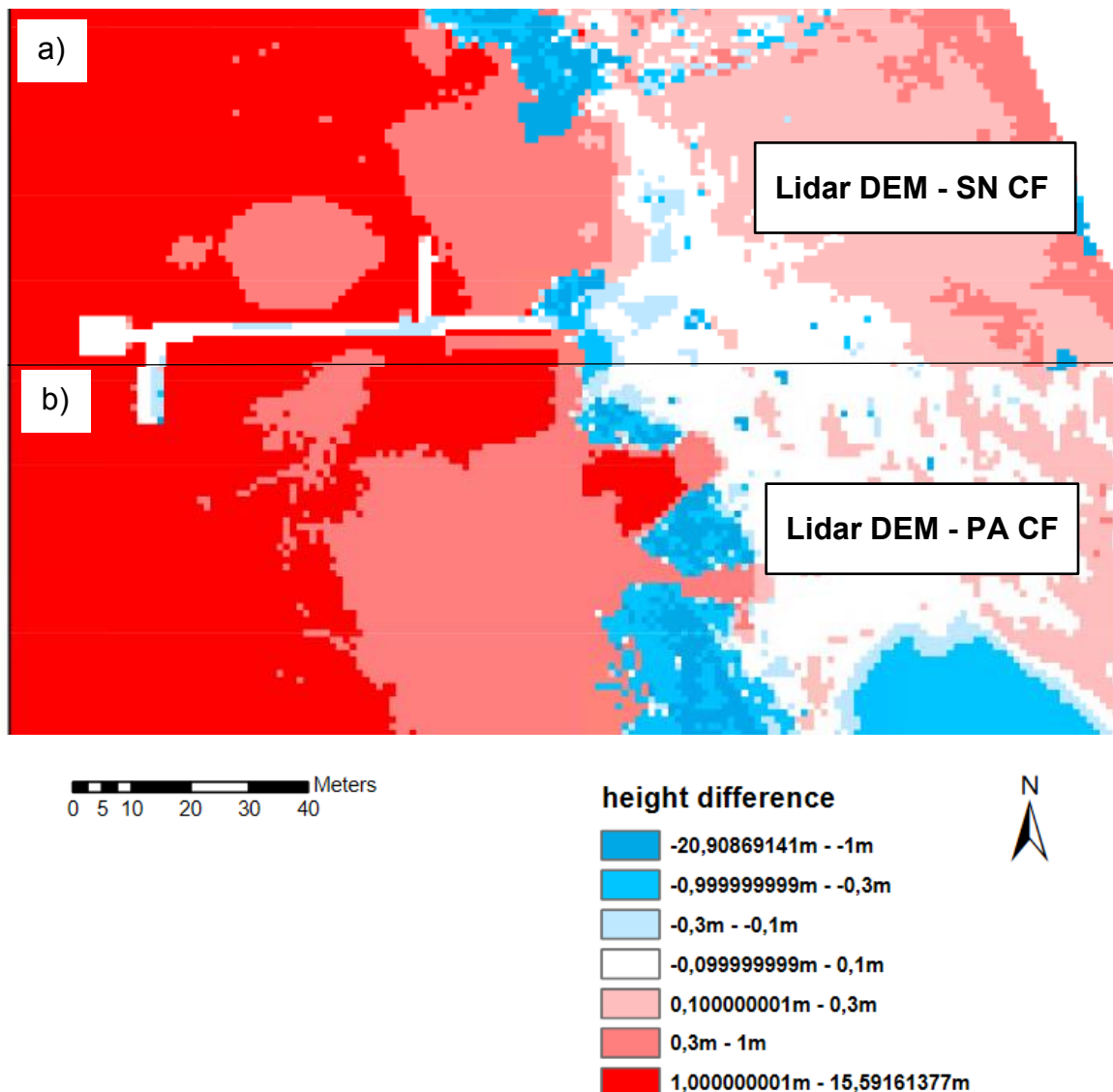


Figure 34: Lidar DEM height offset corrected(1,3m) minus a) SfM Sony Nadir derived factor corrected DSM b) SfM Pentacam all derived factor corrected DSM (SN= Sony Nadir, PA= Pentacam All, CF = calculated factor) (own illustration)

## **7. Discussion**

In the following chapter the finding of this theses will be used to answer the research question and giving additional insights about the work.

### **7.1. Refraction influence on our UAS image capturing setup**

Both, the theoretical calculations of the impact of the refraction with different view angles as well as within a single image and the practical comparison of the SfM data with validation points shows that the influence of the refraction of light have to be considered for UAS based bathymetric surveys. The theoretical calculation indicates a reduced water depth by the factor 1,337 at nadir direction going up to a factor of 1,66 at 48° off-nadir view. From the validation points and uncorrected data sets (SN, PA, PN, PO) calculated mean error of water depth lies between 25cm and 31cm.

It also shows that using oblique views has an impact on the estimated water depth. Since the refraction increases the more the view deviate from the nadir angle also the estimated water depth is shallower. This increase in refraction also leads to greater differences within a single image in oblique view than within images taken close to nadir direction.

### **7.2. Field data acquisition**

During the field experiment, enough aerial images for both camera setups could be captured for the SfM processing step. The weather conditions with no direct sunlight on the plane water surface allowed capturing aerial pictures without unwanted additional distortions.

The bigger sensor in the Sony Alpha 7RIII can capture more light than the Sony ILCE-QX1 sensors used in the Pentacam. This results in shorter exposure times and a sharper image. After looking in the detailed image information, it also turned out that the Sony Alpha 7RIII had a fixed exposure time of 1/250 second while the Pentacam was set to a fixed ISO of 100 and a variable exposure time. The possibility of syncing the flight with the camera trigger and therefore stop on the flight track when a photo is taken and the use of a 3-axis gimbal for better camera stabilization is in favor of the better image quality of the Sony alpha 7RII.

An additional disadvantage of the Pentacam was that the flight was conducted after the Sony Alpha 7RIII. This circumstance results in an overall darker scene since the field test was performed in the afternoon. As a result, some images captured with the Pentacam show a slight motion blur and the overall image quality is lower than from the Sony Alpha 7RIII.

For referencing, calibration and validation purposes the coordinates of several points in the project area were measured. The distribution of the on-land reference point was in a T-shape to avoid tilting of the point cloud. For this purpose, the jetty was important to have also land reference point at the water area. The funnel in the prepared metal plates made the aiming process underwater easy and accurate. This was especially important since they were measured from a canoe. Due to the cold weather conditions below 0°C, the number of additional underwater validation points that could be measured by foot was limited. Also, in some parts, squashy lake bottom had to be put into consideration to avoid the potential of additional errors. Therefore, the metal plates were essential, especially in the deeper areas where a layer of mud could be observed. In the shallow area near the jetty, almost no mud layer existed. In this area, the additional validation points were collected without using the metal plates.

### **7.3. Data preparation**

Especially for the Pentacam a preselection of the pictures was necessary since it was triggered. This trigger was started before the take-off and stopped after the UAV has landed, causing additional foto material, which was not needed for the SfM process. Also, photos lacking in sharpness were not used for the further SfM process. This adds up in more preprocessing work and can be a disadvantage for this capturing setup, especially for bigger data sets.

### **7.4. SfM Data processing and refraction correction**

This step was started with two datasets containing all the preselected images of the two camera systems. After the referencing step, the project with the images of the

Pentacam was split into three different projects with a different image selection. This step ensures to have the exact same projection for all three data sets.

One main difference between the different refraction correction approaches investigated in this master thesis was, that additional field reference data is required for some correction methods. This results in extra work in the field as well as in the refraction correction process. On the other hand, the retrieved results showed that this additional reference data could improve the refraction correction outcome's accuracy and precision. Especially if images are taken in off-nadir views, this step can be necessary. The refraction correction with the clear water index and the iterative refraction correction via Python script both have a lower accuracy for the data sets with oblique views. After further investigations of the Python script outcome, a combined approach with the theoretically calculated refraction correction factors was conducted. Instead of the clear water index the script was fed with the refraction factor at exact 25° off-nadir view and the Pentacam oblique data set. The result had a mean error of 0,5mm and a standard deviation of 29mm. This leads to the assumption that combined refraction correction method when using only oblique images with the same capturing angle is the most suitable for multi-view photogrammetry. If different view angles were used both correction methods using reference data delivered almost identical good results with a mean error between 0,9mm and 0,94mm and a standard deviation of 22,5mm. This makes them the most suitable for multi-view photogrammetry with different view angles.

### **7.5. Benefit of the two different camera setups.**

Using a camera system connected to the UAS and remotely controllable allows only to capture those images needed for the later SfM processing step. Skipping the image selection step for the Sony Alpha 7RIII accelerates the preprocessing effort compared to the Pentacam. The better image quality from the Sony Alpha 7RIII also made the referencing step accurate since the ground control plates were sharper and more detailed. The Sony Alpha 7RIII showed overall a better accuracy while the Pentacam had an overall better precision.

In spite of the lower image quality the SfM performance of the Pentacam could compete with the better Sony Alpha 7R III camera or even deliver more accurate and precise results.

The additional views from the Pentacam provide additional information and a larger number of images with which a higher point density can be achieved. In the context of shallow water bathymetry this difference in information can lead to a better result.

Comparing the two data sets a concentric height difference starting from the middle of the test area and spreading out to the side can be observed. Since further accurate data for comparing is not available further investigation is necessary to find out which dataset leads to this height differences. From the subtraction of the lidar data only an assumption can be made. On the resulting images a trend towards the SN data set can be seen. The results show also differences in a similar pattern, but these errors can be also caused by less images at the edge of the investigated area.

## 8. Conclusion and Further Work

The results show that the theoretically calculated values do not match precisely with the calculated refraction factor derived from the underwater reference points. Using these values for refraction correction only makes sense when a DSM-based correction should be applied on the SfM data set with images in oblique views. But further research has to be done, especially if images from different view angles are combined.

The combined approach of a precalculated refraction factor from the field experiment parameter and the iterative refraction correction delivered a promising result but needs further investigations since the script should take the camera view angle already in consideration and should not depend on special inputs for off-nadir data. If this can be replicated on another test site, an improvement of the script might be possible.

The limited number of reference and validation points and missing points in deeper water areas do not allow to make statements referring to the accuracy and precision at greater water depths.

Also, it will be necessary to test this approach in greater water depths to investigate its limits.

The calculated results also raise the question if the oblique view angle of our multisensor approach can be optimized. Especially the two sensors in vertical direction capture a more significant proportion of light beams with a much greater angle than the recommended  $35^\circ$ .

The concentric height difference between the two datasets indicates that maybe additional settings during the SfM process are necessary to provide an accurate result. Since the results from this work cannot really show which camera system is causing this issue, further investigations on different test sites with both camera setups in parallel are necessary to find the details causing these results.

Representing a new camera setup, the UAV image acquisition with the Pentacam is more time-consuming in the SfM preprocessing. With further optimizations during the image capturing process, this extra work can be reduced to the same amount as for the Sony Alpha 7RIII.

The recommended depth filtering in the Python script did not bring the expected improvement. The accuracy was even lower than without this option and the precision only increases slightly.

## References

Agrafiotis, P.; Georgopoulos, A. (2015): CAMERA CONSTANT IN THE CASE OF TWO MEDIA PHOTOGRAMMETRY. In *Int. Arch. Photogramm. Remote Sens. Spatial Inf. Sci.* XL-5/W5, pp. 1–6. DOI: 10.5194/isprsarchives-XL-5-W5-1-2015.

Agrafiotis, P.; Skarlatos, D.; Georgopoulos, A.; Karantzalos, K. (2019): SHALLOW WATER BATHYMETRY MAPPING FROM UAV IMAGERY BASED ON MACHINE LEARNING. In *Int. Arch. Photogramm. Remote Sens. Spatial Inf. Sci.* XLII-2/W10, pp. 9–16. DOI: 10.5194/isprs-archives-XLII-2-W10-9-2019.

Albertz, J.; Wiggenhagen, M. (2009): Taschenbuch zur Photogrammetrie und Fernerkundung. Guide for photogrammetry and remote sensing. 5., völlig neu bearbeitete und erweiterte Auflage. Heidelberg: Wichmann.

Alvarez, L.; Moreno, H.; Segales, A.; Pham, T.; Pillar-Little, E.; Chilson, P. (2018): Merging Unmanned Aerial Systems (UAS) Imagery and Echo Soundings with an Adaptive Sampling Technique for Bathymetric Surveys. In *Remote Sensing* 10 (9), p. 1362. DOI: 10.3390/rs10091362.

Amt der Kärntner Landesregierung (2020): bathymetric map. Available online at [kis.ktn.gv.at](http://kis.ktn.gv.at), checked on 2020.

Austro Control (2020): Operation of Drones in Austria. Available online at

[https://www.austrocontrol.at/en/aviation\\_agency/licenses\\_\\_permissions/flight\\_permissions/rpas](https://www.austrocontrol.at/en/aviation_agency/licenses__permissions/flight_permissions/rpas), checked on 4/29/2020.

Bailly, J.; Le Coarer, Y.; Languille, P.; Stigermark, C.-J.; Allouis, T. (2010): Geostatistical estimations of bathymetric LiDAR errors on rivers. In *Earth Surface Processes and Landforms* 35 (10), pp. 1199–1210. DOI: 10.1002/esp.1991.

Bangen, S. G.; Wheaton, J. M.; Bouwes, N.; Bouwes, B.; Jordan, C. (2014): A methodological intercomparison of topographic survey techniques for characterizing wadeable streams and rivers. In *Geomorphology* 206, pp. 343–361. DOI: 10.1016/j.geomorph.2013.10.010.

Butler, J. B.; Lane, S. N.; Chandler, J. H.; Porfiri, E. (2002): THROUGH-WATER CLOSE RANGE DIGITAL PHOTOGRAMMETRY IN FLUME AND FIELD ENVIRONMENTS. In *Photogrammetric Record* 17, pp. 419–439.

Carbonneau, P. E.; Lane, S. N.; Bergeron, N. (2006): Feature based image processing methods applied to bathymetric measurements from airborne remote sensing in fluvial environments. In *Earth Surface Processes and Landforms* 31 (11), pp. 1413–1423. DOI: 10.1002/esp.1341.

Chen, S.; Xue, C.; Zhang, T.; Hu, L.; Chen, G.; Tang, J. (2019): Analysis of the Optimal Wavelength for Oceanographic Lidar at the Global Scale Based on the Inherent Optical Properties of Water. In *Remote Sensing* 11 (22), p. 2705. DOI: 10.3390/rs11222705.

Church, M.; Roy, A. G.; Biron, P. M.; Ashmore, P.; Bergeron, N.; Buffin-Belanger, T.; Rennie, C. (2012): Gravel-bed rivers. Processes, tools, environments. Chichester: John Wiley & Sons.

Conner, J. T.; Tonina, D. (2014): Effect of cross-section interpolated bathymetry on 2D hydrodynamic model results in a large river. In *Earth Surf. Process. Landforms* 39 (4), pp. 463–475. DOI: 10.1002/esp.3458.

Dietrich, J. T. (2017a): Bathymetric Structure-from-Motion: extracting shallow stream bathymetry from multi-view stereo photogrammetry. In *Earth Surf. Process. Landforms* 42 (2), pp. 355–364. DOI: 10.1002/esp.4060.

Dietrich, J. T. (2017b): pyBathySfM. A Python script for performing refraction correction on Structure from Motion datasets (2). Available online at <https://geojames.github.io/pyBathySfM/>, checked on 1/8/2020.

Dietrich, J. T. (2019): pyBathySfM. File number v4.0. Python Skript.

Dodds, Walter K. (2002): Freshwater ecology. Concepts and environmental applications / Walter K. Dodds. San Diego, Calif., London: Academic.

EU (2000): Water Framework Directive 2000/60/EC. In *Official Journal of the European Communities* 327.

Feurer, D.; Bailly, J.-S.; Puech, C.; Le Coarer, Y.; Viau, A. A. (2008): Very-high-resolution mapping of river-immersed topography by remote sensing. In *Progress in Physical Geography: Earth and Environment* 32 (4), pp. 403–419. DOI: 10.1177/0309133308096030.

Grenzdörffer, G. J.; Naumann, M. (2016): INVESTIGATIONS ON THE POSSIBILITIES OF MONITORING COASTAL CHANGES INCLUDING SHALLOW UNDER WATER AREAS WITH UAS PHOTO BATHMETRY. In *Int. Arch. Photogramm. Remote Sens. Spatial Inf.*

*Sci.* XLI-B1, pp. 843–850. DOI: 10.5194/isprsarchives-XLI-B1-843-2016.

Harvey, A. H.; Gallagher, J. S.; Sengers, J. M. H. L. (1998): Revised Formulation for the Refractive Index of Water and Steam as a Function of Wavelength, Temperature and Density. In *Journal of Physical and Chemical Reference Data* 27 (4), pp. 761–774. DOI: 10.1063/1.556029.

Hauer, C.; Mandlbürger, G.; Habersack, H. (2009): Hydraulically related hydro-morphological units: description based on a new conceptual mesohabitat evaluation model (MEM) using LiDAR data as geometric input. In *River Res. Applic.* 25 (1), pp. 29–47. DOI: 10.1002/rra.1083.

Jocham, S.; Dobler, W.; Baran, R.; Aufleger, M.; Steinbacher, F. (2014): Einsatz hochauflösender Bathymetriedaten aus luftgestützter Vermessung in der Abfluss- und Habitatmodellierung. In *Österr Wasser- und Abfallw* 66 (5-6), pp. 206–213. DOI: 10.1007/s00506-014-0153-3.

Kasvi, E.; Salmela, J.; Lotsari, E.; Kumpula, T.; Lane, S. N. (2019): Comparison of remote sensing based approaches for mapping bathymetry of shallow, clear water rivers. In *Geomorphology* 333, pp. 180–197. DOI: 10.1016/j.geomorph.2019.02.017.

Kinzel, P. J.; Wright, C. W.; Nelson, J. M.; Burman, A. R. (2007): Evaluation of an Experimental LiDAR for Surveying a Shallow, Braided, Sand-Bedded River. In *Journal of Hydraulic Engineering* 133 (7), pp. 838–842. DOI: 10.1061/(asce)0733-9429(2007)133:7(838).

Klopper, F.; Hammerle, M.; Hofle, B. (2017): Assessing the Potential of a Low-Cost 3-D Sensor in Shallow-Water Bathymetry. In *IEEE Geosci. Remote Sensing Lett.* 14 (8), pp. 1388–1392. DOI: 10.1109/LGRS.2017.2713991.

Kongsberg (2020): Product datasheet. Available online at <https://www.kongsberg.com/maritime/products/mapping-systems/mapping-systems/multibeam-echo-sounders/>, updated on 1/27/2020, checked on 1/27/2020.

Lane, S. N.; Widdison, P. E.; Thomas, R. E.; Ashworth, P. J.; Best, J. L.; Lunt, I. A. et al. (2010): Quantification of braided river channel change using archival digital image analysis. In *Earth Surface Processes and Landforms* 35 (8), pp. 971–985. DOI: 10.1002/esp.2015.

Legleiter, C. J. (2012): MAPPING RIVER DEPTH FROM PUBLICLY AVAILABLE AERIAL IMAGES. In *River Research and Applications* 29 (6), pp. 760–780. DOI: 10.1002/rra.2560.

Legleiter, C. J. (2013): MAPPING RIVER DEPTH FROM PUBLICLY AVAILABLE AERIAL IMAGES. In *River Res. Applic.* 29 (6), pp. 760–780. DOI: 10.1002/rra.2560.

Lejot, J.; Delacourt, C.; Piégay, H.; Fournier, T.; Trémélo, M-L.; Allemand, P. (2007): Very high spatial resolution imagery for channel bathymetry and topography from an unmanned mapping controlled platform. In *Earth Surface Processes and Landforms* 32 (11), pp. 1705–1725. DOI: 10.1002/esp.1595.

Longley, P.; Goodchild, M. F.; Maguire, D. J.; Rhind, D. (2016): Geographic information science and systems. 4th edition (B&W). Hoboken, NJ: Wiley Custom Learning Solutions.

Luhmann, T. (2003): Nahbereichsphotogrammetrie. Grundlagen, Methoden und Anwendungen. 2., überarb. Aufl. Heidelberg: Wichmann.

Marks, K. M.; Smith, W. H. F. (2008): An uncertainty model for deep ocean single beam and multibeam echo sounder data. In *Mar Geophys Res* 29 (4), pp. 239–250. DOI: 10.1007/s11001-008-9060-y.

Paulus, G.; Anders, K.-H.; Erlacher, M.; Mayr, P.; Schneeberger, R. (2019): WÖRTHERSEE 3D – EMPIRISCHER VERGLEICH VON FLACHWASSERBATHYMETRIEDATEN. UAS PHOTOGRAMMETRIE VERSUS SINGLE BEAM ECHOLOTT. In *Publikationen der DGPF* Band 28.

Pinz, K. (2011): 10 Jahre Wasserrahmenrichtlinie: Sachstand zwischen Erwartung und Befürchtungen, Anspruch und Realität. In : WARNSIGNAL KLIMA: Genug Wasser für alle?, vol. 3.

PolarNick239 (2020): footprints\_to\_shapes. Version Oct 22, 2020: Github. Available online at <https://github.com/agisoft-llc/metashape-scripts>.

Riegl (2019): RIEGL\_VQ-840-G\_Preliminary-Datasheet\_2019-09-02.

Schiebener, P.; Straub, J.; Levelt Sengers, J. M. H.; Gallagher, J. S. (1990): Refractive index of water and steam as function of wavelength, temperature and density. In *Journal of Physical and Chemical Reference Data* 19 (3), pp. 677–717. DOI: 10.1063/1.555859.

Teledyne optech (2020): World`s first multispectral Lidar. A revolution in Lidar applications. Available online at <https://www.teledyneoptech.com/en/products/airborne-survey/titan/>, checked on 2/9/2020.

TEWINKEL, G. C. (1963): Water Depths from Aerial Photographs. In *Photogrammetric Engineering* Vol. XXIX, No. 6, pp. 1037–1042.

Westaway, R. M. (2001): Remote sensing of clear-water, shallow, gravel-bed rivers using digital photogrammetry. In *Photogrammetric Engineering and Remote Sensing* 67 (11), p. 1271.

Westaway, R. M.; Lane, S. N.; Hicks, D. M. (2003): Remote survey of large-scale braided, gravel-bed rivers using digital photogrammetry and image analysis. In *International Journal of Remote Sensing* 24 (4), pp. 795–815. DOI: 10.1080/01431160110113070.

Westoby, M. J.; Brasington, J.; Glasser, N. F.; Hambrey, M. J.; Reynolds, J. M. (2012): ‘Structure-from-Motion’ photogrammetry: A low-cost, effective tool for geoscience applications. In *Geomorphology* 179, pp. 300–314. DOI: 10.1016/j.geomorph.2012.08.021.

Winterbottom, S. J.; Gilvear, D. J. (1997): Quantification of channel bed morphology in gravel-bed rivers using airborne multispectral imagery and aerial photography. In *Regulated Rivers: Research & Management* 13 (6), pp. 489–499. DOI: 10.1002/(sici)1099-1646(199711/12)13:6<489::aid-rrr471>3.0.co;2-x.

Woodget, A. S.; Carbonneau, P. E.; Visser, F.; Maddock, I. P. (2015a): Quantifying submerged fluvial topography using hyperspatial resolution UAS imagery and structure from motion photogrammetry. In *Earth Surf. Process. Landforms* 40 (1), pp. 47–64.

Woodget, A. S.; Carbonneau, P. E.; Visser, F.; Maddock, I. P. (2015b): Quantifying submerged fluvial topography using hyperspatial resolution UAS imagery and structure from motion photogrammetry. In *Earth Surf. Process. Landforms* 40 (1), pp. 47–64. DOI: 10.1002/esp.3613.

Woodget, Amy S.; Dietrich, James T.; Wilson, Robin T. (2019): Quantifying Below-Water Fluvial Geomorphic Change: The Implications of Refraction Correction, Water Surface Elevations, and Spatially Variable Error. In *Remote Sensing* 11 (20), p. 2415. DOI: 10.3390/rs11202415.

Xu, G. (2010): *Sciences of geodesy*. Heidelberg, New York: Springer.

## Appendix A: Orthomosaic

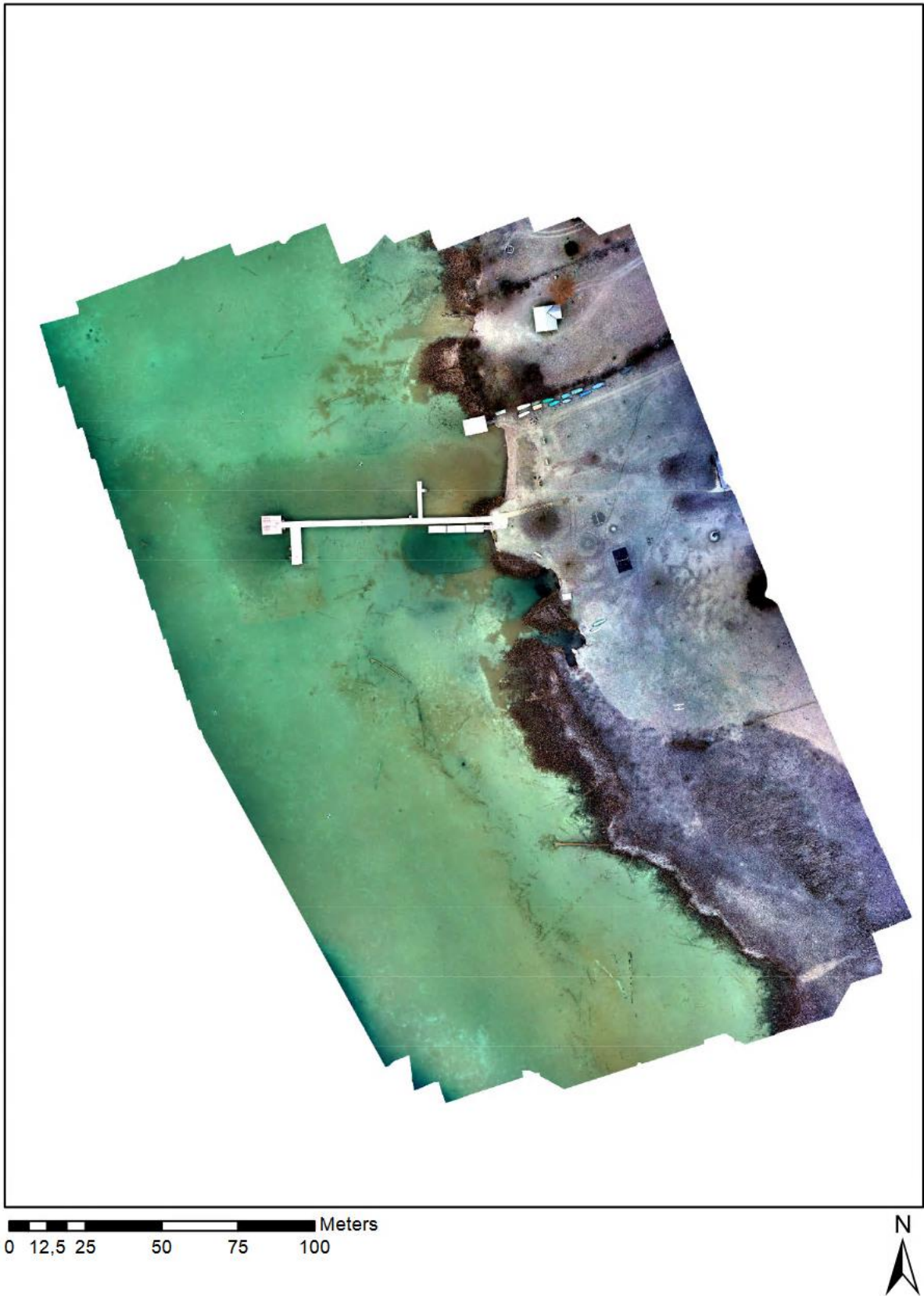
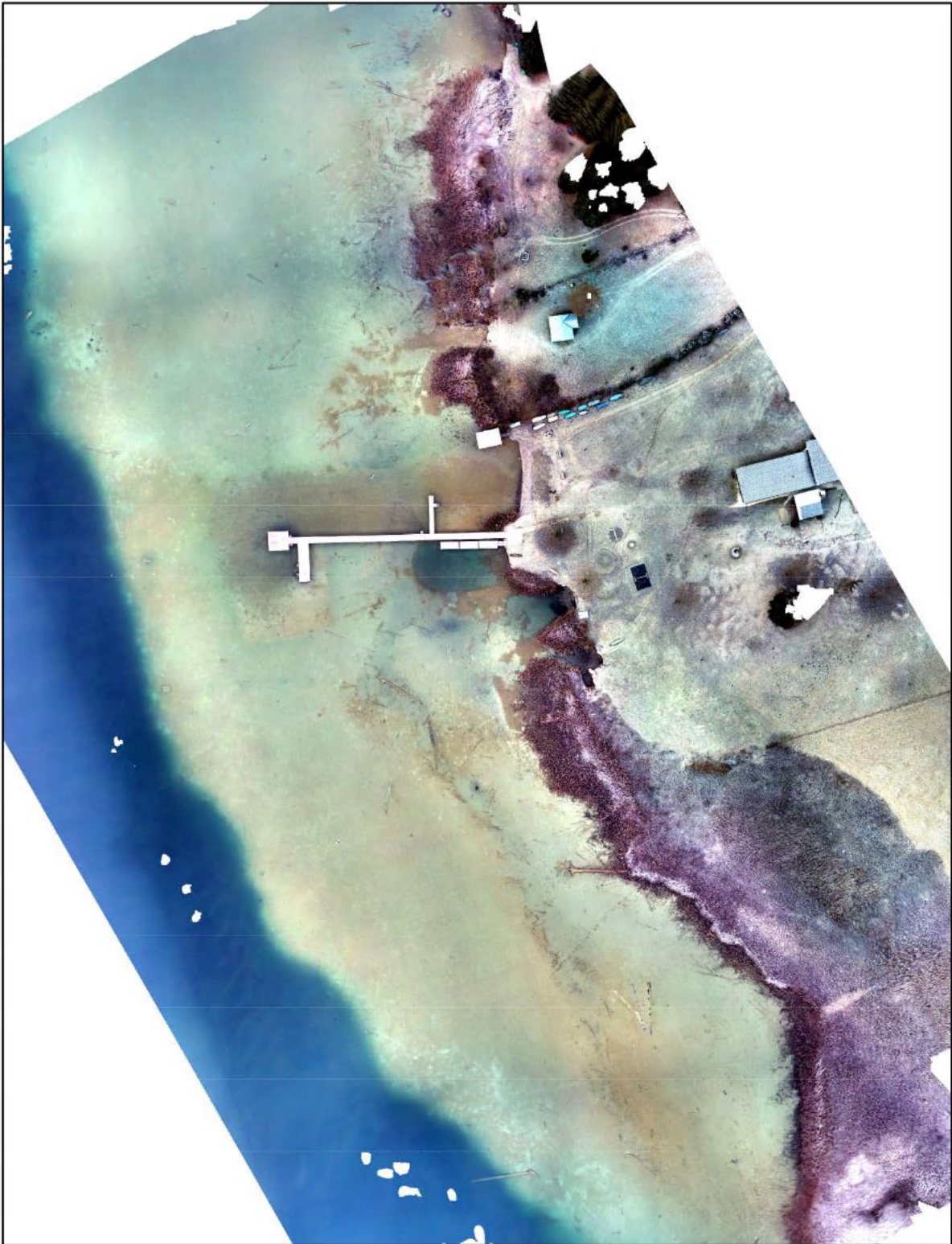


Figure 35: Sony nadir Orthomosaic (own Illustration)



0 12,5 25 50 75 100 Meters



Figure 36: Pentacam all images orthomosaic (own Illustration)

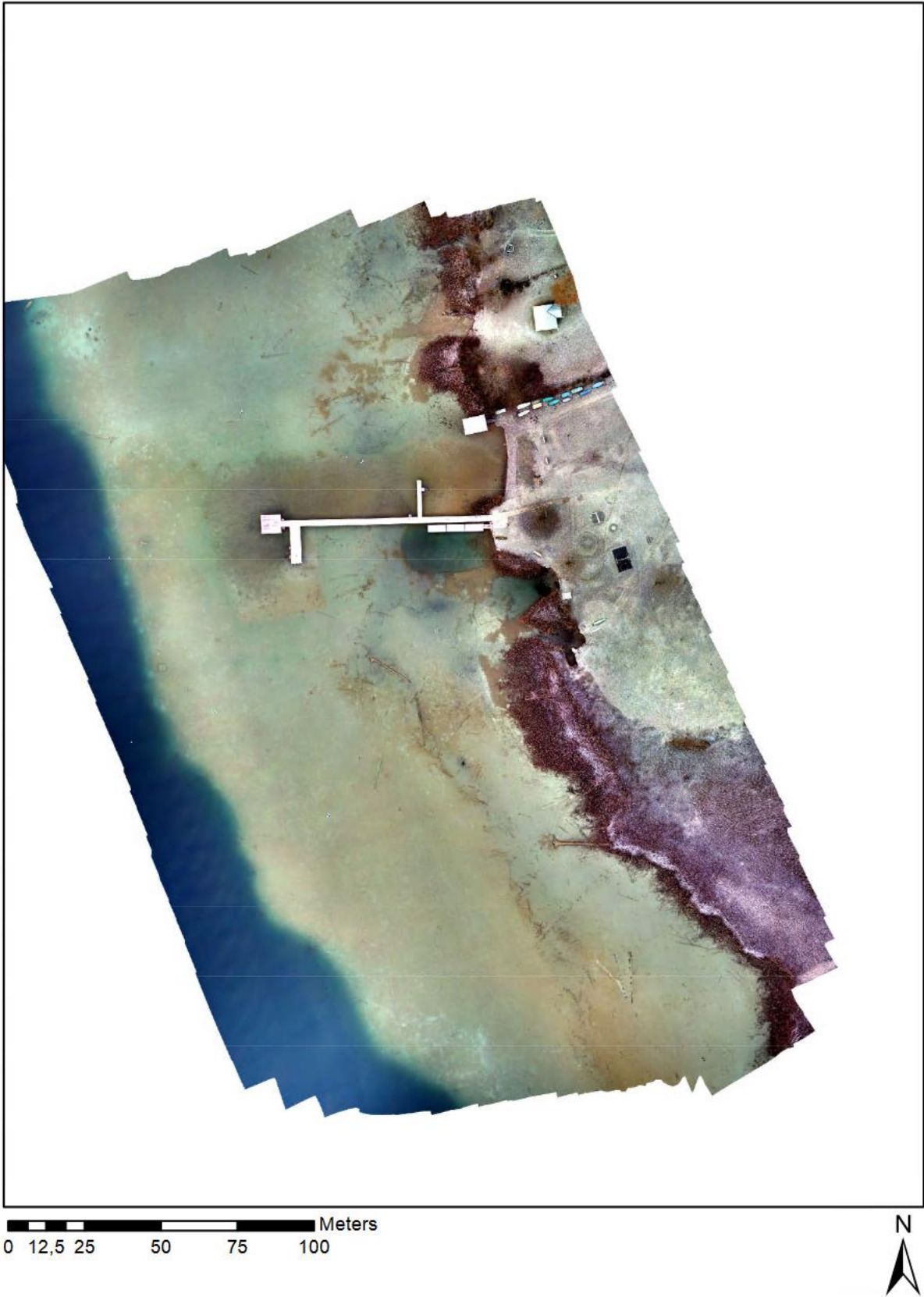


Figure 37: Pentacam nadir orthomosaic (own illustration)

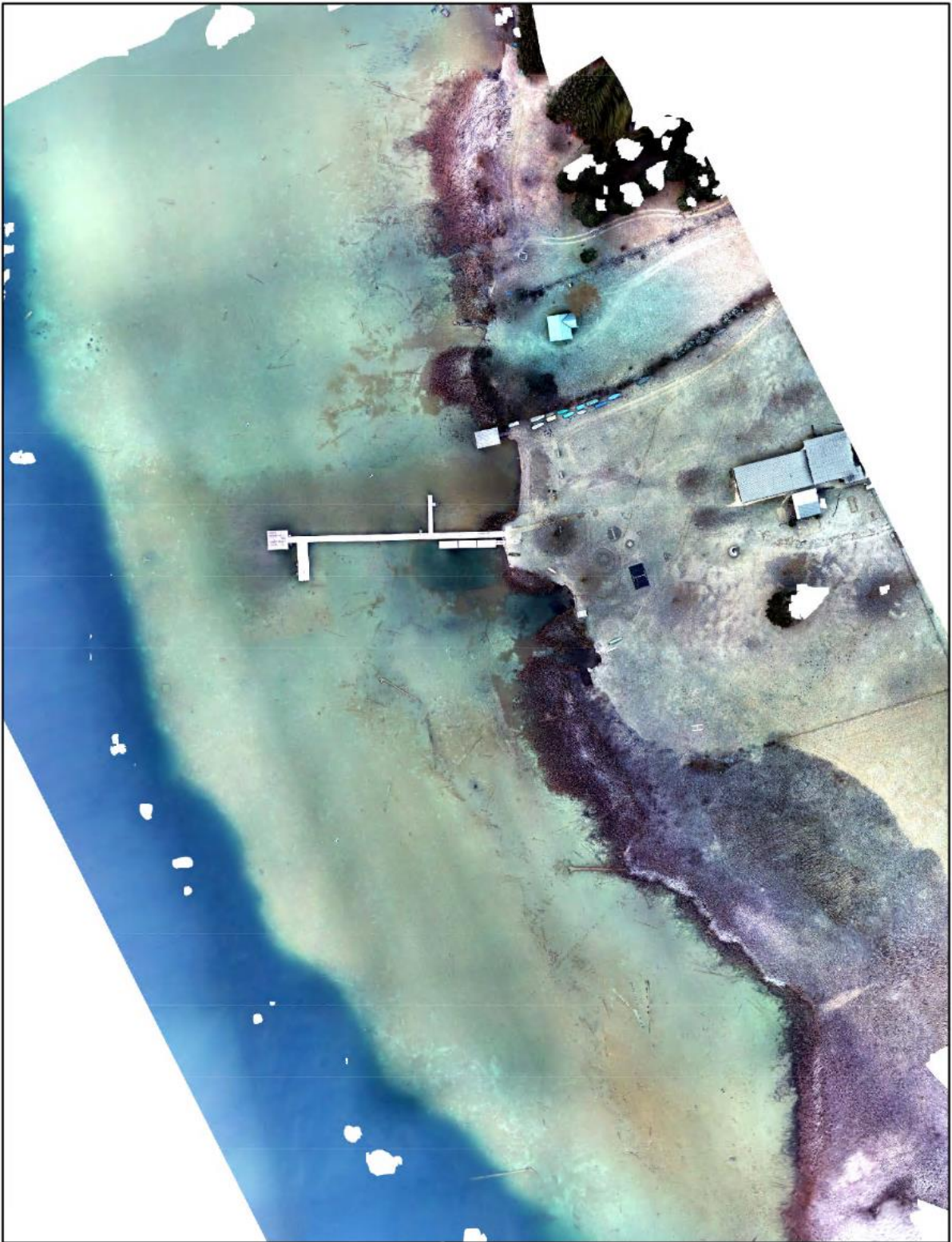
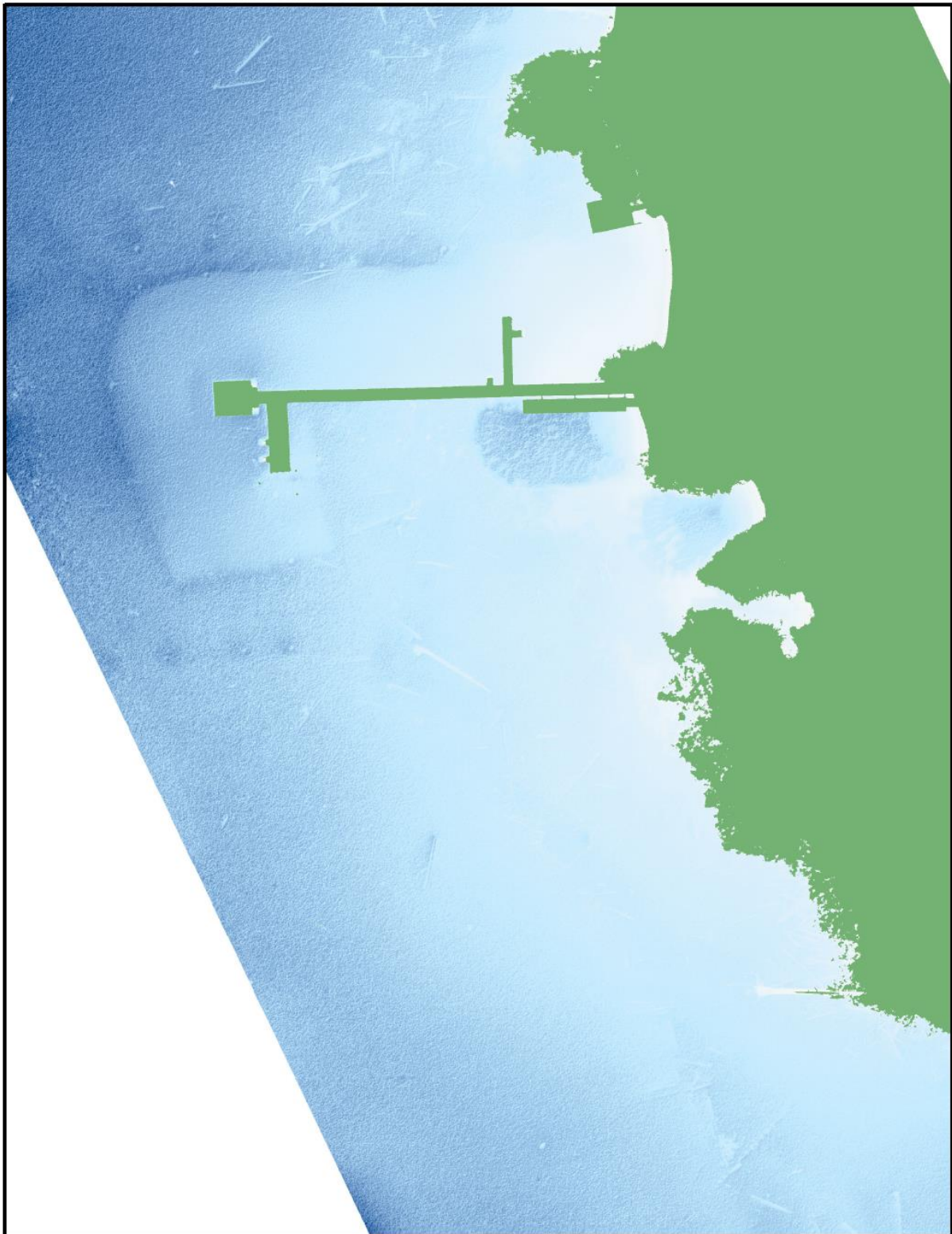


Figure 38: Pentacam Oblique Orthomosaic (own illustration)

## **Appendix B: SfM water depth DSM uncorrected**

Figure 39-Figure 42 shows the uncorrected SfM DSM's with the water depth information of all four data sets. To visualize more details the effect hillshade was activated in ArcMap.



0 5 10 20 30 40 Meters

height difference

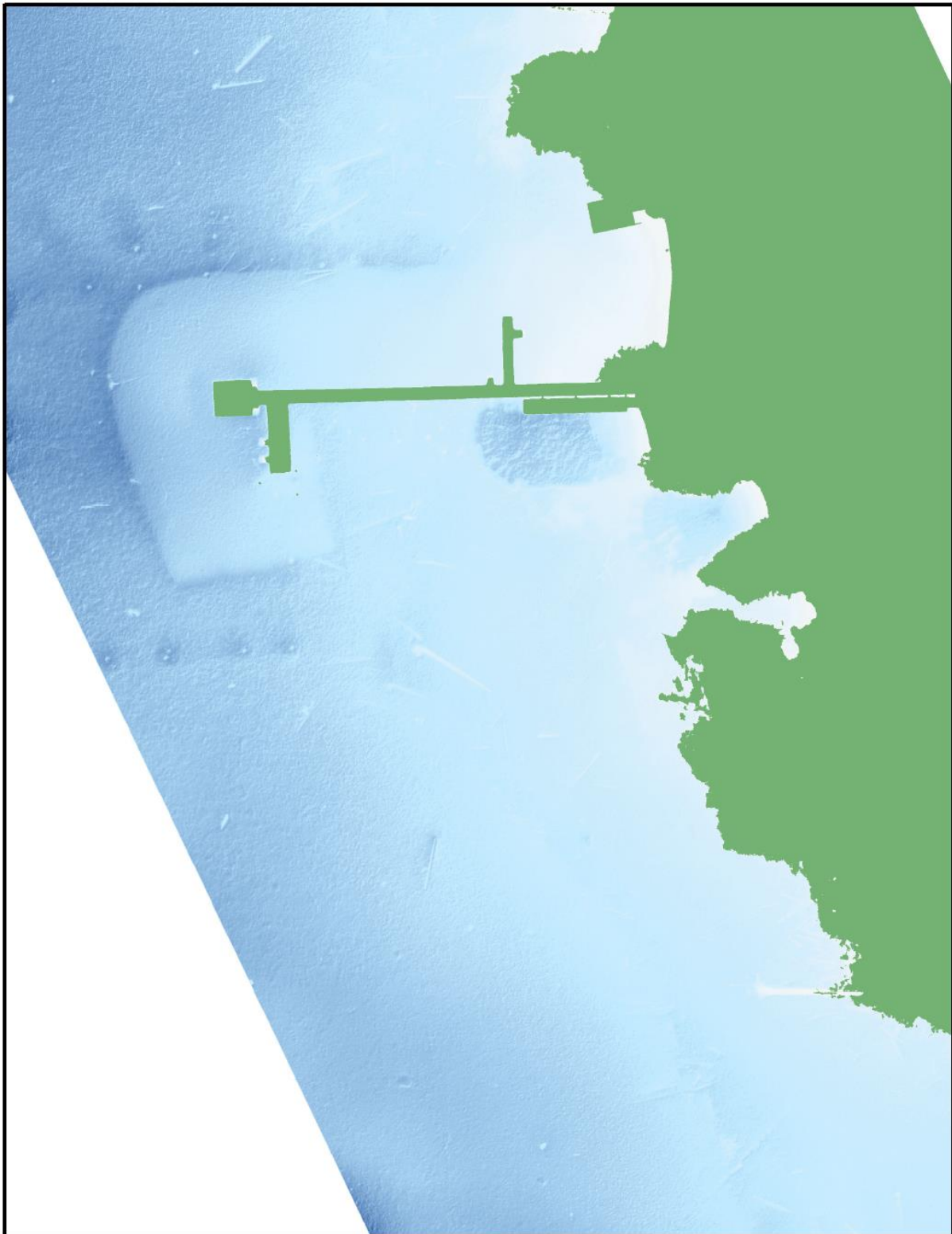


2,5m  
1m  
0m

land area



Figure 39: Water depth Sony Nadir DSM uncorrected (own illustration with hillshade effect)



0 5 10 20 30 40 Meters

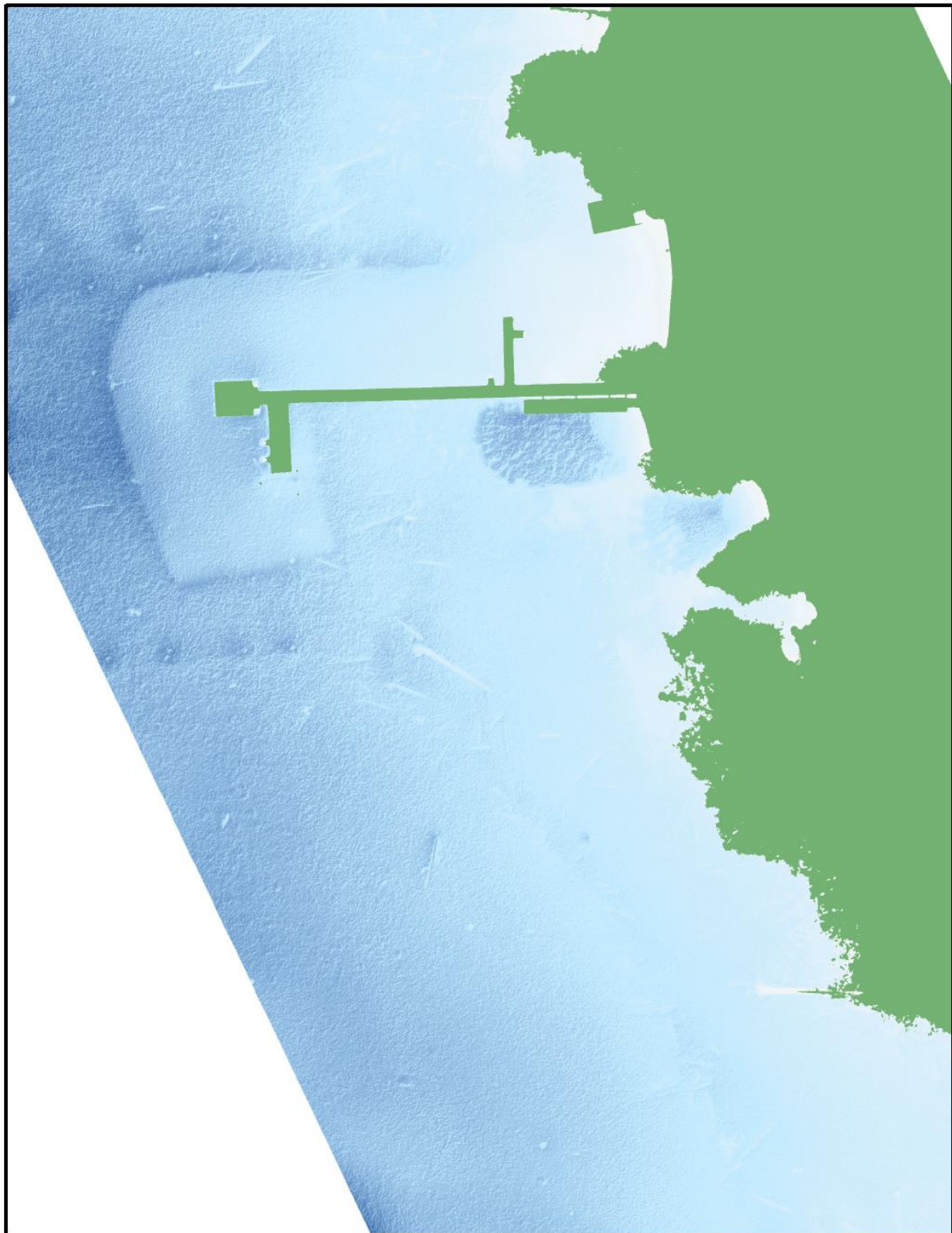
height difference



land area



Figure 40: Water depth Pentacam All DSM uncorrected (own illustration with hillshade effect)



0 5 10 20 30 40 Meters

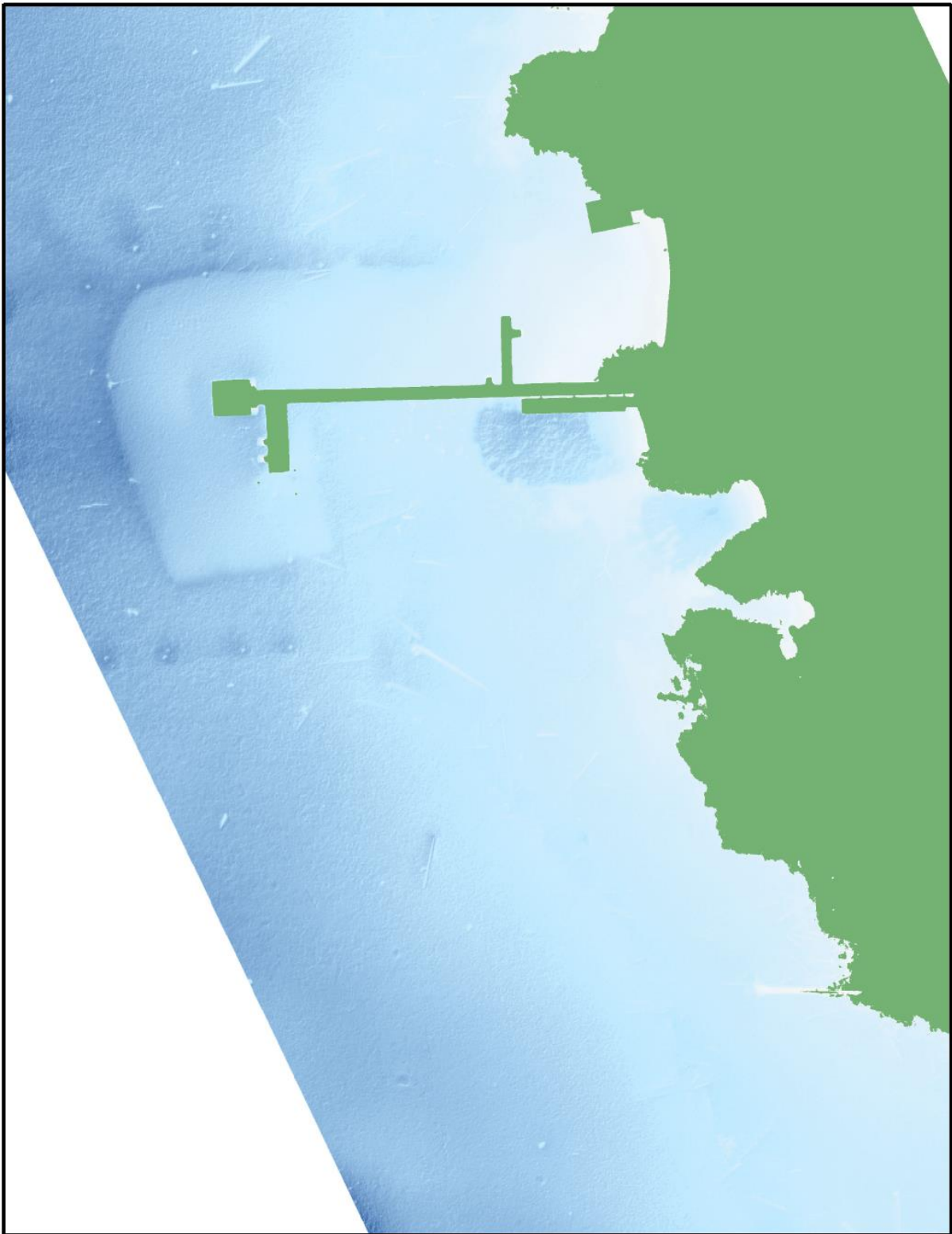
**height difference**



land area



Figure 41: Water depth Pentacam Nadir DSM uncorrected (own illustration with hillshade effect)



0 5 10 20 30 40 Meters

height difference



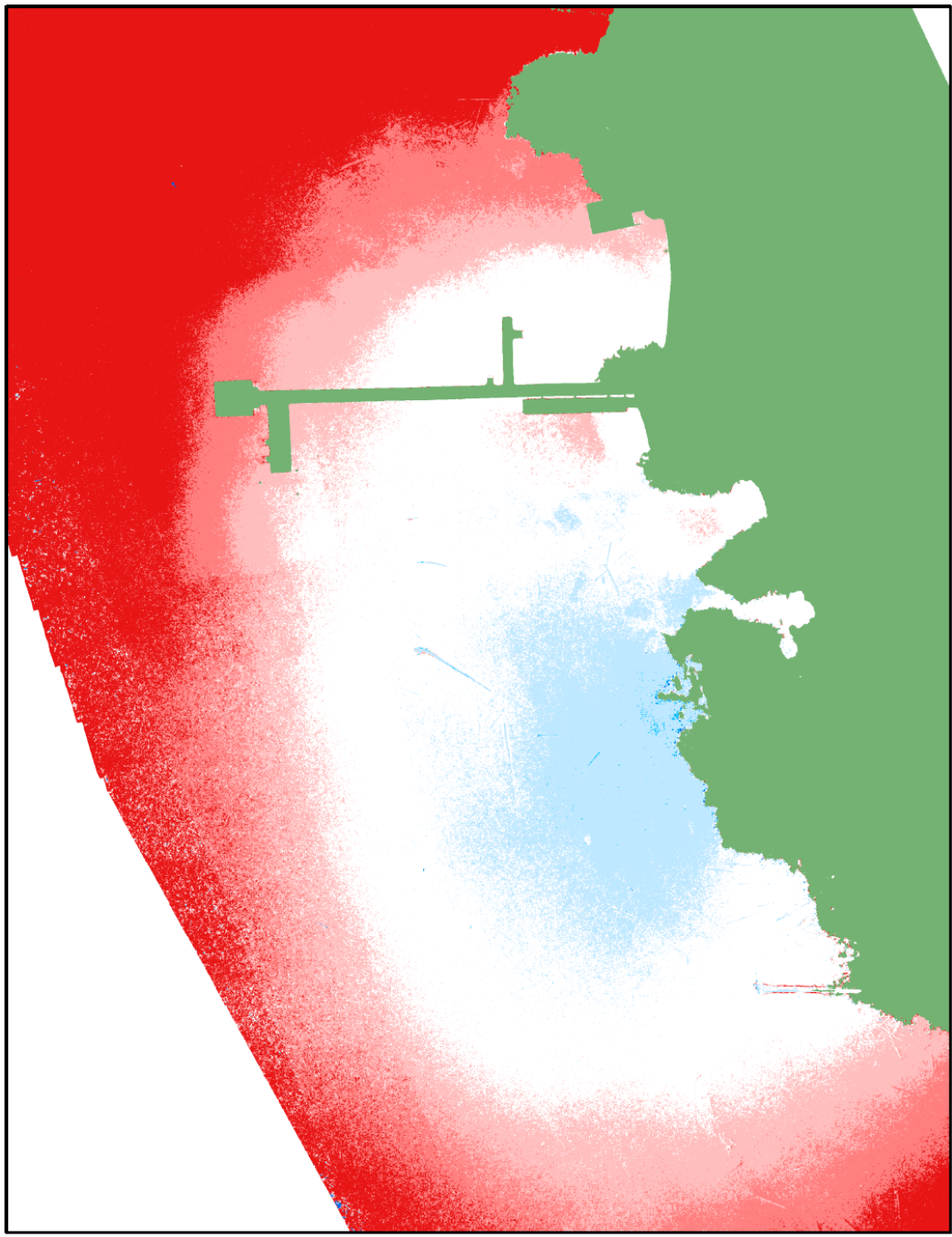
land area



Figure 42: Water depth Pentacam Oblique DSM uncorrected (own illustration with hillshade effect)

## **Appendix C: SfM DSM uncorrected comparison**

Comparing (Figure 43-Figure 45) the two camera setups highlights that slightly higher elevation values were captured with the Sony Alpha 7R III at the middle of the test area than with the Pentacam. This area of the test site is very shallow. The biggest difference could be observed between the two data sets consisting of Nadir images.



0 5 10 20 30 40 Meters

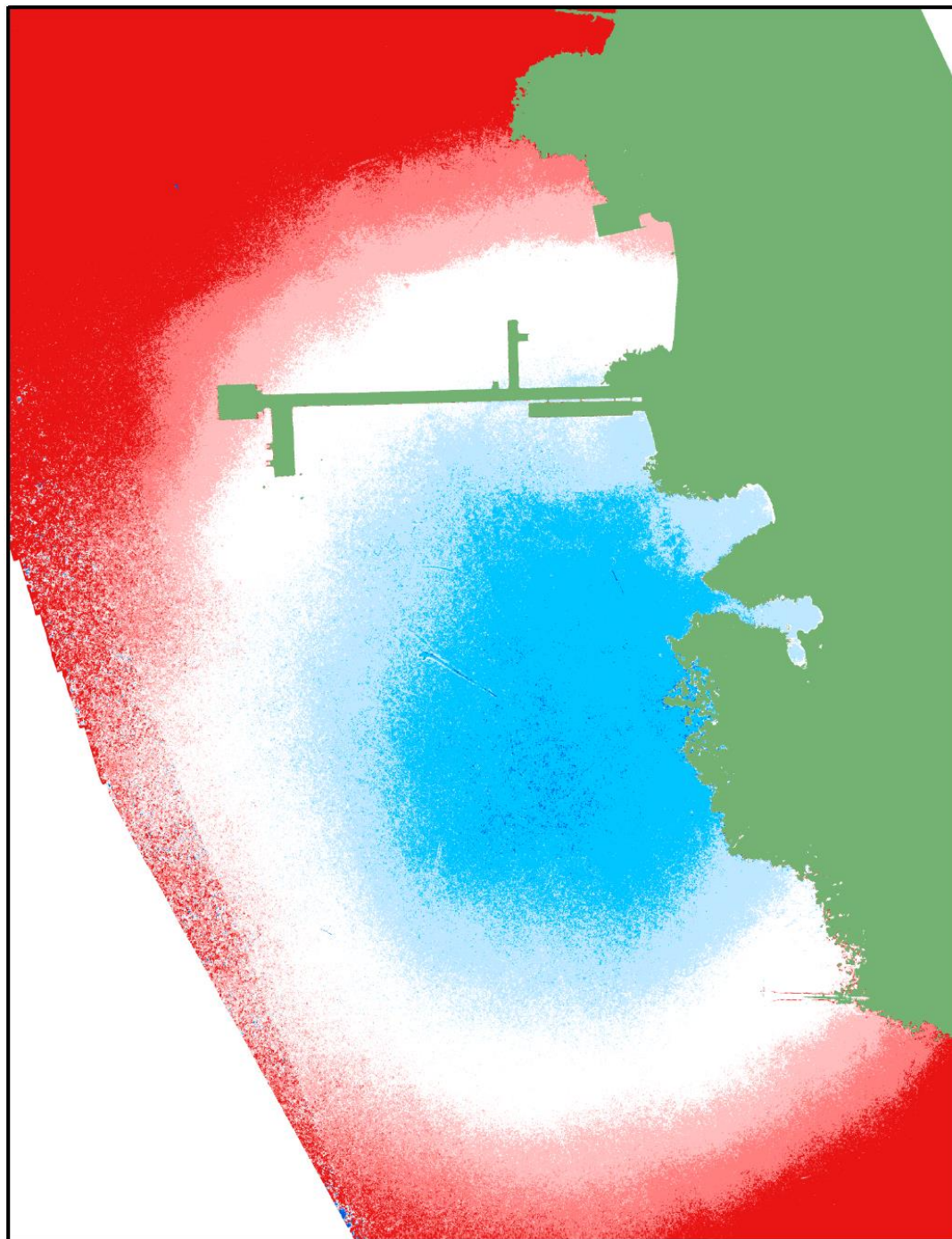
**height difference**

- 20,91m - -0,15m
- 0,149m - -0,1m
- 0,099m - -0,05m
- 0,049m - 0,049m
- 0,05m - 0,099
- 0,10m - 0,149m
- 0,15m - 15,59m

land area



Figure 43: Sony Nadir DSM minus Pentacam all DSM both uncorrected (own illustration)



0 5 10 20 30 40 Meters

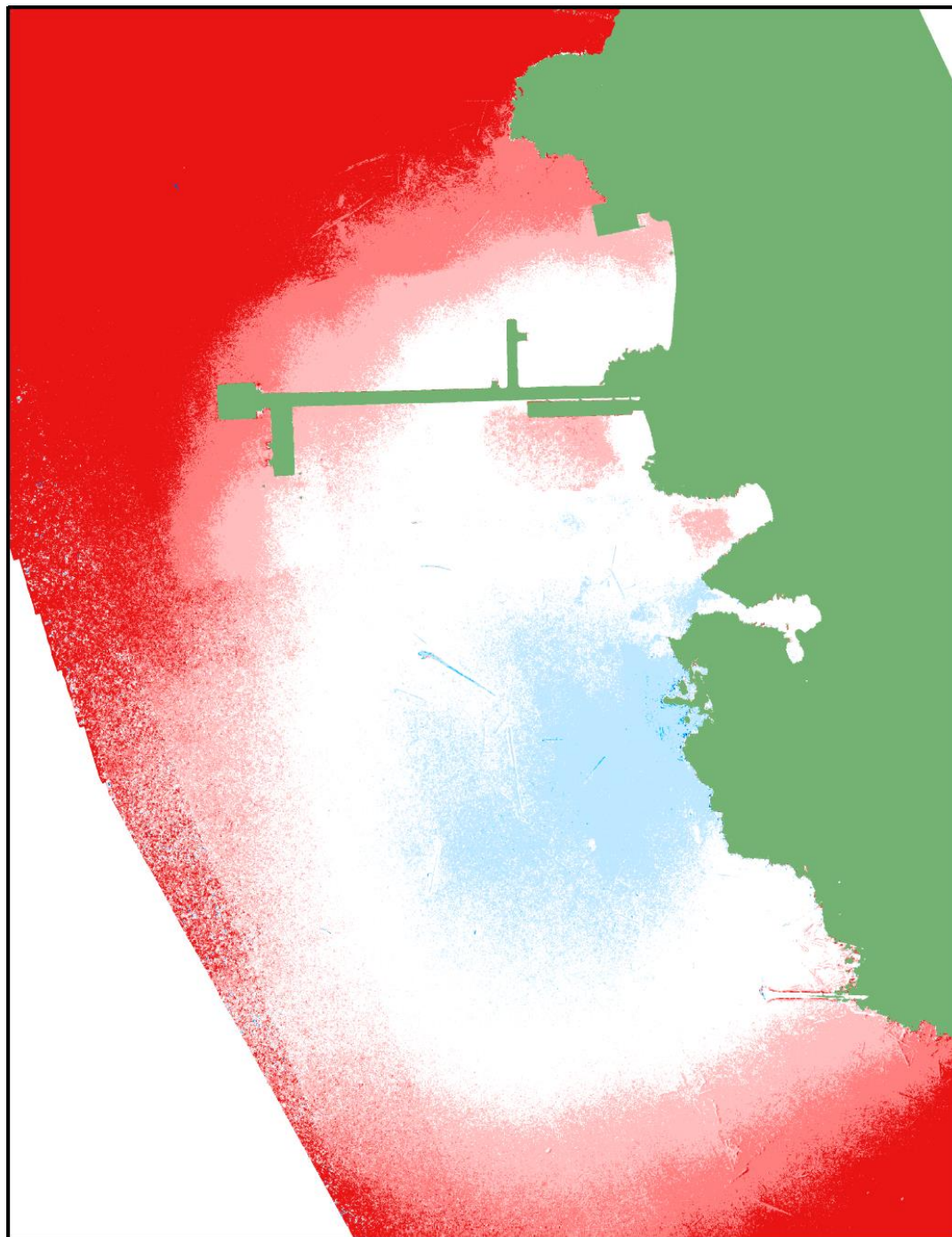
**height difference**

- 20,91m - -0,15m
- 0,149m - -0,1m
- 0,099m - -0,05m
- 0,049m - 0,049m
- 0,05m - 0,099
- 0,10m - 0,149m
- 0,15m - 15,59m

land area



Figure 44: Sony Nadir DSM minus Pentacam nadir DSM both uncorrected (own illustration)



0 5 10 20 30 40 Meters

**height difference**

- 20,91m - -0,15m
- 0,149m - -0,1m
- 0,099m - -0,05m
- 0,049m - 0,049m
- 0,05m - 0,099
- 0,10m - 0,149m
- 0,15m - 15,59m

land area



Figure 45: Sony Nadir DSM minus Pentacam oblique DSM both uncorrected (own illustration)

## **Appendix D: Comparison of SfM DSM refraction corrected and uncorrected**

Figure 46 - Figure 54 illustrates the water depth comparison between the refraction corrected SN DSM and the uncorrected SN DSM and the best performing Pentacam data set for each refraction correction approach and the uncorrected corresponding Pentacam DSM.



0 5 10 20 30 40 Meters

**height difference**

- 0- 0,09m
- 0,1 - 0,19m
- 0,2 - 0,29m
- 0,3 - 0,39m
- 0,4 - 0,49m
- 0,5 - 0,59m
- 0,6 - 0,69m
- 0,7 - 0,79m
- 0,8 - 0,9m

land area



Figure 46: Pentacam Nadir clear water index corrected DSM minus Pentacam Nadir uncorrected DSM (own illustration)



0 5 10 20 30 40 Meters

**height difference**

- 0 - 0,09m
- 0,1 - 0,19m
- 0,2 - 0,29m
- 0,3 - 0,39m
- 0,4 - 0,49m
- 0,5 - 0,59m
- 0,6 - 0,69m
- 0,7 - 0,79m
- 0,8 - 0,9m

land area



Figure 47: Pentacam All derived factor corrected DSM minus Pentacam All uncorrected DSM (own illustration)



0 5 10 20 30 40 Meters

**height difference**

- 0 - 0,09m
- 0,1 - 0,19m
- 0,2 - 0,29m
- 0,3 - 0,39m
- 0,4 - 0,49m
- 0,5 - 0,59m
- 0,6 - 0,69m
- 0,7 - 0,79m
- 0,8 - 0,9m

land area



Figure 48: Pentacam All linear regression function corrected DSM minus Pentacam All uncorrected DSM (own illustration)



Figure 49: Pentacam Oblique iterative Python script (index = 1,337) corrected DSM minus Pentacam Nadir uncorrected DSM (own illustration)



0 5 10 20 30 40 Meters

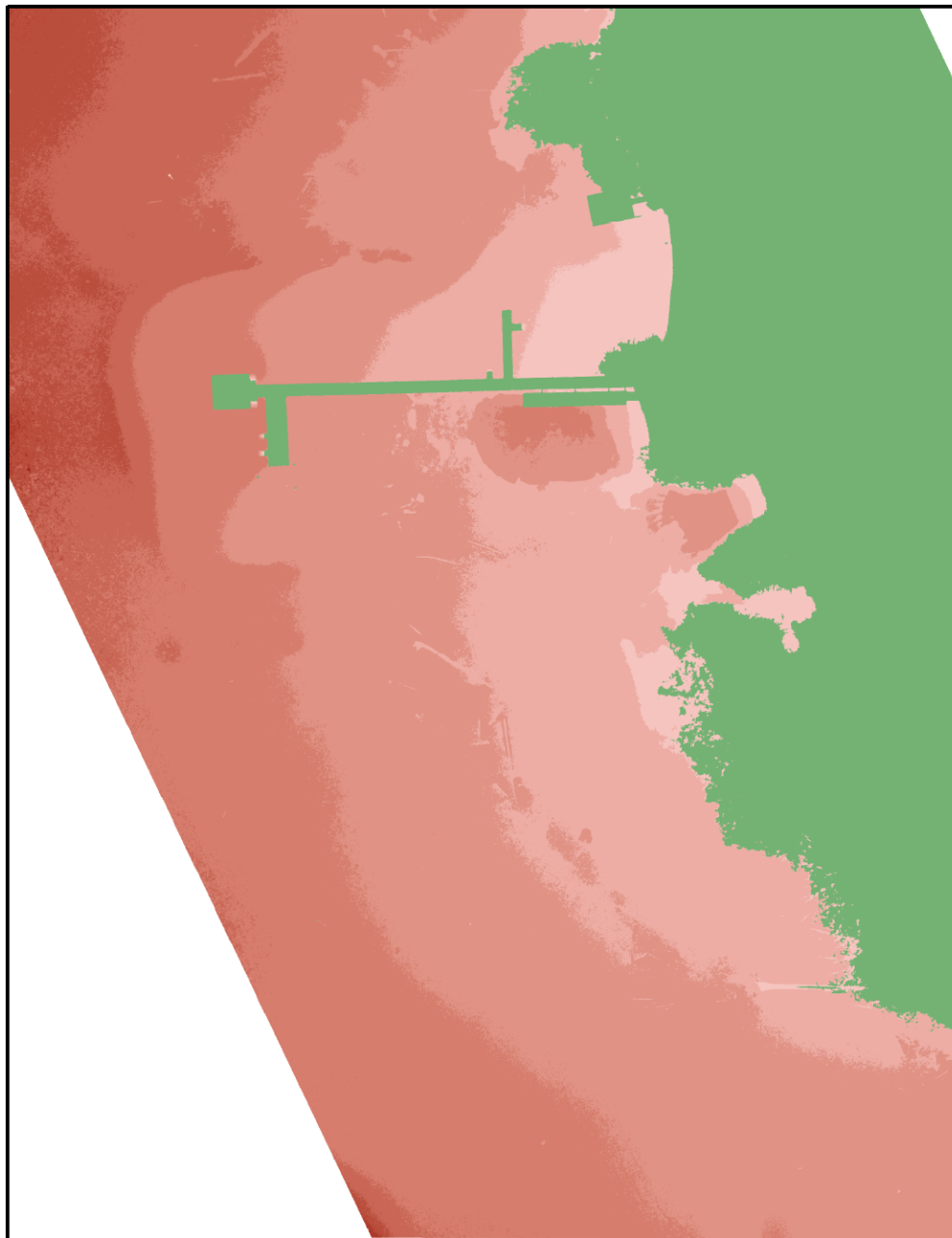
**height difference**

- 0- 0,09m
- 0,1 - 0,19m
- 0,2 - 0,29m
- 0,3 - 0,39m
- 0,4 - 0,49m
- 0,5 - 0,59m
- 0,6 - 0,69m
- 0,7 - 0,79m
- 0,8 - 0,9m

land area



Figure 50: Pentacam Oblique iterative Python script (index = 1,4) corrected DSM minus Pentacam Nadir uncorrected DSM (own illustration)



0 5 10 20 30 40 Meters

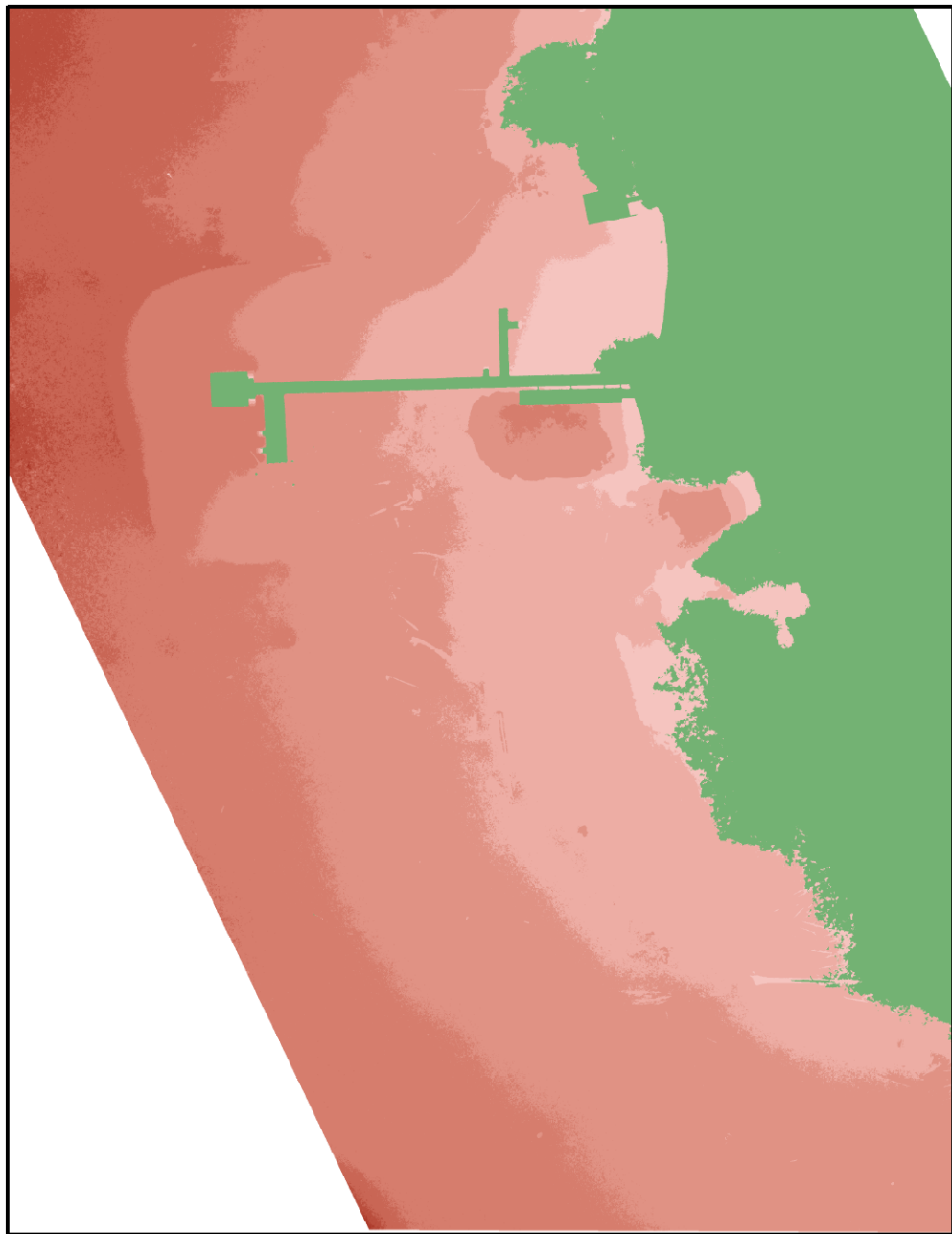
**height difference**

- 0 - 0,09m
- 0,1 - 0,19m
- 0,2 - 0,29m
- 0,3 - 0,39m
- 0,4 - 0,49m
- 0,5 - 0,59m
- 0,6 - 0,69m
- 0,7 - 0,79m
- 0,8 - 0,9m

land area



Figure 51: Sony Nadir clear water index corrected DSM minus Sony Nadir uncorrected DSM (own illustration)



0 5 10 20 30 40 Meters

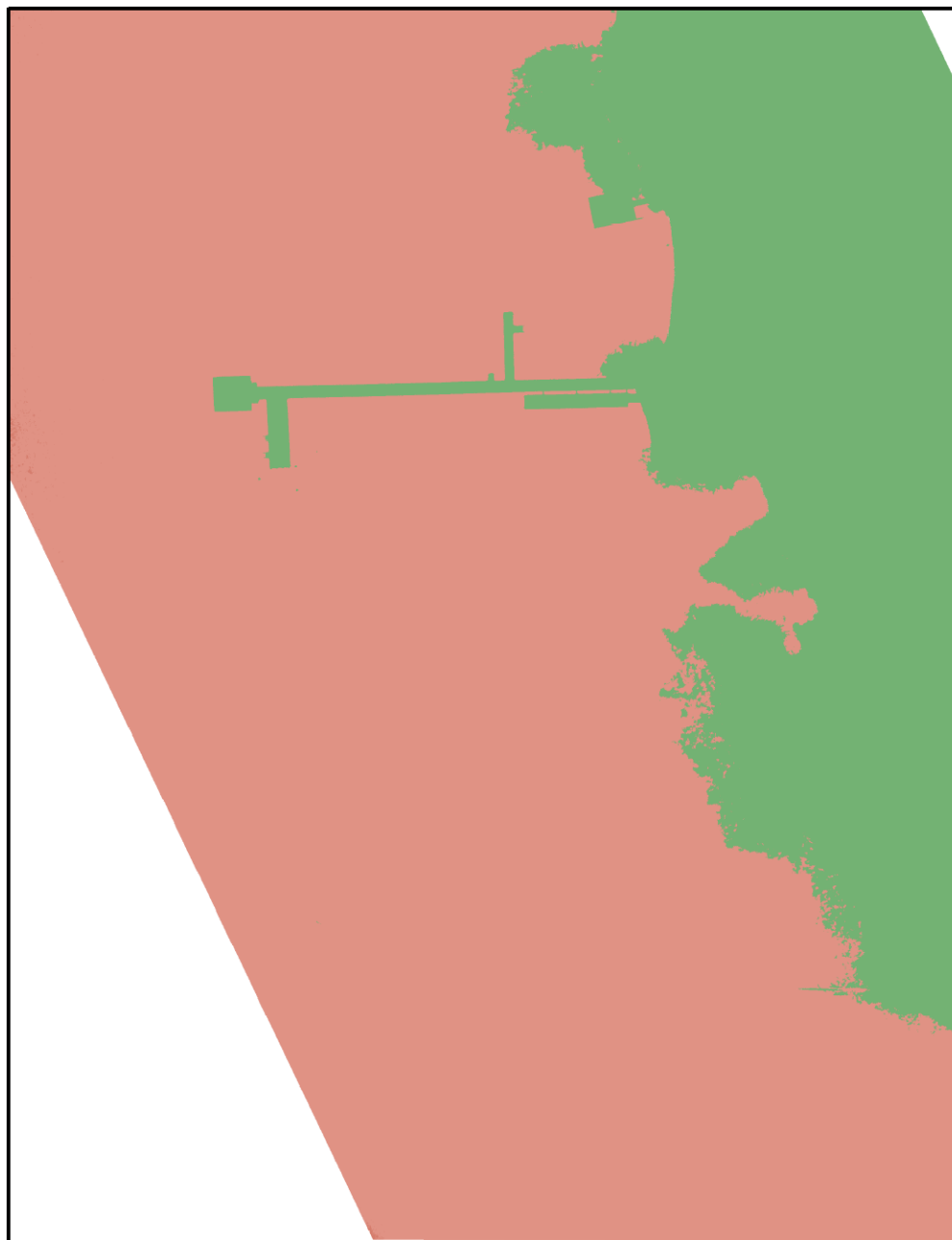
**height difference**

- 0 - 0,09m
- 0,1 - 0,19m
- 0,2 - 0,29m
- 0,3 - 0,39m
- 0,4 - 0,49m
- 0,5 - 0,59m
- 0,6 - 0,69m
- 0,7 - 0,79m
- 0,8 - 0,9m

land area



Figure 52: Sony Nadir derived factor corrected DSM minus Sony Nadir uncorrected DSM (own illustration)



0 5 10 20 30 40 Meters

**height difference**

- 0 - 0,09m
- 0,1 - 0,19m
- 0,2 - 0,29m
- 0,3 - 0,39m
- 0,4 - 0,49m
- 0,5 - 0,59m
- 0,6 - 0,69m
- 0,7 - 0,79m
- 0,8 - 0,9m

land area



Figure 53: Sony Nadir linear regression function corrected DSM minus Sony Nadir uncorrected DSM (own illustration)



0 5 10 20 30 40 Meters

**height difference**

- 0 - 0,09m
- 0,1 - 0,19m
- 0,2 - 0,29m
- 0,3 - 0,39m
- 0,4 - 0,49m
- 0,5 - 0,59m
- 0,6 - 0,69m
- 0,7 - 0,79m
- 0,8 - 0,9m

land area



Figure 54: Sony Nadir iterative Python script corrected DSM minus Sony Nadir uncorrected DSM (own illustration)

## **Appendix E: SfM DSM refraction corrected sensor comparison**

Figure 55-Figure 58 illustrate the water depth comparison between the Sony Nadir data set and the best performing Pentacam data set for each refraction correction approach.

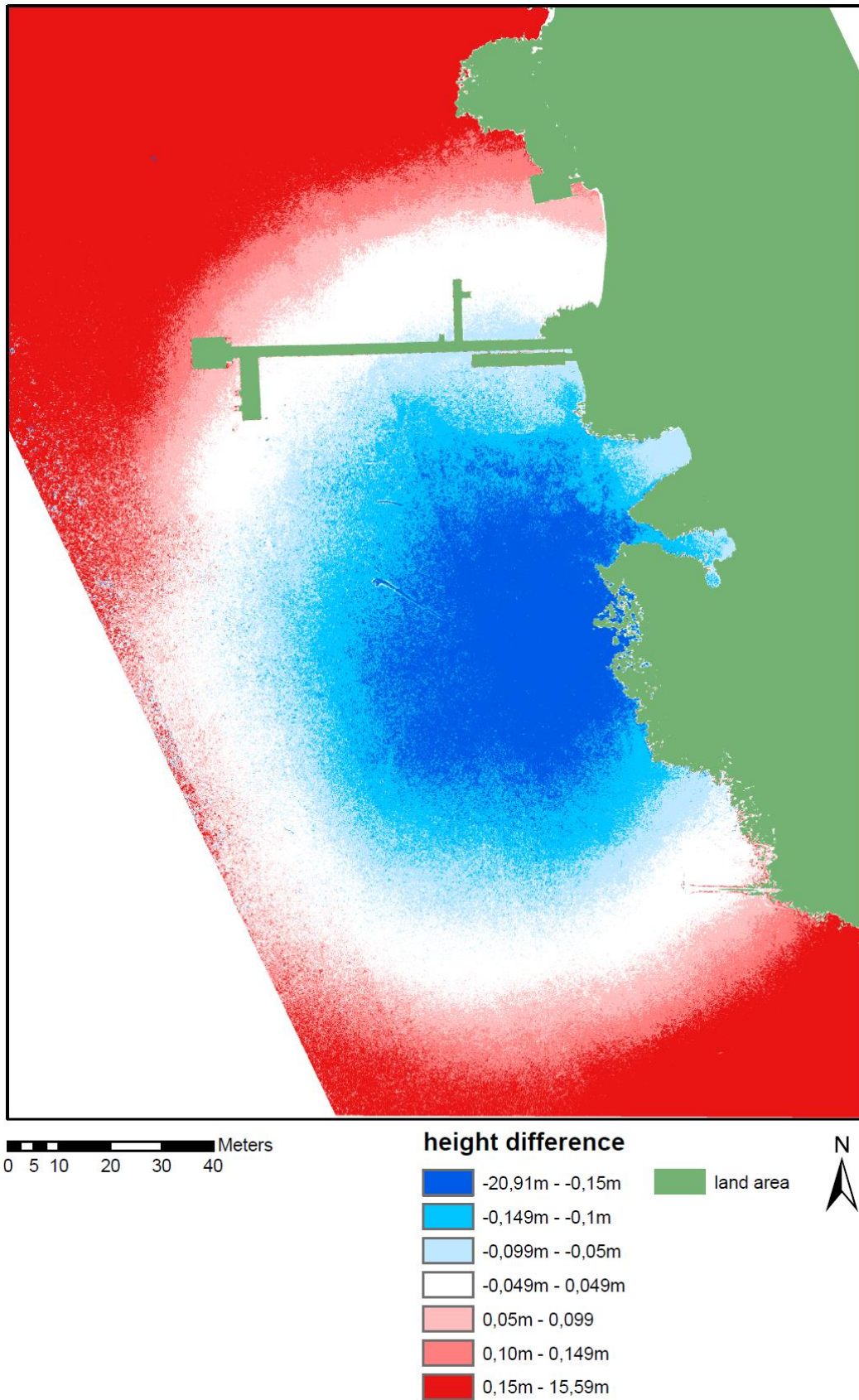
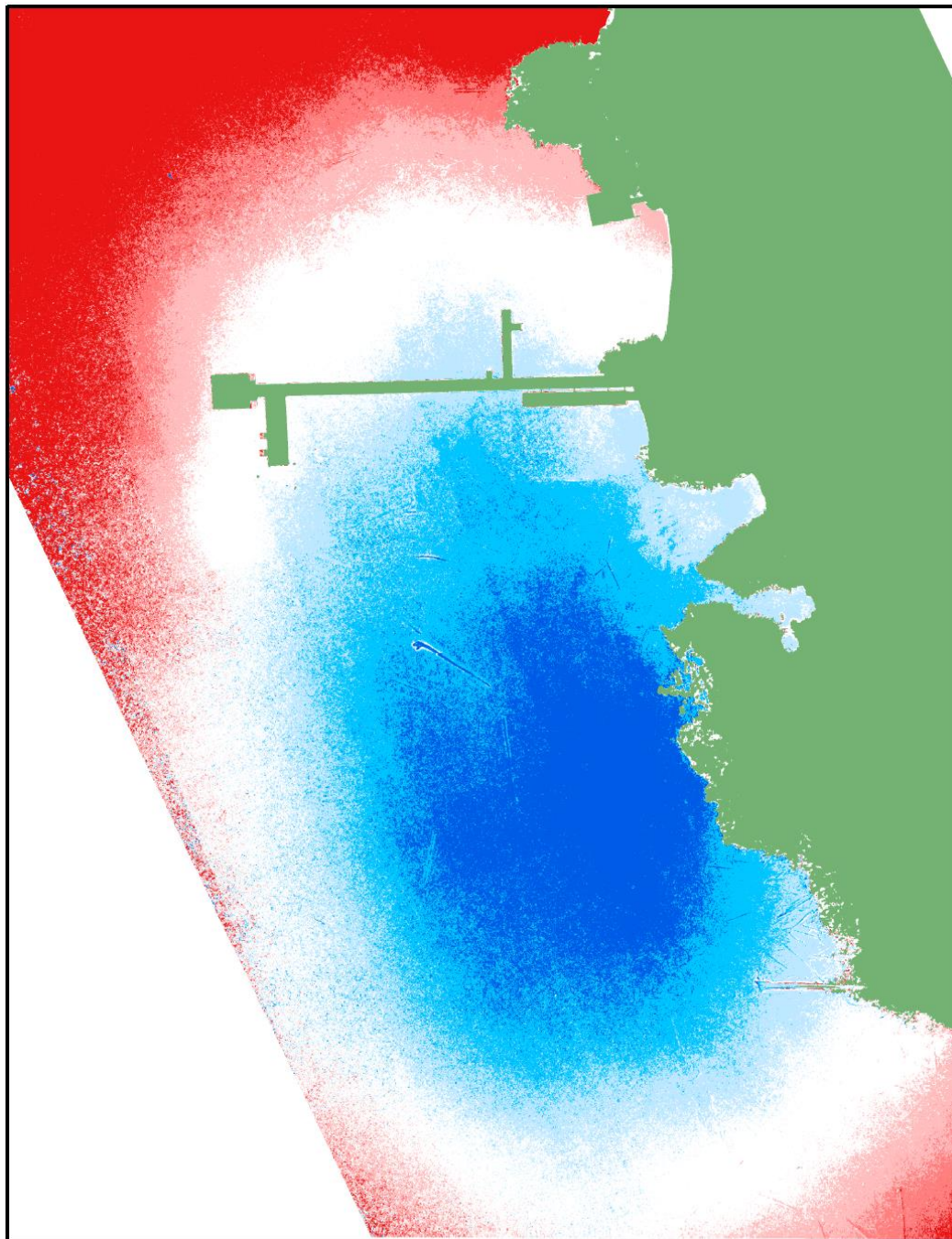


Figure 55: Sony Nadir DSM minus Pentacam Nadir both corrected via clearwater index (own illustration)

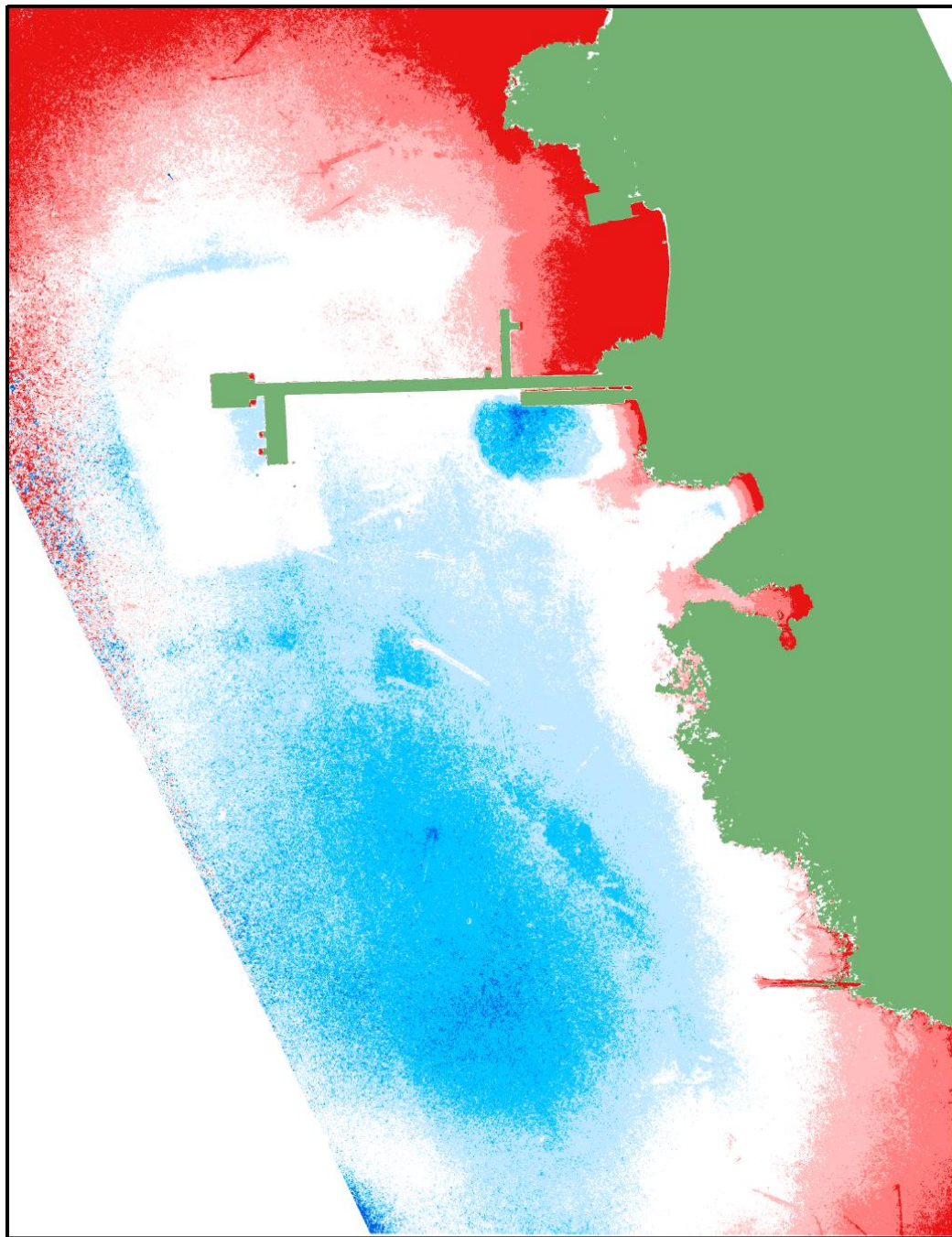


0 5 10 20 30 40 Meters

**height difference**



Figure 56: Sony Nadir DSM minus Pentacam All both corrected via derived factor from underwater reference points (own illustration)



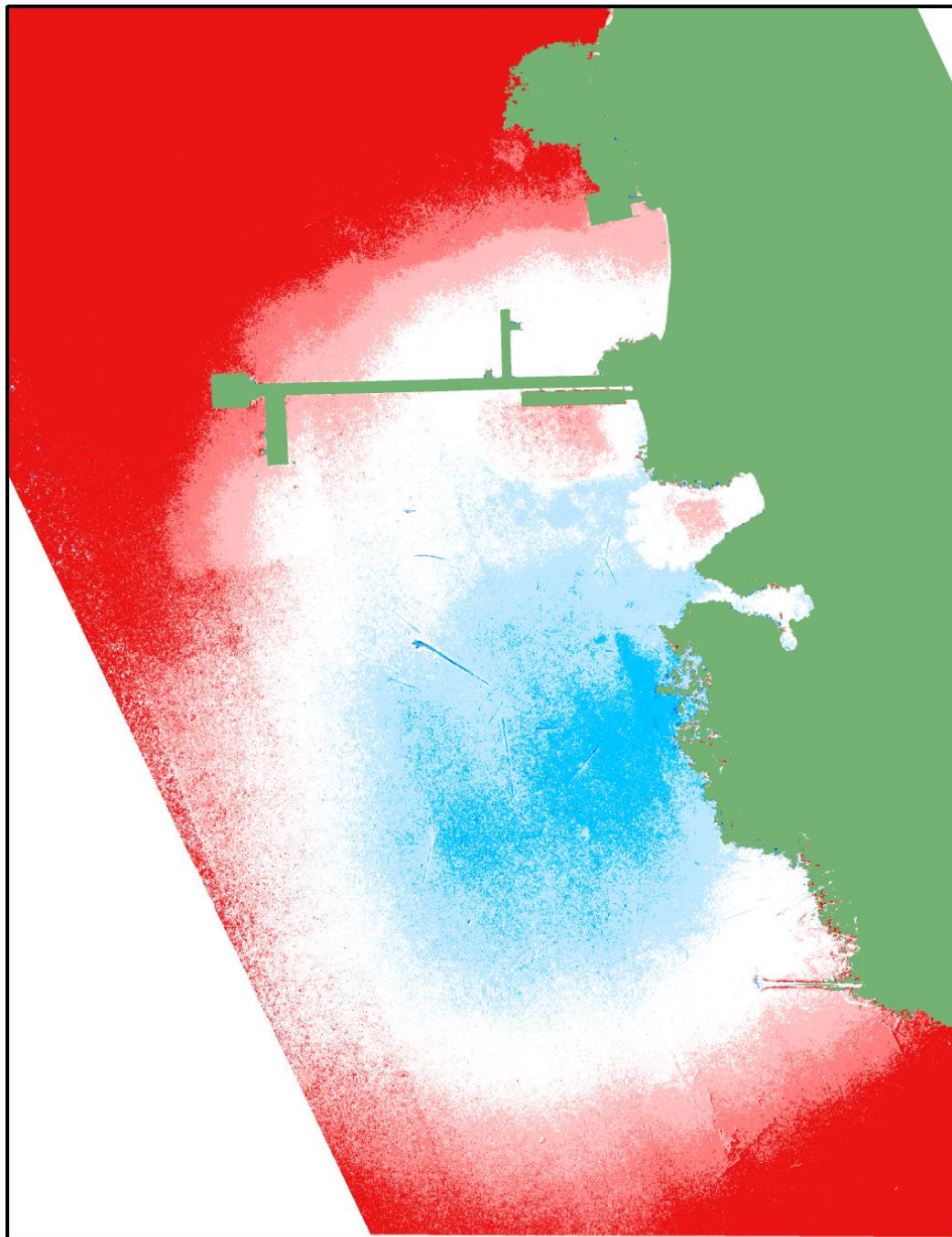
0 5 10 20 30 40 Meters

**height difference**

	-20,91m - -0,15m		land area
	-0,149m - -0,1m		
	-0,099m - -0,05m		
	-0,049m - 0,049m		
	0,05m - 0,099		
	0,10m - 0,149m		
	0,15m - 15,59m		



Figure 57: Sony Nadir DSM minus Pentacam All both corrected via linear regression function derived from underwater reference points (own illustration)



0 5 10 20 30 40 Meters

**height difference**

- 20,91m - -0,15m
- 0,149m - -0,1m
- 0,099m - -0,05m
- 0,049m - 0,049m
- 0,05m - 0,099
- 0,10m - 0,149m
- 0,15m - 15,59m

land area



Figure 58: Sony Nadir DSM minus Pentacam Oblique both corrected via iterative correcting Python script (own illustration)

## **Appendix F: Comparison, SfM data with Lidar data**

For this comparison, the lidar data were shifted by 1,3m in height to increase the comparability since they were not matching with the collected DGNS data.

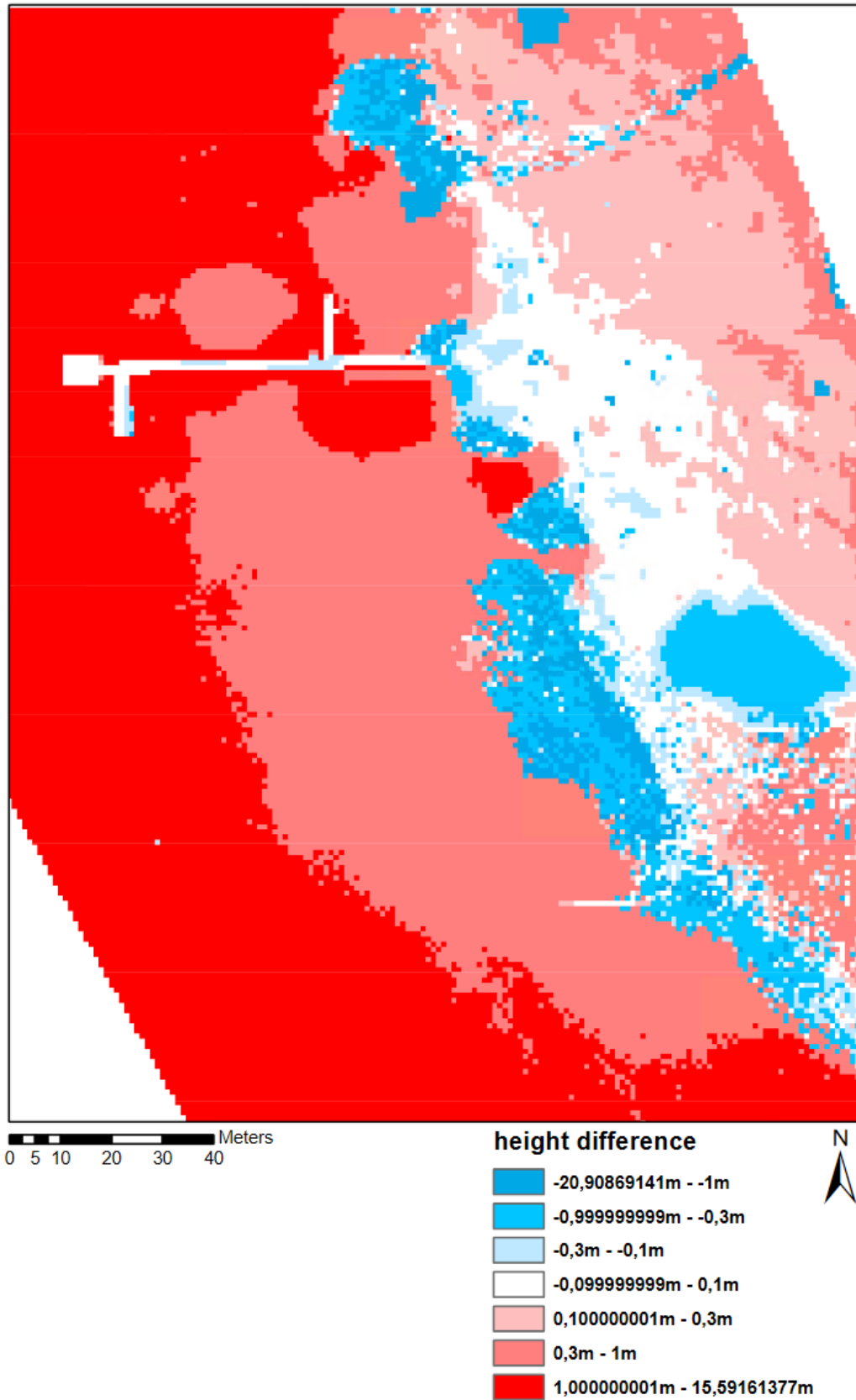


Figure 59: Lidar DEM height offset corrected(1,3m) minus SfM Sony Nadir factor corrected DSM (own illustration)

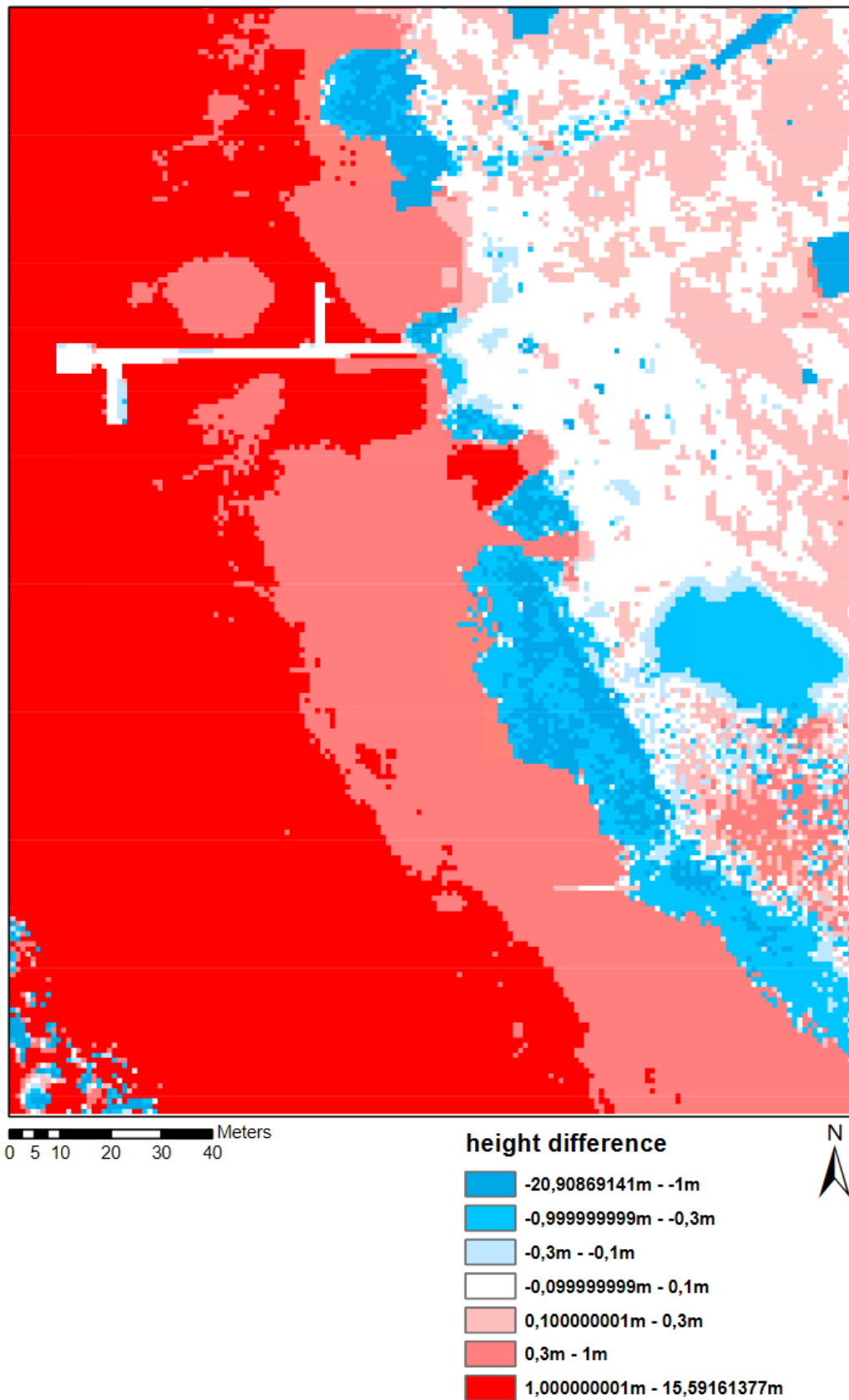


Figure 60: Lidar DEM height offset corrected(1,3m) minus SfM Pentacam all factor corrected DSM (own illustration)

## **Appendix G: Error histogram and scatterplot**

Figure 29-Figure 66 show all error histograms and scatterplots for all datasets created are shown. Starting with the uncorrected SfM data ( Figure 61) and followed by the refraction corrected SfM data with the clearwater index (CWI, Figure 62), calculated factor (CF, Figure 63), linear regression function (LRF, Figure 64), and two sets of error histograms for the refraction correction with the Python script (PS, Figure 65 and Figure 66).

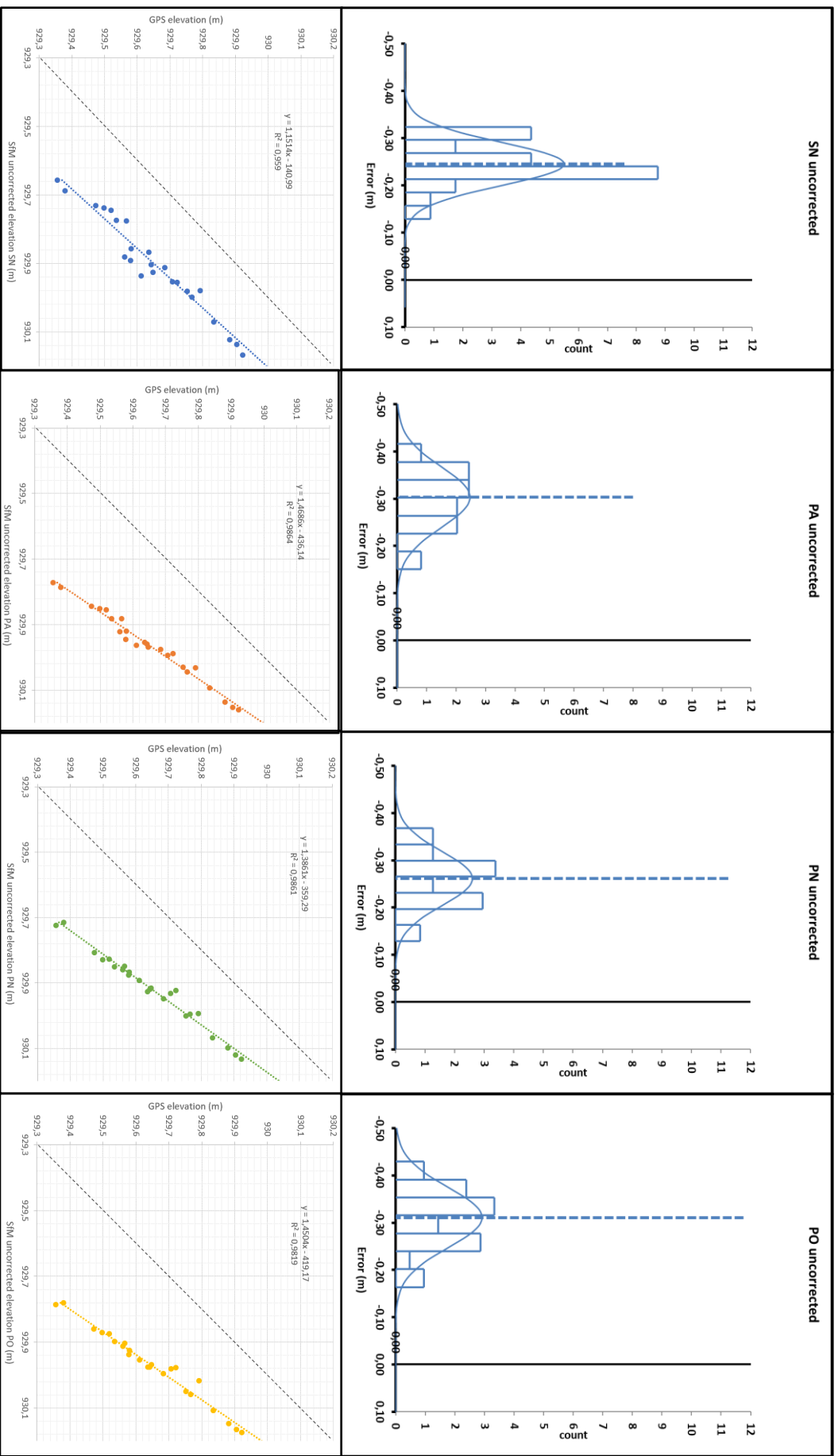


Figure 61: Error histograms and scatterplots for uncorrected SfM data (SN =Sony Nadir, PA= Pentacam All, PN= Pentacam Nadir, PO =Pentacam Oblique)

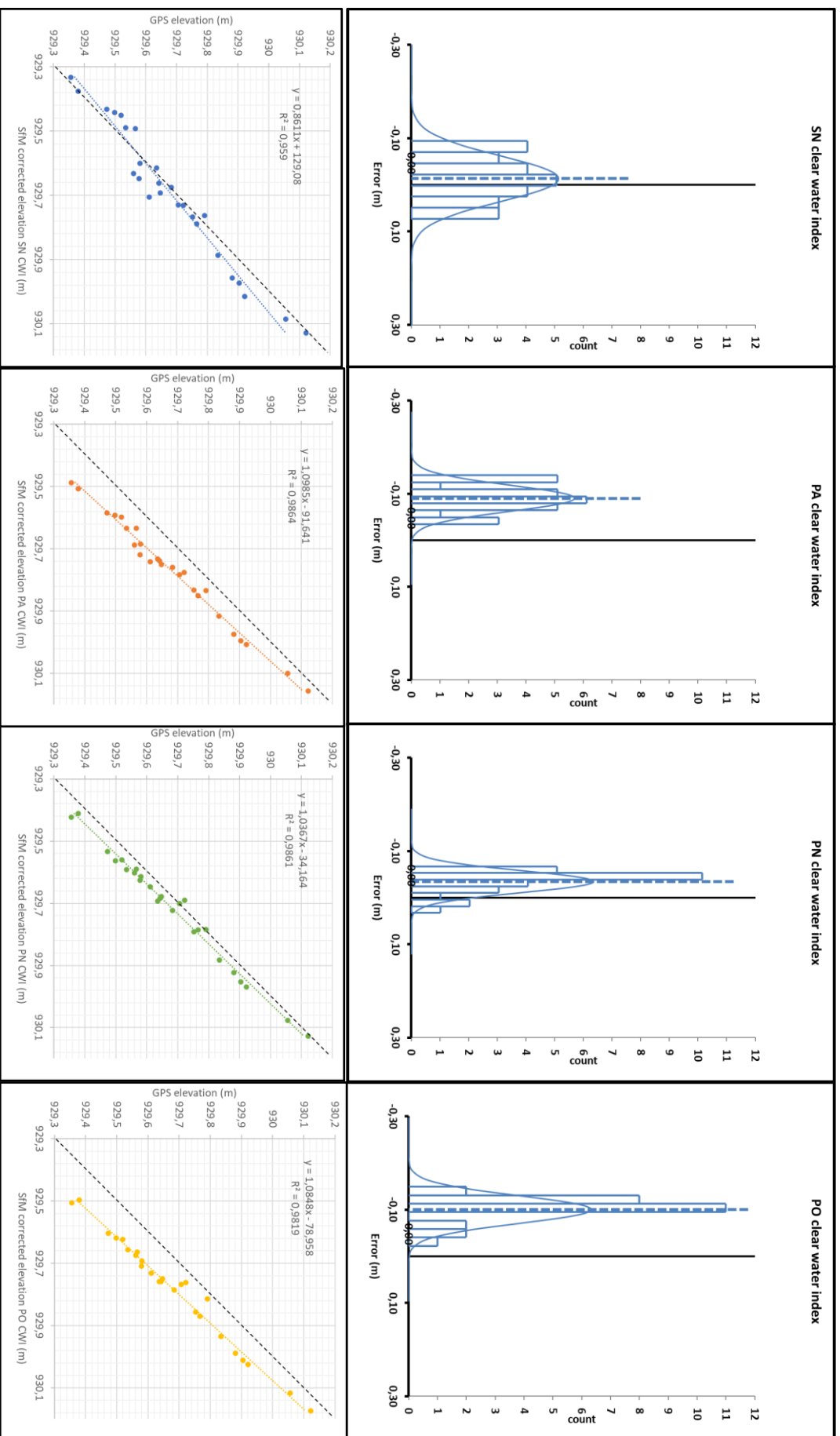


Figure 62: Error histograms and scatterplots for refraction correction via clear water index (SN = Sony Nadir, PA = Pentacam All, PN = Pentacam Nadir, PO = Pentacam Oblique), (own illustration)

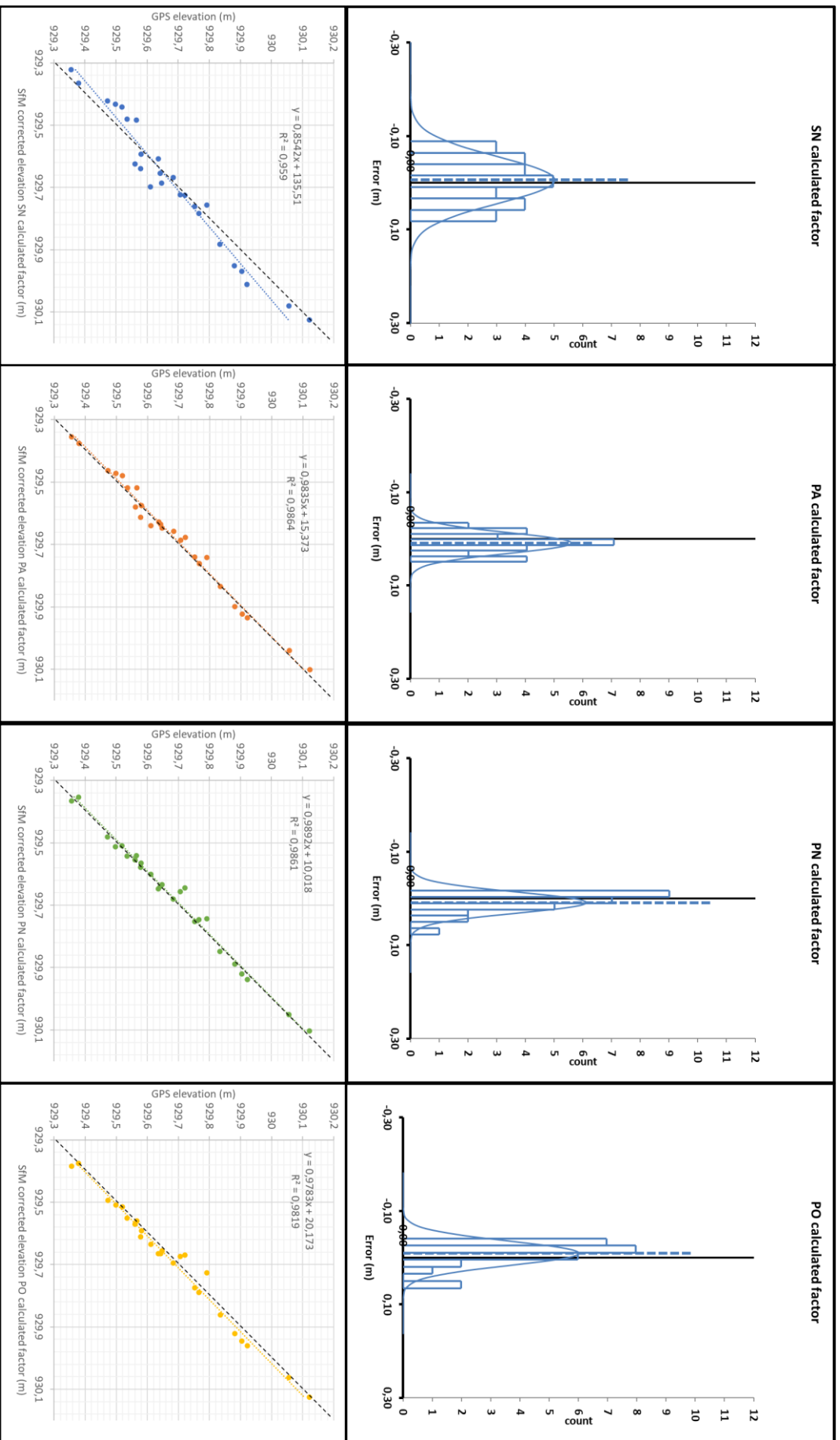


Figure 63: Error histograms and scatterplots for refraction correction via calculated factor (CF), (SN =Sony Nadir, PA= Pentacam All, PN= Pentacam Nadir, PO =Pentacam Oblique), (own illustration)

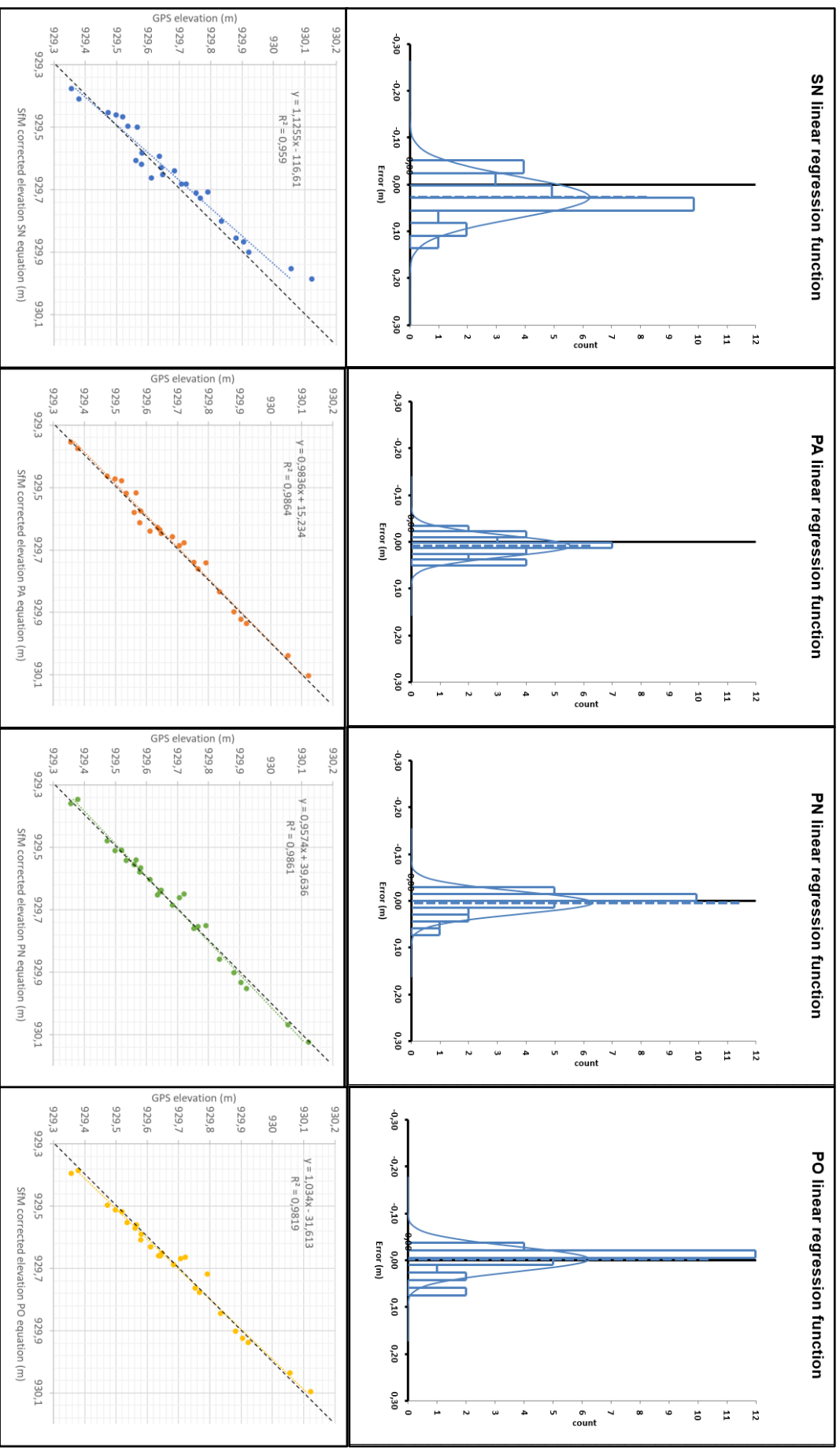


Figure 64: Error histograms and scatterplots for refraction correction via linear regression function (SN =Sony Nadir, PA= Pentacam AII, PN= Pentacam Nadir, PO =Pentacam Oblique), (own illustration)

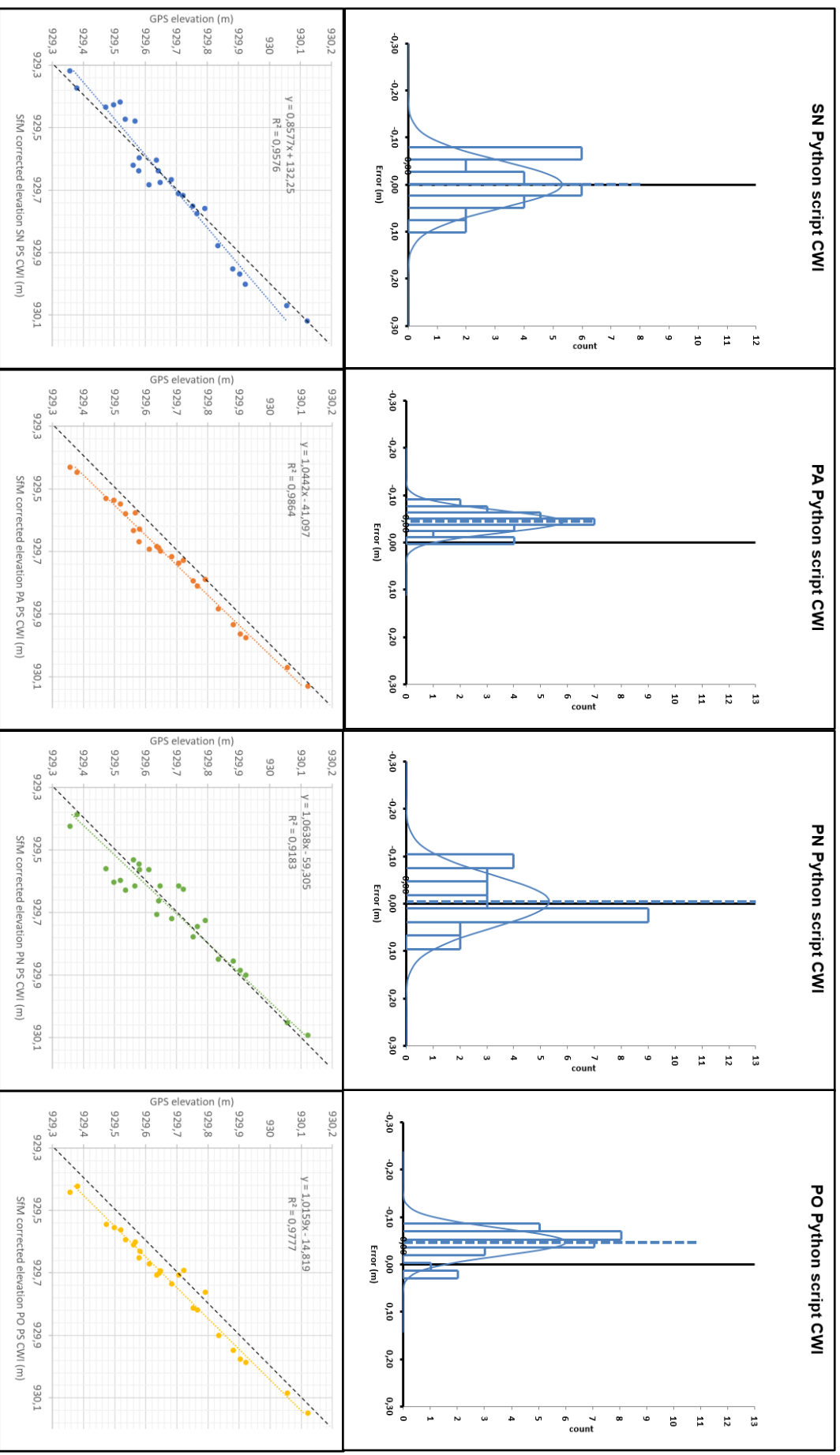


Figure 65: Error histograms and scatterplots for refraction correction via python script using the clearwater index (SN =Sony Nadir, PA= Pentacam All, PN= Pentacam Nadir, PO =Pentacam Oblique, CWI= clearwater index), (Own Illustration)

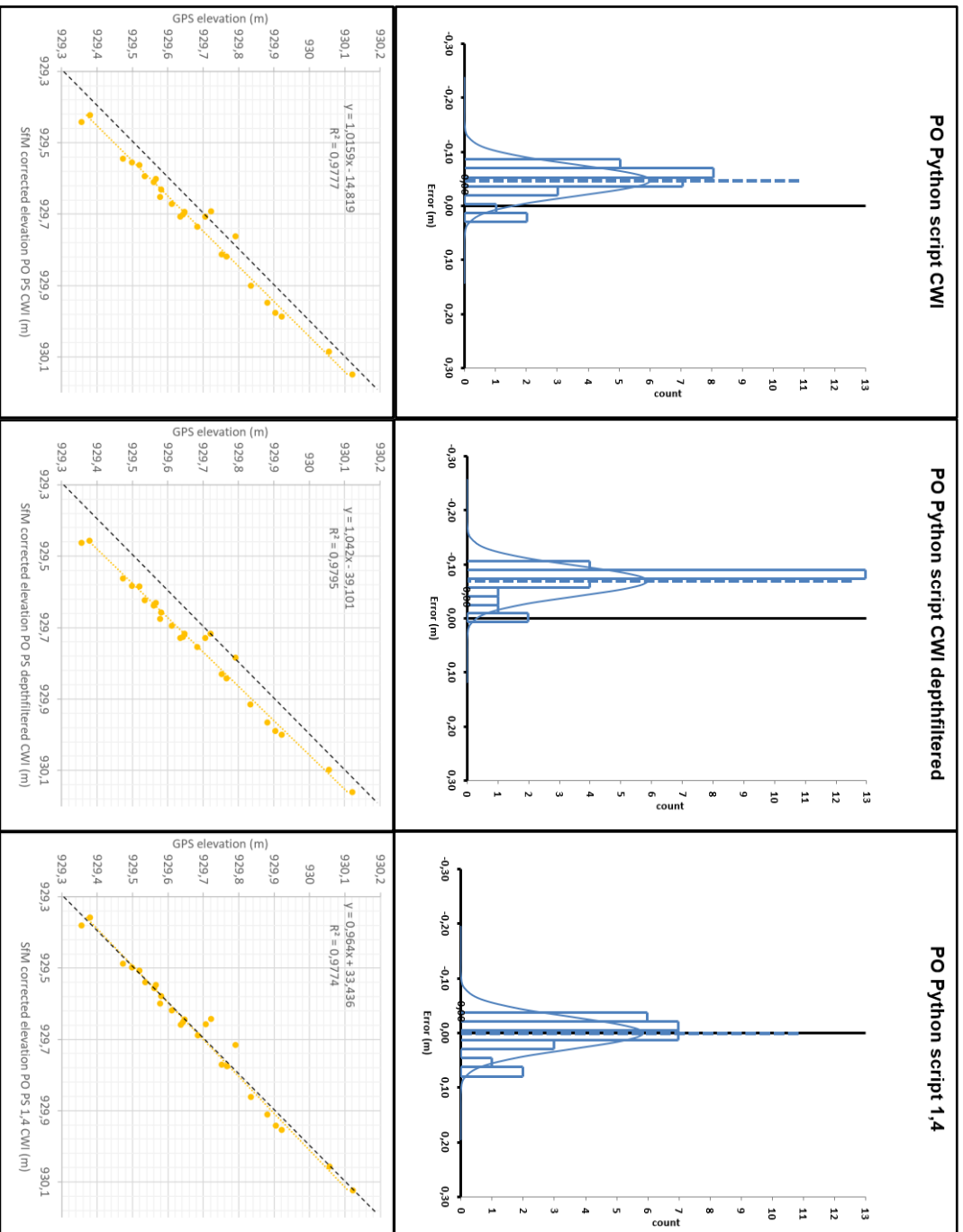
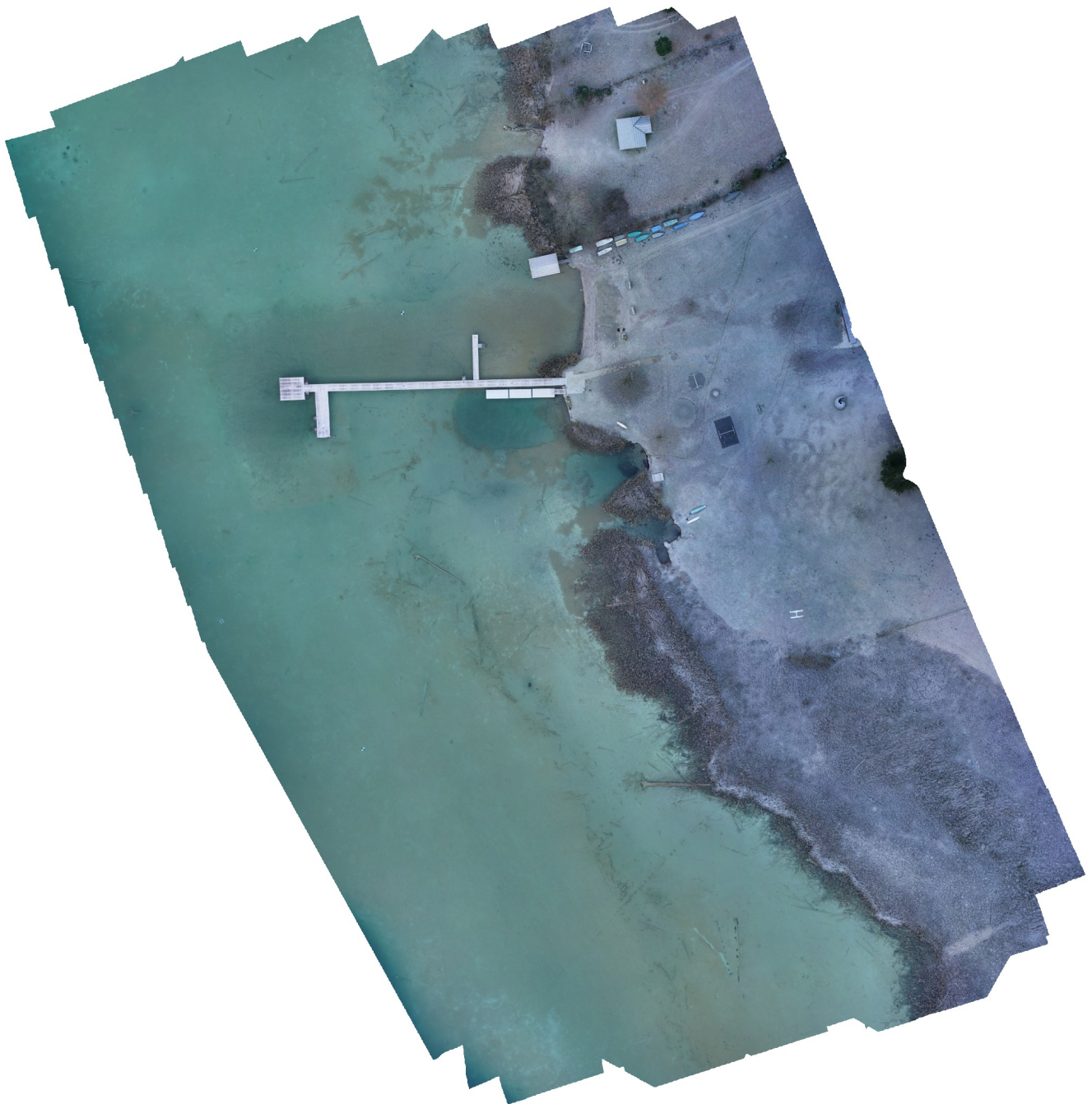


Figure 66: Error histograms and scatterplots for refraction correction via Python script for the PO (PO=Pentacam Oblique) data set with three different option (own illustration)

# Appendix H: Agisoft Metashape Professional Processing Report SN

SN - Pentacam nadir Photos

18 January 2021



# Survey Data

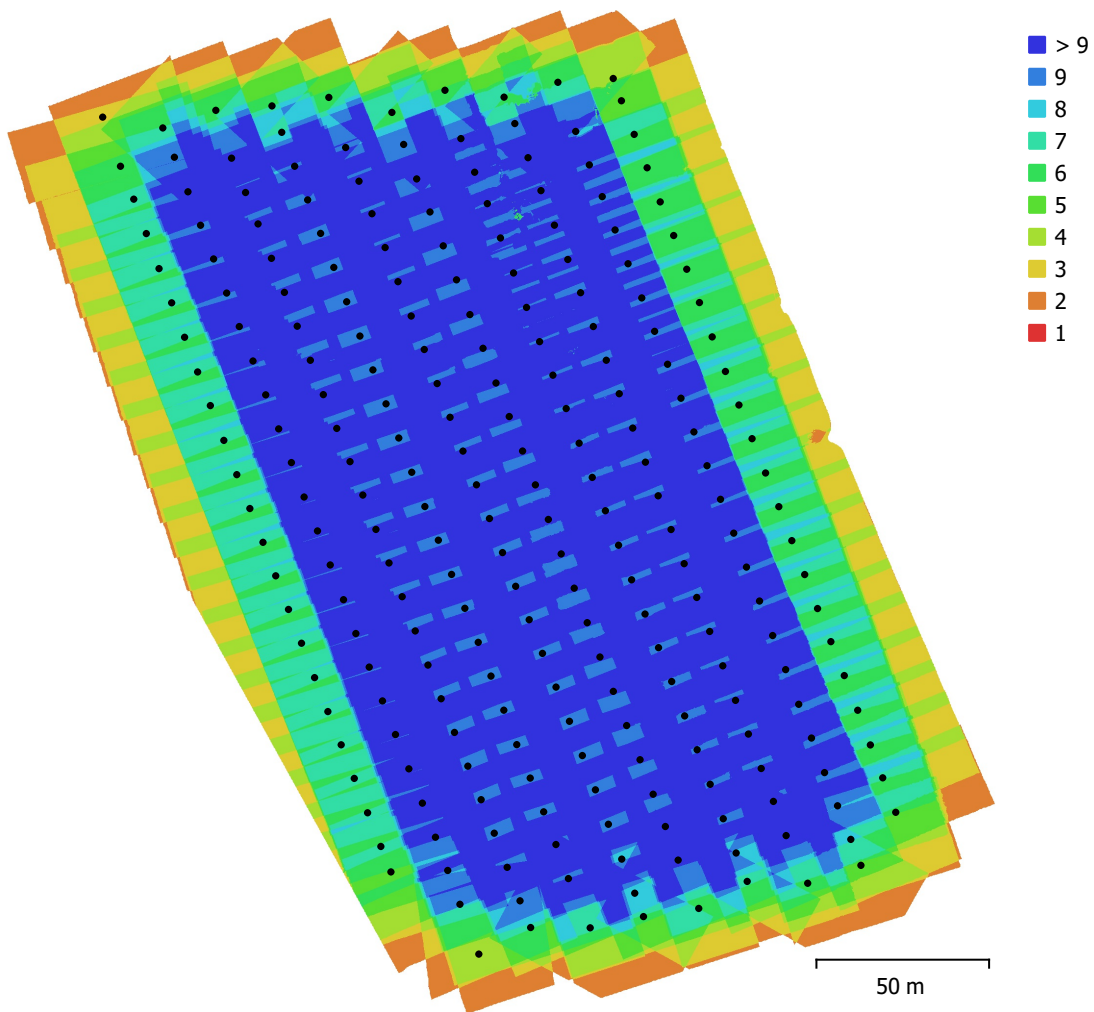


Fig. 1. Camera locations and image overlap.

Number of images:	242	Camera stations:	242
Flying altitude:	85.4 m	Tie points:	179,339
Ground resolution:	6.74 mm/pix	Projections:	708,717
Coverage area:	0.0526 km <sup>2</sup>	Reprojection error:	0.815 pix

Camera Model	Resolution	Focal Length	Pixel Size	Precalibrated
ILCE-7RM2 (55mm)	7952 x 5304	55 mm	4.53 x 4.53 $\mu$ m	No

Table 1. Cameras.

# Camera Calibration

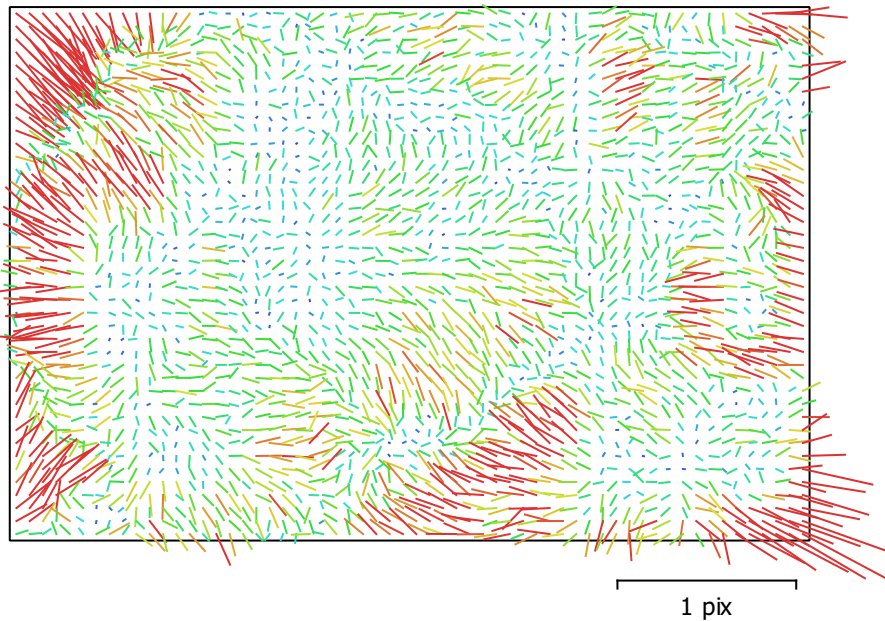


Fig. 2. Image residuals for ILCE-7RM2 (55mm).

## ILCE-7RM2 (55mm)

242 images

Type  
**Frame**

Resolution  
**7952 x 5304**

Focal Length  
**55 mm**

Pixel Size  
**4.53 x 4.53  $\mu\text{m}$**

	Value	Error	F	Cx	Cy	K1	K2	K3	P1	P2
<b>F</b>	<b>12412.5</b>	8.5	1.00	-0.93	0.77	0.52	-0.10	-0.14	-0.43	0.07
<b>Cx</b>	<b>-42.6048</b>	0.39		1.00	-0.71	-0.49	0.10	0.12	0.49	-0.06
<b>Cy</b>	<b>-32.0247</b>	0.2			1.00	0.35	-0.08	-0.11	-0.27	0.25
<b>K1</b>	<b>0.0028663</b>	0.00028				1.00	-0.33	0.17	-0.88	0.54
<b>K2</b>	<b>-0.0309285</b>	0.0013					1.00	-0.96	0.06	0.01
<b>K3</b>	<b>-0.251785</b>	0.0062						1.00	0.06	-0.04
<b>P1</b>	<b>-8.94791e-05</b>	6.2e-06							1.00	-0.54
<b>P2</b>	<b>-0.00121468</b>	2.5e-06								1.00

Table 2. Calibration coefficients and correlation matrix.

# Ground Control Points

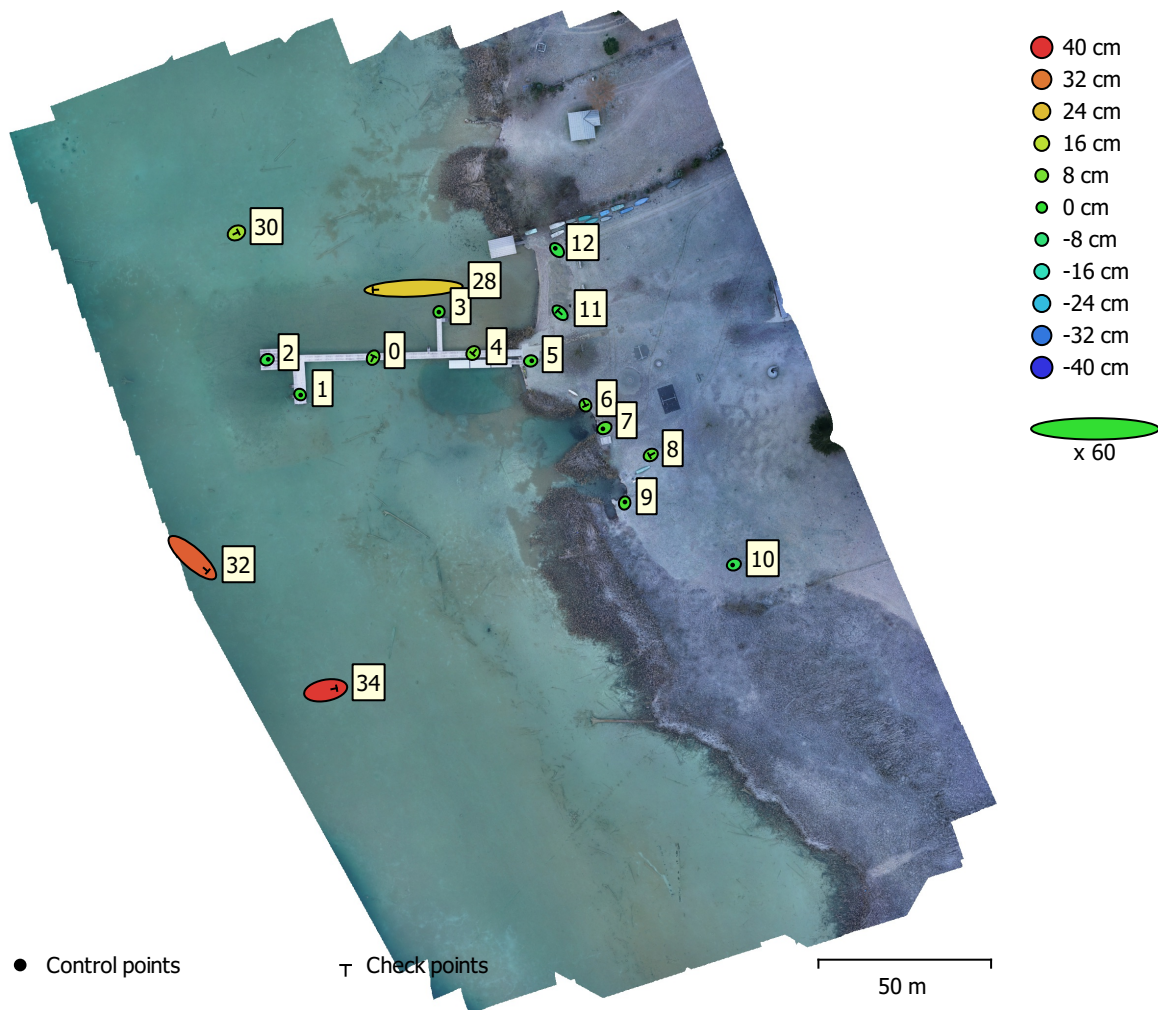


Fig. 3. GCP locations and error estimates.

Z error is represented by ellipse color. X,Y errors are represented by ellipse shape.

Estimated GCP locations are marked with a dot or crossing.

Count	X error (cm)	Y error (cm)	Z error (cm)	XY error (cm)	Total (cm)
8	1.05327	0.785304	2.60262	1.3138	2.91542

Table 3. Control points RMSE.

X - Easting, Y - Northing, Z - Altitude.

Count	X error (cm)	Y error (cm)	Z error (cm)	XY error (cm)	Total (cm)
9	14.5013	4.62332	19.9377	15.2205	25.0833

Table 4. Check points RMSE.

X - Easting, Y - Northing, Z - Altitude.

<b>Label</b>	<b>X error (cm)</b>	<b>Y error (cm)</b>	<b>Z error (cm)</b>	<b>Total (cm)</b>	<b>Image (pix)</b>
1	0.532502	-0.4706	0.982904	1.2129	0.409 (13)
2	1.0446	0.417815	-2.22808	2.49602	0.721 (13)
3	-0.130443	-0.240322	1.99061	2.0093	0.629 (14)
5	1.0404	0.147091	2.3472	2.57166	0.713 (13)
9	0.235253	0.94723	2.64046	2.81507	1.079 (9)
10	-1.22497	-0.392575	-3.58968	3.8132	0.971 (12)
12	-1.6818	1.70304	-2.54594	3.49437	0.955 (10)
7	-1.42001	-0.711683	3.52803	3.8691	0.863 (13)
<b>Total</b>	<b>1.05327</b>	<b>0.785304</b>	<b>2.60262</b>	<b>2.91542</b>	<b>0.797</b>

Table 5. Control points.  
X - Easting, Y - Northing, Z - Altitude.

<b>Label</b>	<b>X error (cm)</b>	<b>Y error (cm)</b>	<b>Z error (cm)</b>	<b>Total (cm)</b>	<b>Image (pix)</b>
0	0.670199	1.32111	5.26701	5.47137	0.822 (11)
4	-0.649207	-0.760563	7.69179	7.75651	0.340 (10)
6	0.241984	-0.510204	4.37035	4.40668	0.542 (9)
8	-1.25948	-0.693452	4.38047	4.61039	0.371 (9)
11	-2.35961	2.1513	-2.29008	3.92942	0.454 (13)
28	-39.3212	-1.58546	22.6561	45.4089	1.089 (13)
30	1.79151	0.887538	13.0685	13.2206	0.907 (14)
32	14.8976	-13.3125	34.8611	40.1803	0.784 (4)
34	10.6397	2.03901	39.3418	40.8061	0.844 (7)
<b>Total</b>	<b>14.5013</b>	<b>4.62332</b>	<b>19.9377</b>	<b>25.0833</b>	<b>0.742</b>

Table 6. Check points.  
X - Easting, Y - Northing, Z - Altitude.

# Digital Elevation Model

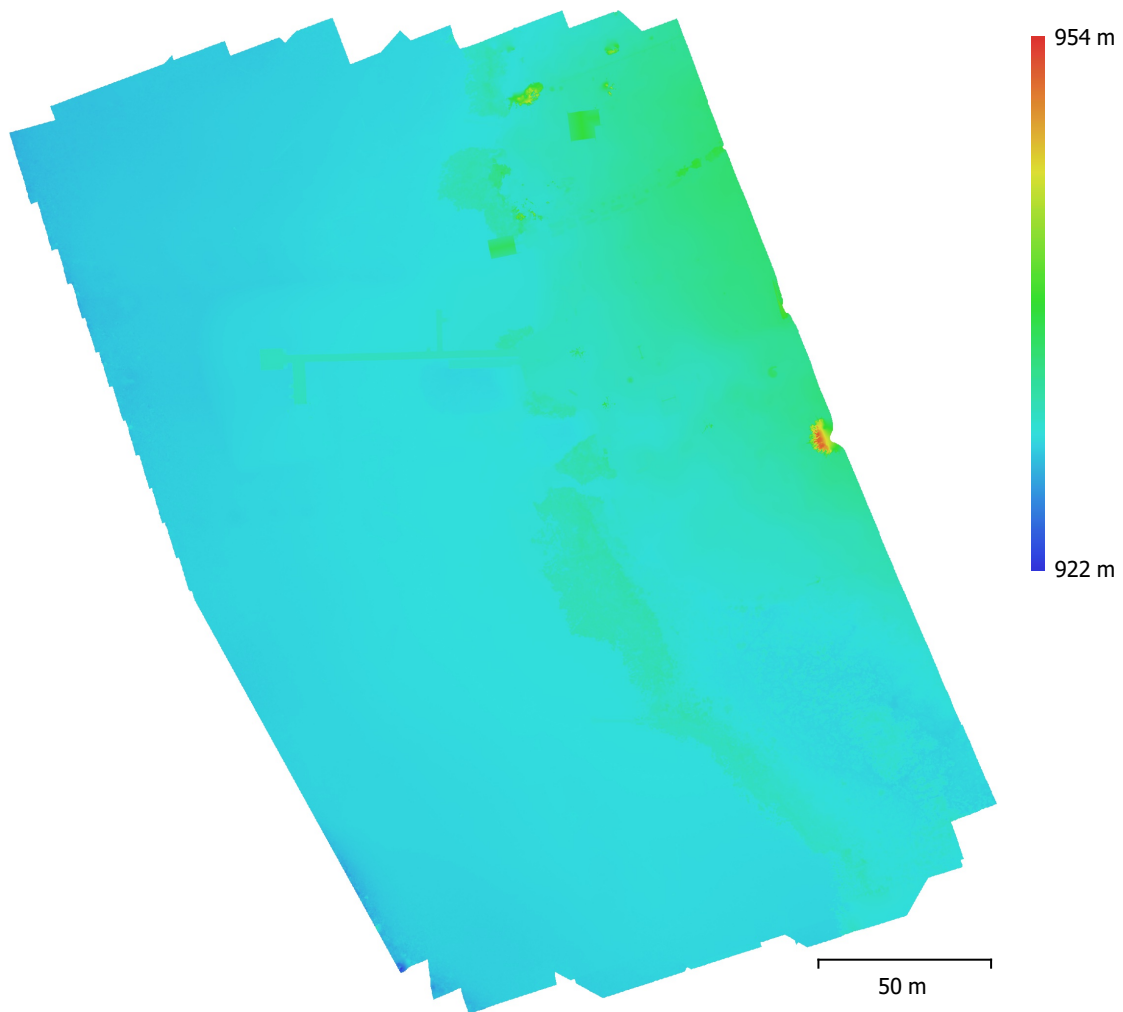


Fig. 4. Reconstructed digital elevation model.

Resolution: 1.35 cm/pix  
Point density: 0.55 points/cm<sup>2</sup>

# Processing Parameters

## General

Cameras	242
Aligned cameras	242
Markers	17

## Shapes

Polygons	242
Coordinate system	MGI / Austria GK Central (EPSG::31255)
Rotation angles	Yaw, Pitch, Roll

## Point Cloud

Points	179,339 of 190,502
RMS reprojection error	0.14608 (0.814608 pix)
Max reprojection error	0.439256 (30.8258 pix)
Mean key point size	5.23937 pix
Point colors	3 bands, uint8
Key points	No
Average tie point multiplicity	4.05394

## Alignment parameters

Accuracy	High
Generic preselection	Yes
Key point limit	40,000
Tie point limit	4,000
Adaptive camera model fitting	No
Matching time	5 minutes 0 seconds
Alignment time	2 minutes 54 seconds
Software version	1.5.5.9097
File size	16.47 MB

## Depth Maps

Count	242
-------	-----

## Depth maps generation parameters

Quality	High
Filtering mode	Mild
Processing time	58 minutes 48 seconds
Software version	1.5.5.9097
File size	2.76 GB

## Dense Point Cloud

Points	424,346,033
Point colors	3 bands, uint8

## Depth maps generation parameters

Quality	High
Filtering mode	Mild
Processing time	58 minutes 48 seconds

## Dense cloud generation parameters

Processing time	1 hours 26 minutes
Software version	1.5.5.9097
File size	5.40 GB

## DEM

Size	27,258 x 31,627
Coordinate system	MGI / Austria GK Central (EPSG::31255)

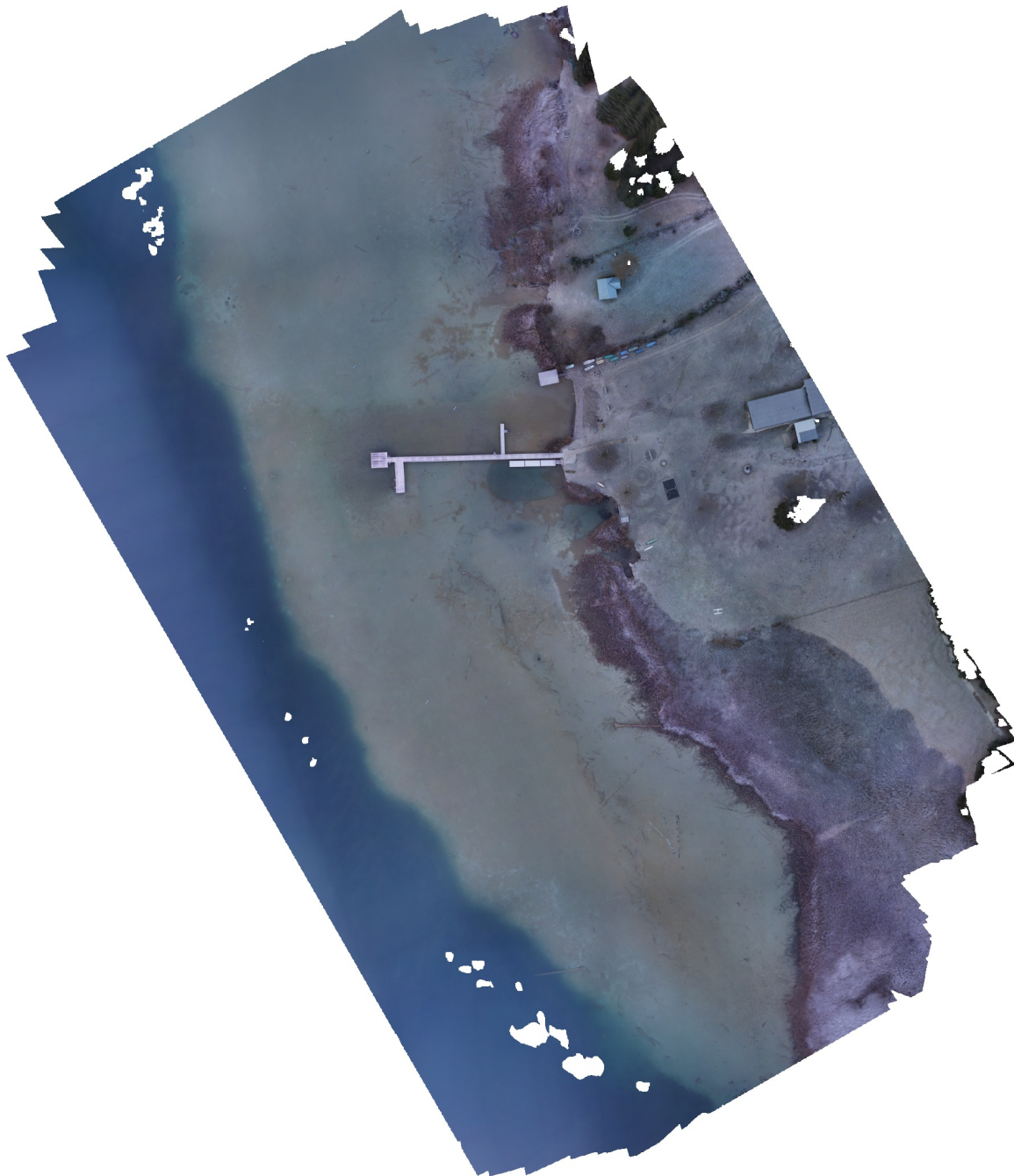
## Reconstruction parameters

Source data	Dense cloud
Interpolation	Enabled

Processing time	10 minutes 53 seconds
Software version	1.5.5.9097
File size	841.72 MB
<b>Orthomosaic</b>	
Size	14,289 x 14,521
Coordinate system	MGI / Austria GK Central (EPSG::31255)
Colors	3 bands, uint8
<b>Reconstruction parameters</b>	
Blending mode	Mosaic
Surface	DEM
Enable hole filling	Yes
Processing time	7 minutes 59 seconds
Memory usage	3.63 GB
Software version	1.6.5.11249
File size	1.40 GB
<b>System</b>	
Software name	Agisoft Metashape Professional
Software version	1.6.5 build 11249
OS	Windows 64 bit
RAM	511.87 GB
CPU	Intel(R) Xeon(R) CPU E5-2620 v4 @ 2.10GHz
GPU(s)	Tesla P100-PCI-E-16GB

# Appendix I: Agisoft Metashape Professional Processing Report PA

PA - Pentacam all Photos  
18 January 2021



# Survey Data

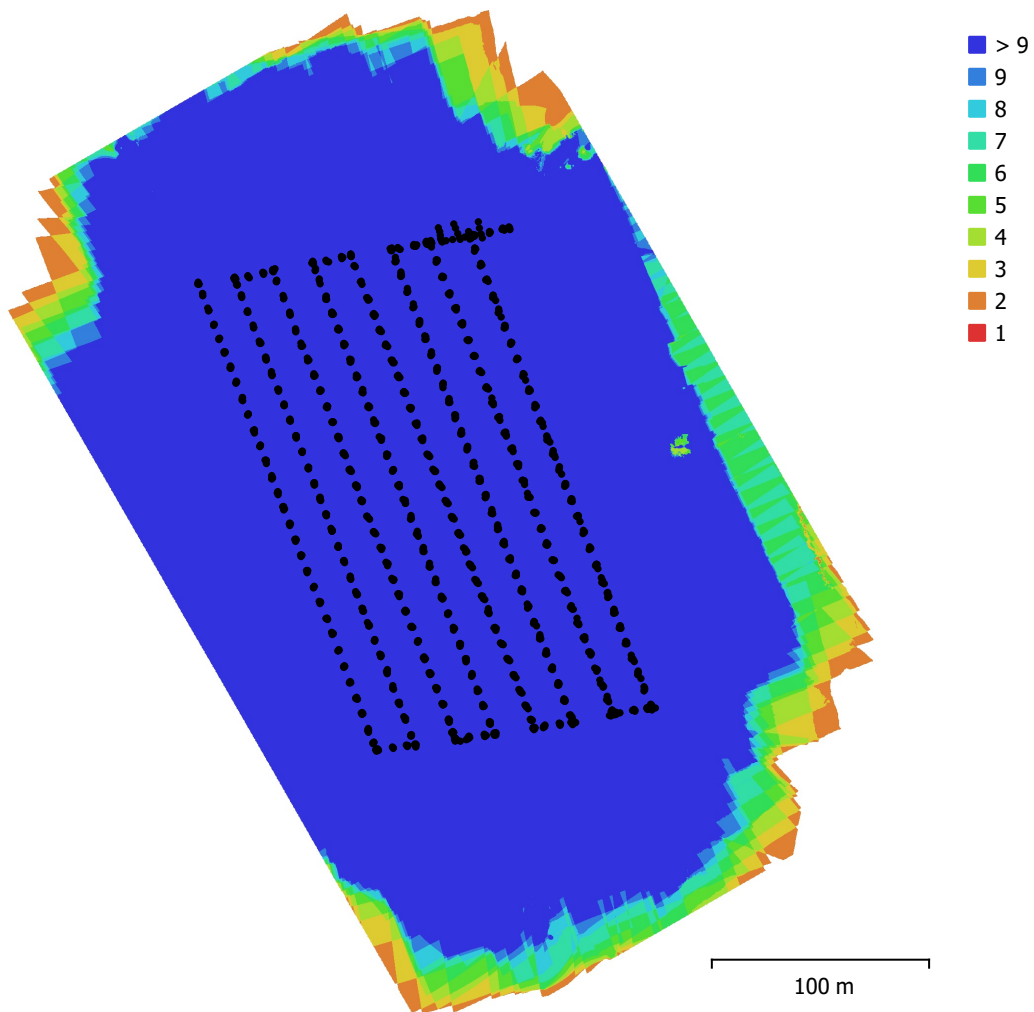


Fig. 1. Camera locations and image overlap.

Number of images:	1,404	Camera stations:	1,403
Flying altitude:	101 m	Tie points:	684,359
Ground resolution:	1.19 cm/pix	Projections:	3,342,826
Coverage area:	0.111 km <sup>2</sup>	Reprojection error:	1.31 pix

Camera Model	Resolution	Focal Length	Pixel Size	Precalibrated
ILCE-QX1	5456 x 3632	35 mm	4.25 x 4.25 $\mu$ m	No

Table 1. Cameras.

# Camera Calibration

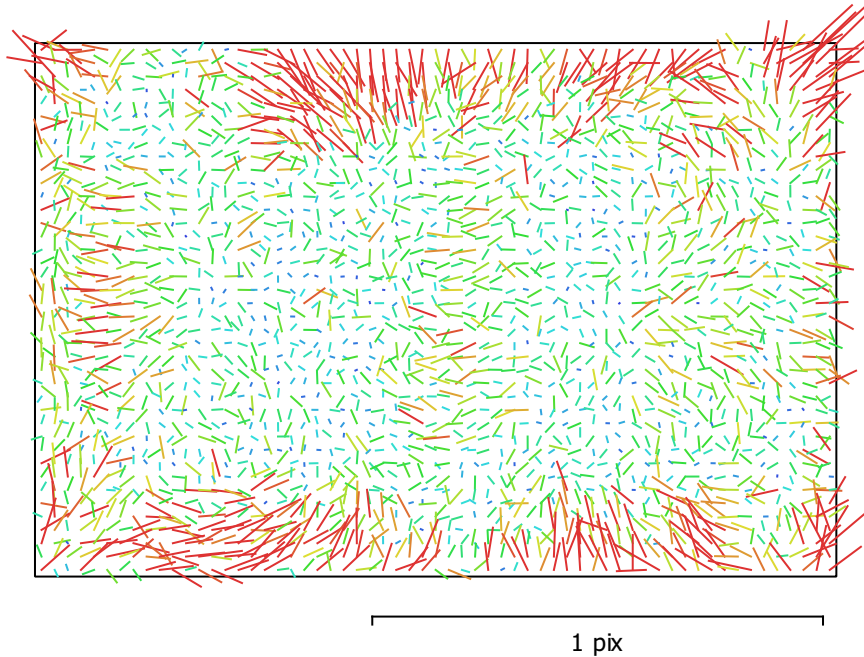


Fig. 2. Image residuals for ILCE-QX1.

## ILCE-QX1

1404 images

Type	Resolution	Focal Length	Pixel Size
<b>Frame</b>	<b>5456 x 3632</b>	<b>35 mm</b>	<b>4.25 x 4.25 <math>\mu\text{m}</math></b>
F:	8504.82		
Cx:	-21.4592	B1:	0
Cy:	15.4426	B2:	0
K1:	-0.0555496	P1:	-0.000320344
K2:	0.0435613	P2:	0.000118418
K3:	0.935693	P3:	0
K4:	0	P4:	0

# Ground Control Points

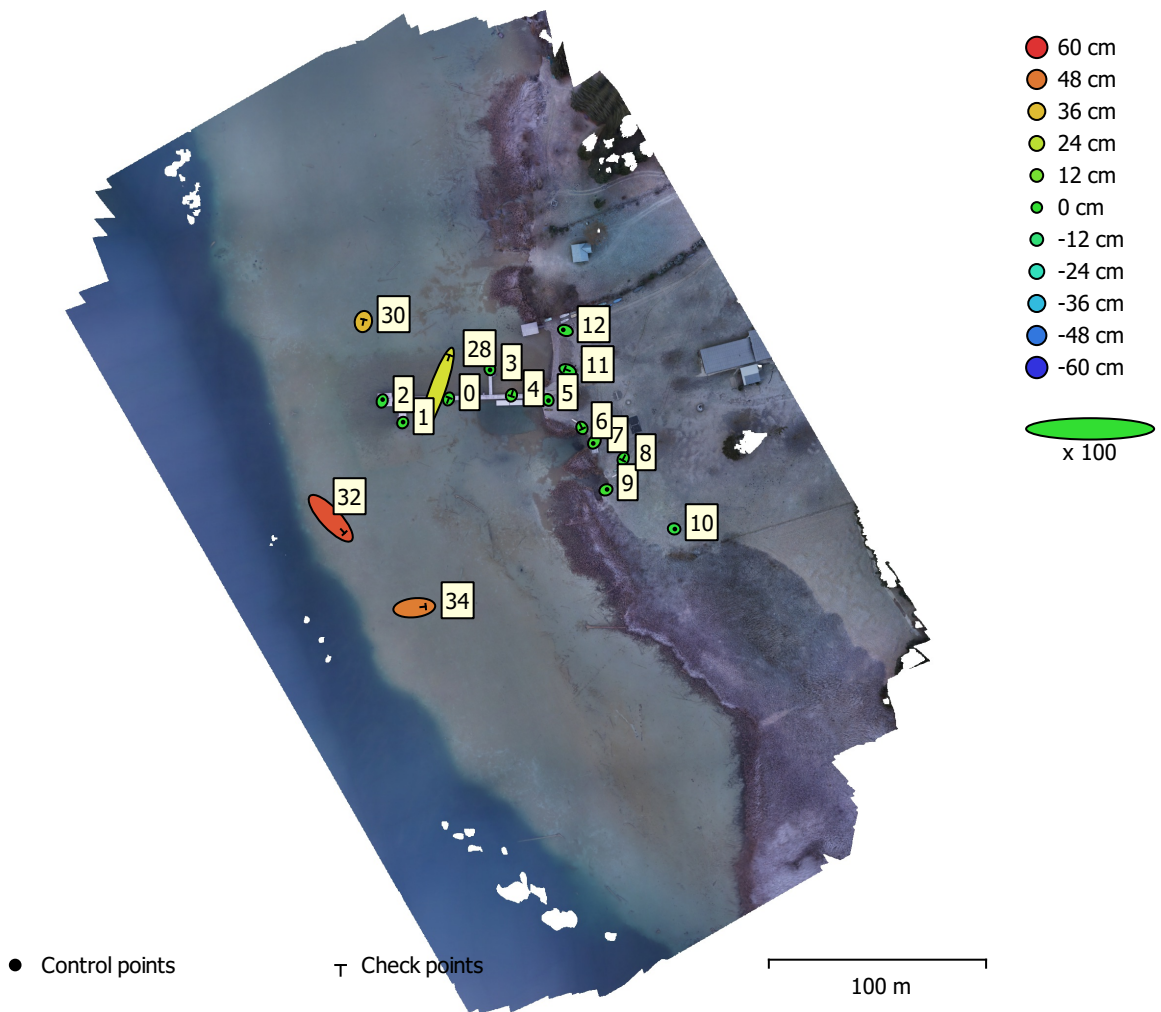


Fig. 3. GCP locations and error estimates.

Z error is represented by ellipse color. X,Y errors are represented by ellipse shape.

Estimated GCP locations are marked with a dot or crossing.

Count	X error (cm)	Y error (cm)	Z error (cm)	XY error (cm)	Total (cm)
8	0.934402	0.772815	1.69049	1.21258	2.08041

Table 2. Control points RMSE.

X - Easting, Y - Northing, Z - Altitude.

Count	X error (cm)	Y error (cm)	Z error (cm)	XY error (cm)	Total (cm)
9	6.79198	11.9255	28.5821	13.724	31.7062

Table 3. Check points RMSE.

X - Easting, Y - Northing, Z - Altitude.

<b>Label</b>	<b>X error (cm)</b>	<b>Y error (cm)</b>	<b>Z error (cm)</b>	<b>Total (cm)</b>	<b>Image (pix)</b>
1	0.315015	0.444828	0.772689	0.945597	1.217 (89)
2	0.405924	1.25547	-1.25133	1.81847	1.810 (87)
3	0.172742	-0.66556	-0.558499	0.885851	1.357 (84)
5	0.384856	-0.627993	-0.356105	0.818108	1.094 (85)
7	-1.04882	-1.27022	2.82963	3.27418	0.587 (77)
9	1.05268	0.409222	1.9505	2.25389	0.525 (74)
10	0.684033	-0.148649	-2.85826	2.94273	0.773 (50)
12	-1.96643	0.602903	-0.528613	2.12362	0.408 (53)
<b>Total</b>	<b>0.934402</b>	<b>0.772815</b>	<b>1.69049</b>	<b>2.08041</b>	<b>1.126</b>

Table 4. Control points.  
X - Easting, Y - Northing, Z - Altitude.

<b>Label</b>	<b>X error (cm)</b>	<b>Y error (cm)</b>	<b>Z error (cm)</b>	<b>Total (cm)</b>	<b>Image (pix)</b>
0	0.443717	1.12902	0.539977	1.32784	1.570 (95)
4	-0.264585	-0.803893	1.99779	2.16966	1.233 (87)
6	0.409056	-0.834896	1.55027	1.80768	0.652 (75)
8	-0.627966	-1.23392	0.68937	1.54665	0.865 (44)
11	-2.74516	1.06843	-1.60248	3.35342	0.449 (48)
28	11.5748	32.9047	28.5131	45.0521	0.966 (51)
30	0.412406	1.86786	36.7178	36.7676	1.258 (34)
32	12.7179	-13.6864	54.5587	57.669	1.033 (74)
34	10.532	1.07518	46.9556	48.1343	1.086 (97)
<b>Total</b>	<b>6.79198</b>	<b>11.9255</b>	<b>28.5821</b>	<b>31.7062</b>	<b>1.103</b>

Table 5. Check points.  
X - Easting, Y - Northing, Z - Altitude.

# Digital Elevation Model

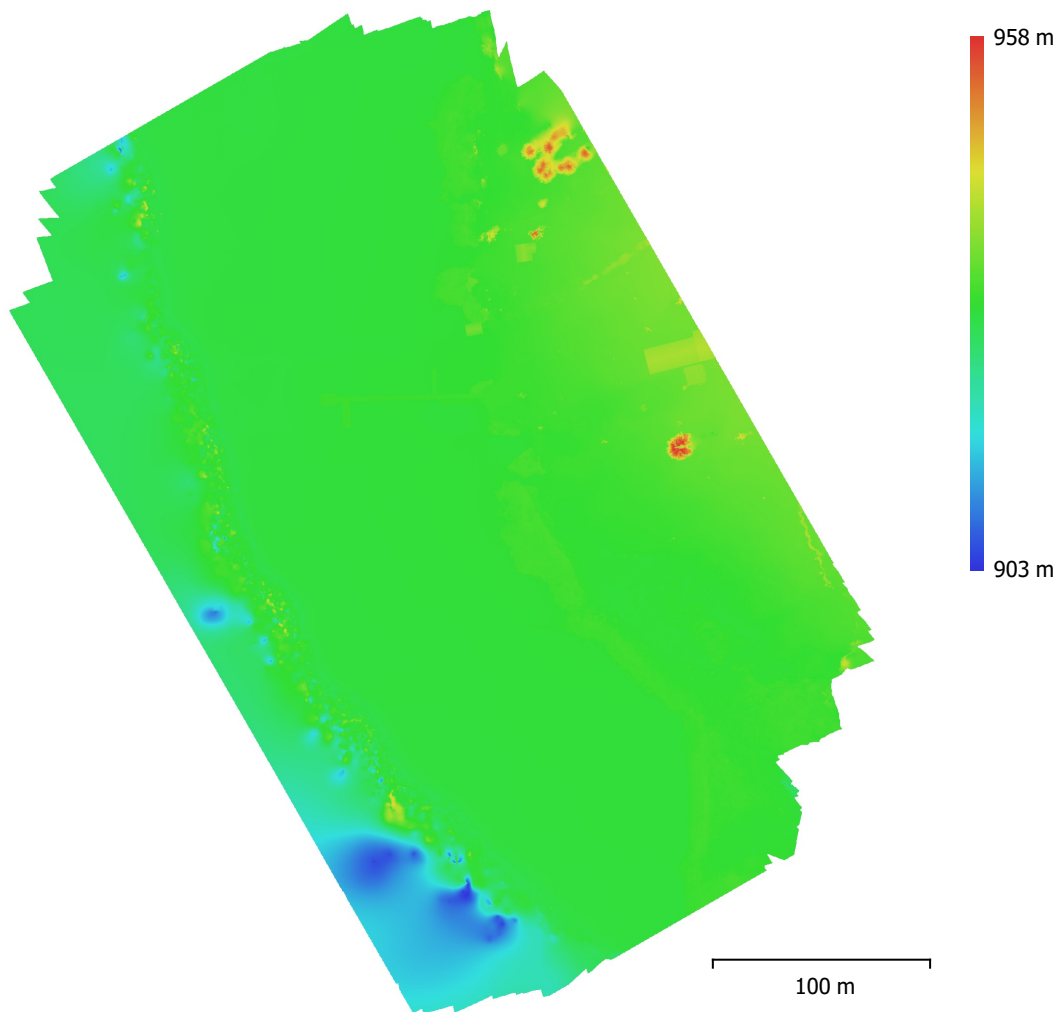


Fig. 4. Reconstructed digital elevation model.

Resolution: 2.38 cm/pix  
Point density: 0.176 points/cm<sup>2</sup>

# Processing Parameters

## General

Cameras	1404
Aligned cameras	1403
Markers	17

## Shapes

Polygons	1403
Coordinate system	MGI / Austria GK Central (EPSG::31255)
Rotation angles	Yaw, Pitch, Roll

## Point Cloud

Points	684,359 of 800,433
RMS reprojection error	0.187182 (1.30765 pix)
Max reprojection error	0.568176 (52.5855 pix)
Mean key point size	6.46658 pix
Point colors	3 bands, uint8
Key points	No
Average tie point multiplicity	6.69726

## Alignment parameters

Accuracy	High
Generic preselection	Yes
Key point limit	40,000
Tie point limit	4,000
Adaptive camera model fitting	No
Matching time	16 hours 55 minutes
Alignment time	43 minutes 29 seconds
Software version	1.5.5.9097
File size	99.93 MB

## Depth Maps

Count	1333
-------	------

## Depth maps generation parameters

Quality	High
Filtering mode	Mild
Processing time	18 hours 9 minutes
Software version	1.5.5.9097
File size	6.31 GB

## Dense Point Cloud

Points	209,246,129
Point colors	3 bands, uint8

## Depth maps generation parameters

Quality	High
Filtering mode	Mild
Processing time	18 hours 9 minutes

## Dense cloud generation parameters

Processing time	13 hours 4 minutes
Software version	1.5.5.9097
File size	2.72 GB

## DEM

Size	19,125 x 21,732
Coordinate system	MGI / Austria GK Central (EPSG::31255)

## Reconstruction parameters

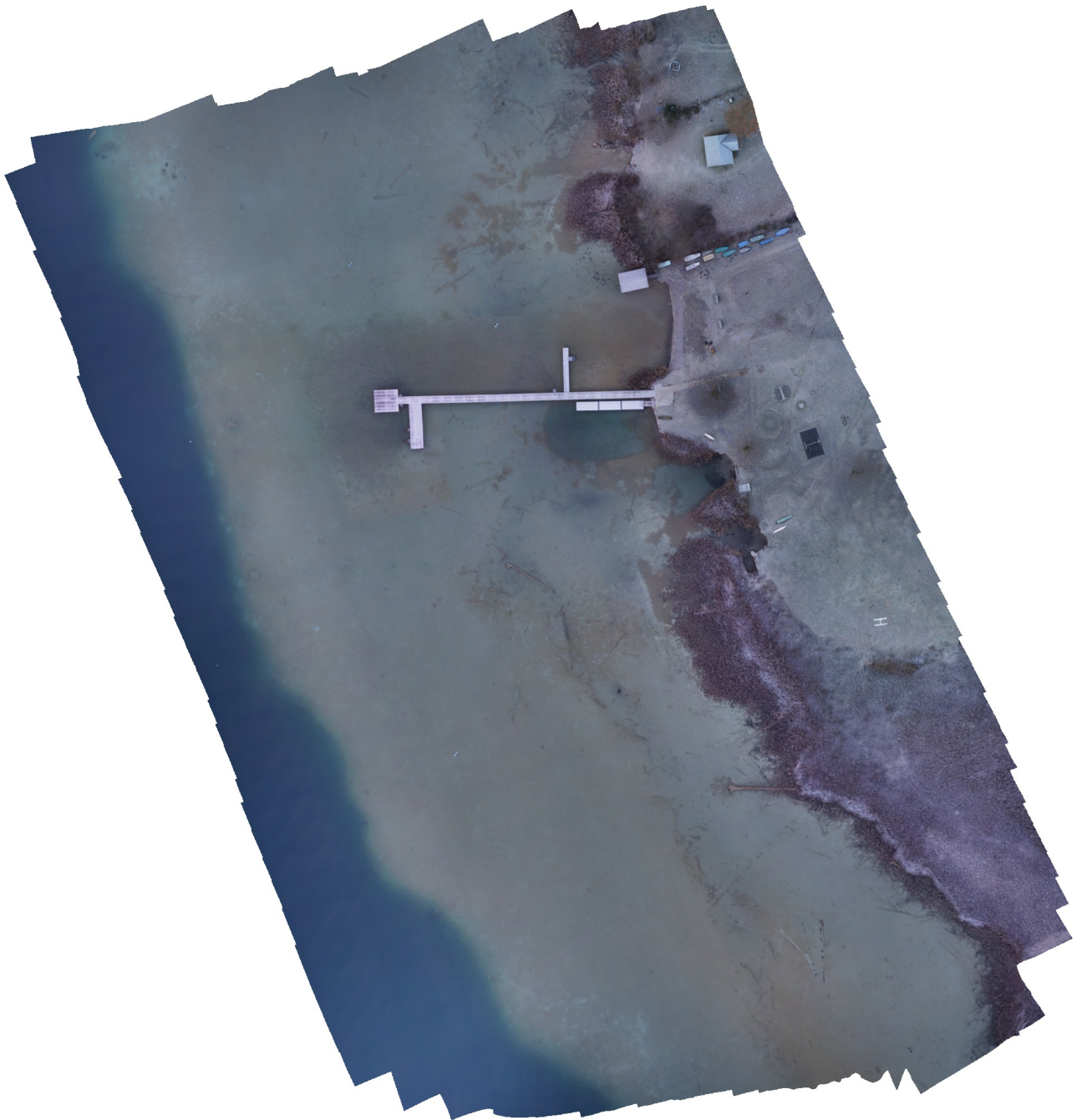
Source data	Dense cloud
Interpolation	Enabled

Processing time	9 minutes 22 seconds
Software version	1.5.5.9097
File size	605.12 MB
<b>Orthomosaic</b>	
Size	19,928 x 23,080
Coordinate system	MGI / Austria GK Central (EPSG::31255)
Colors	3 bands, uint8
<b>Reconstruction parameters</b>	
Blending mode	Mosaic
Surface	DEM
Enable hole filling	Yes
Processing time	43 minutes 13 seconds
Memory usage	4.06 GB
Software version	1.6.5.11249
File size	7.03 GB
<b>System</b>	
Software name	Agisoft Metashape Professional
Software version	1.6.5 build 11249
OS	Windows 64 bit
RAM	511.87 GB
CPU	Intel(R) Xeon(R) CPU E5-2620 v4 @ 2.10GHz
GPU(s)	Tesla P100-PCI-E-16GB

# Appendix J: Agisoft Metashape Professional Processing Report PN

PN - Pentacam nadir Photos

18 January 2021



# Survey Data

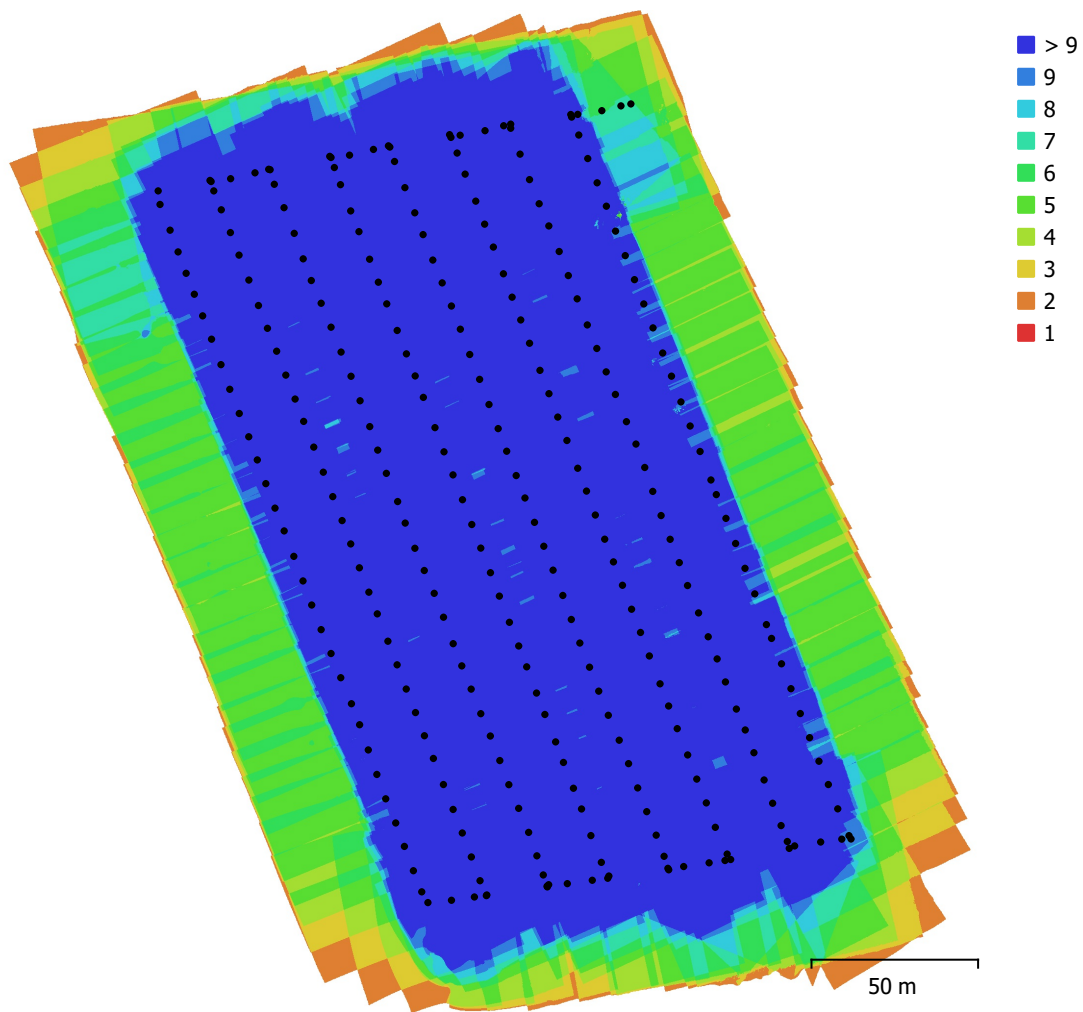


Fig. 1. Camera locations and image overlap.

Number of images:	289	Camera stations:	289
Flying altitude:	92.4 m	Tie points:	238,556
Ground resolution:	1.07 cm/pix	Projections:	1,006,588
Coverage area:	0.057 km <sup>2</sup>	Reprojection error:	0.934 pix

Camera Model	Resolution	Focal Length	Pixel Size	Precalibrated
ILCE-QX1	5456 x 3632	35 mm	4.25 x 4.25 μm	No

Table 1. Cameras.

# Camera Calibration

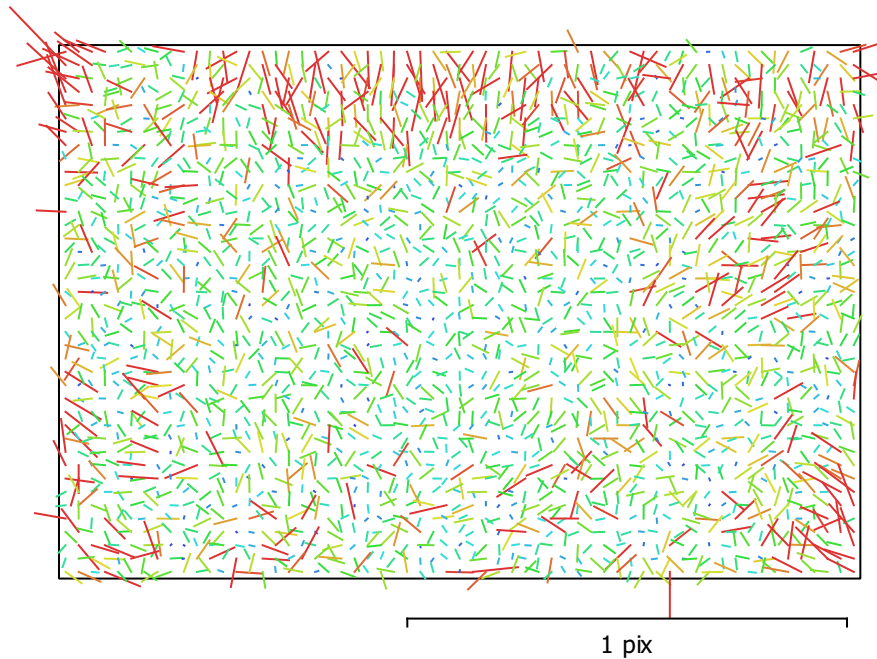


Fig. 2. Image residuals for ILCE-QX1.

## ILCE-QX1

289 images

Type  
Frame

Resolution  
**5456 x 3632**

Focal Length  
**35 mm**

Pixel Size  
**4.25 x 4.25  $\mu\text{m}$**

	Value	Error	F	Cx	Cy	K1	K2	K3	P1	P2
<b>F</b>	<b>8510.65</b>	1.9	1.00	0.60	0.85	-0.15	0.05	0.09	-0.06	-0.11
<b>Cx</b>	<b>-22.6409</b>	0.22		1.00	0.52	-0.06	-0.01	0.10	0.31	-0.01
<b>Cy</b>	<b>22.8795</b>	0.32			1.00	-0.11	0.04	0.07	-0.02	0.05
<b>K1</b>	<b>-0.0544572</b>	0.00014				1.00	-0.93	0.86	0.14	0.18
<b>K2</b>	<b>0.0921716</b>	0.0021					1.00	-0.97	-0.05	0.01
<b>K3</b>	<b>0.727639</b>	0.0098						1.00	0.03	-0.03
<b>P1</b>	<b>-0.000963134</b>	4.2e-06							1.00	0.33
<b>P2</b>	<b>0.000912283</b>	4.3e-06								1.00

Table 2. Calibration coefficients and correlation matrix.

# Ground Control Points

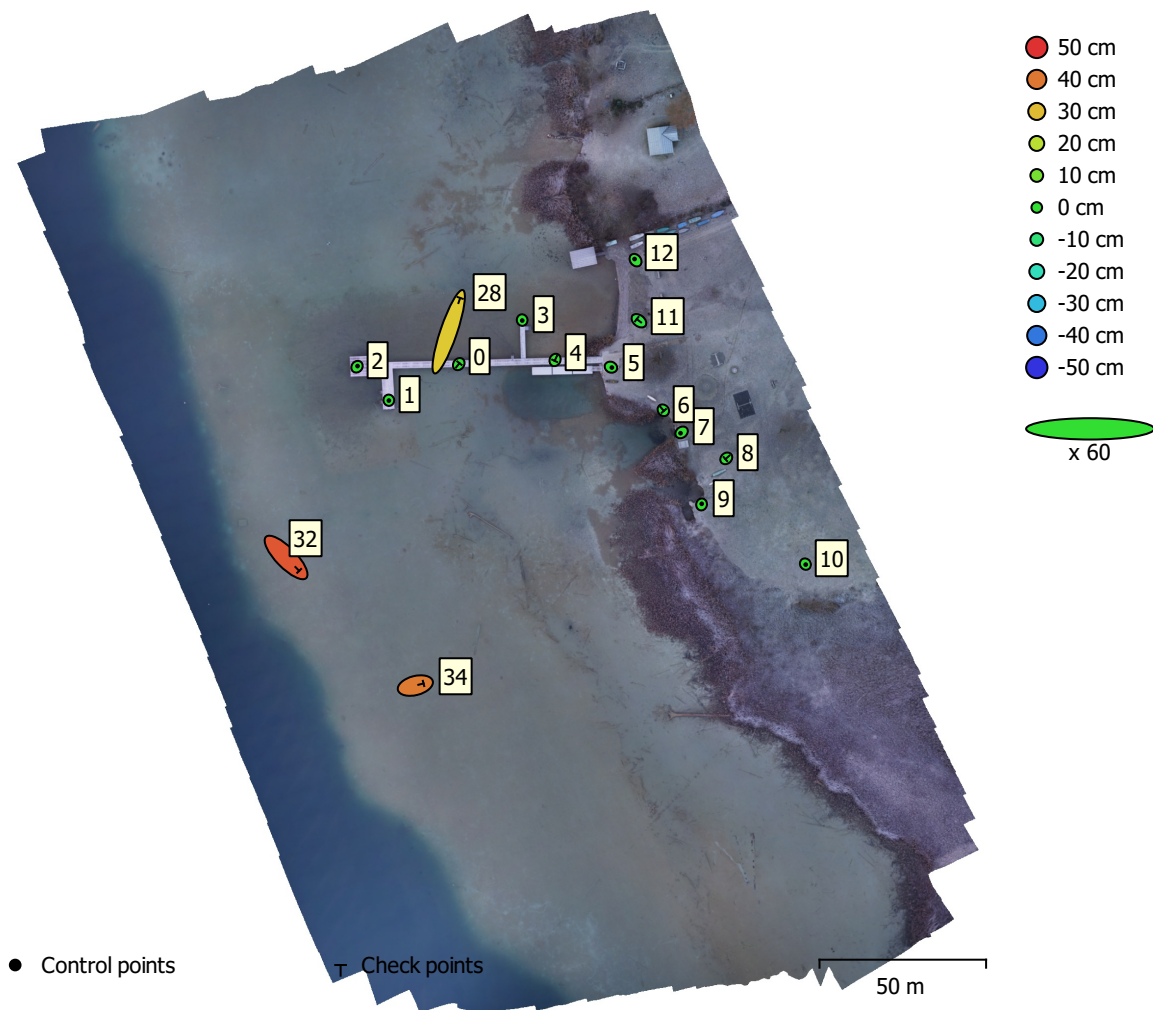


Fig. 3. GCP locations and error estimates.

Z error is represented by ellipse color. X,Y errors are represented by ellipse shape.

Estimated GCP locations are marked with a dot or crossing.

Count	X error (cm)	Y error (cm)	Z error (cm)	XY error (cm)	Total (cm)
8	0.646517	0.666477	0.223966	0.928534	0.955163

Table 3. Control points RMSE.

X - Easting, Y - Northing, Z - Altitude.

Count	X error (cm)	Y error (cm)	Z error (cm)	XY error (cm)	Total (cm)
8	6.86162	12.893	23.2842	14.6052	27.4857

Table 4. Check points RMSE.

X - Easting, Y - Northing, Z - Altitude.

<b>Label</b>	<b>X error (cm)</b>	<b>Y error (cm)</b>	<b>Z error (cm)</b>	<b>Total (cm)</b>	<b>Image (pix)</b>
1	0.0557321	-0.32881	-0.0844246	0.34402	0.364 (18)
2	0.529191	0.64231	0.146049	0.844948	0.488 (18)
3	0.0704905	-0.454296	0.0546297	0.462967	0.595 (15)
5	0.918821	-0.384683	-0.551268	1.13847	0.521 (15)
7	-1.08448	-0.815004	0.100912	1.36033	0.502 (15)
9	0.154793	0.65212	0.140379	0.684783	0.479 (15)
10	0.311659	-0.478031	0.00387322	0.570666	0.264 (4)
12	-0.956212	1.16639	0.189851	1.52015	0.443 (9)
<b>Total</b>	<b>0.646517</b>	<b>0.666477</b>	<b>0.223966</b>	<b>0.955163</b>	<b>0.482</b>

Table 5. Control points.  
X - Easting, Y - Northing, Z - Altitude.

<b>Label</b>	<b>X error (cm)</b>	<b>Y error (cm)</b>	<b>Z error (cm)</b>	<b>Total (cm)</b>	<b>Image (pix)</b>
0	0.71482	0.892935	-0.184176	1.15854	0.736 (14)
4	-0.414128	-0.871671	0.738642	1.21528	0.850 (15)
6	0.550283	-0.640373	-0.199195	0.867506	0.442 (15)
8	-0.853411	-0.744727	0.0457131	1.13359	0.579 (10)
11	-2.12385	1.64662	-2.28484	3.52741	0.838 (15)
28	11.4749	33.7825	27.963	45.3306	0.420 (2)
32	13.1024	-13.3756	44.7237	48.4849	0.457 (10)
34	8.19049	2.10802	39.3605	40.2589	0.454 (15)
<b>Total</b>	<b>6.86162</b>	<b>12.893</b>	<b>23.2842</b>	<b>27.4857</b>	<b>0.652</b>

Table 6. Check points.  
X - Easting, Y - Northing, Z - Altitude.

# Digital Elevation Model

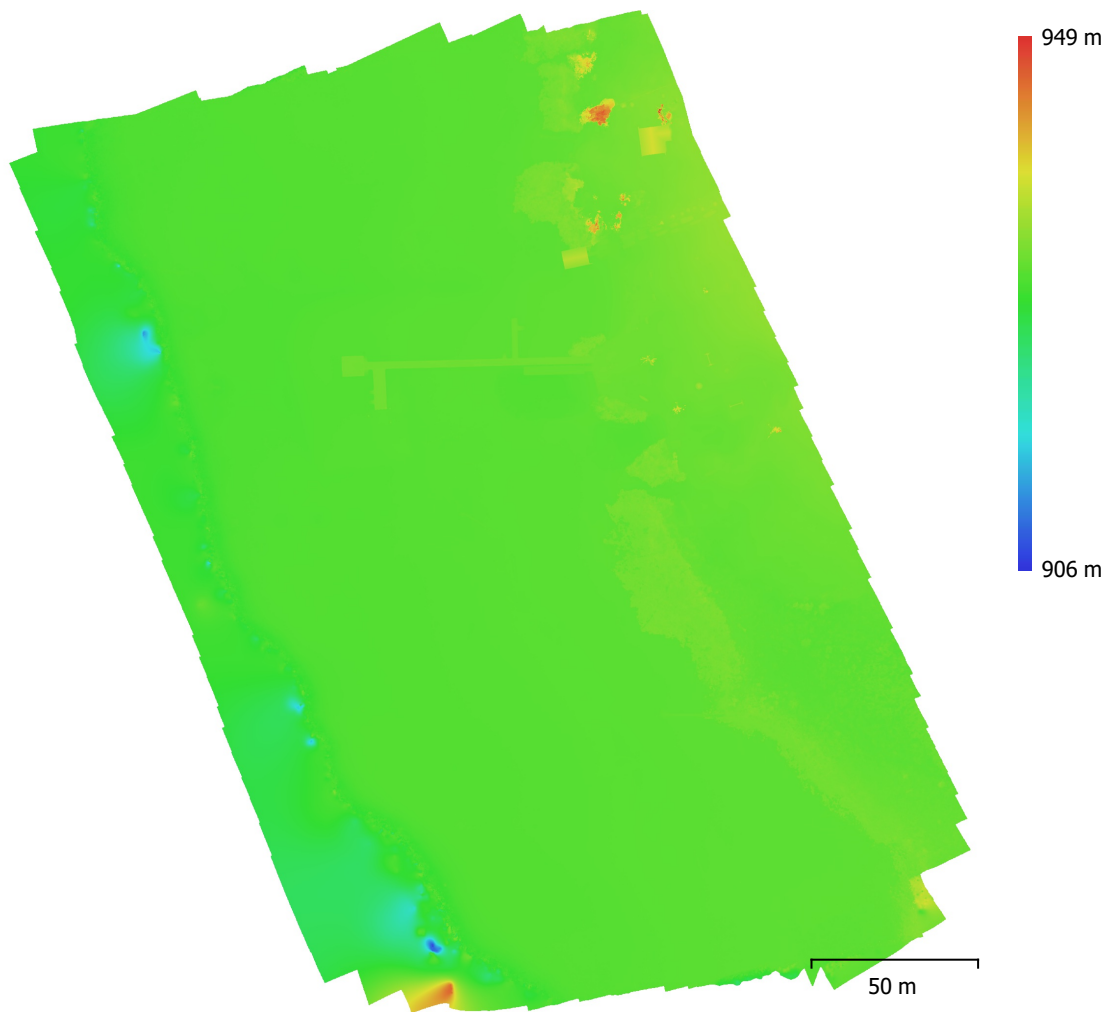


Fig. 4. Reconstructed digital elevation model.

Resolution: 2.13 cm/pix  
Point density: 0.22 points/cm<sup>2</sup>

# Processing Parameters

## General

Cameras	289
Aligned cameras	289
Markers	17

## Shapes

Polygons	289
Coordinate system	MGI / Austria GK Central (EPSG::31255)
Rotation angles	Yaw, Pitch, Roll

## Point Cloud

Points	238,556 of 257,872
RMS reprojection error	0.149665 (0.934432 pix)
Max reprojection error	0.542225 (21.5063 pix)
Mean key point size	6.00365 pix
Point colors	3 bands, uint8
Key points	No
Average tie point multiplicity	4.42966

## Alignment parameters

Accuracy	High
Generic preselection	Yes
Key point limit	40,000
Tie point limit	4,000
Adaptive camera model fitting	No
Matching time	5 minutes 35 seconds
Alignment time	3 minutes 30 seconds

## Optimization parameters

Parameters	f, cx, cy, k1-k3, p1, p2
Adaptive camera model fitting	No
Optimization time	12 seconds
Software version	1.5.5.9097
File size	23.67 MB

## Depth Maps

Count	289
-------	-----

## Depth maps generation parameters

Quality	High
Filtering mode	Mild
Processing time	49 minutes 36 seconds
Software version	1.5.5.9097
File size	1.53 GB

## Dense Point Cloud

Points	174,765,512
Point colors	3 bands, uint8

## Depth maps generation parameters

Quality	High
Filtering mode	Mild
Processing time	49 minutes 36 seconds

## Dense cloud generation parameters

Processing time	1 hours 2 minutes
Software version	1.5.5.9097
File size	2.13 GB

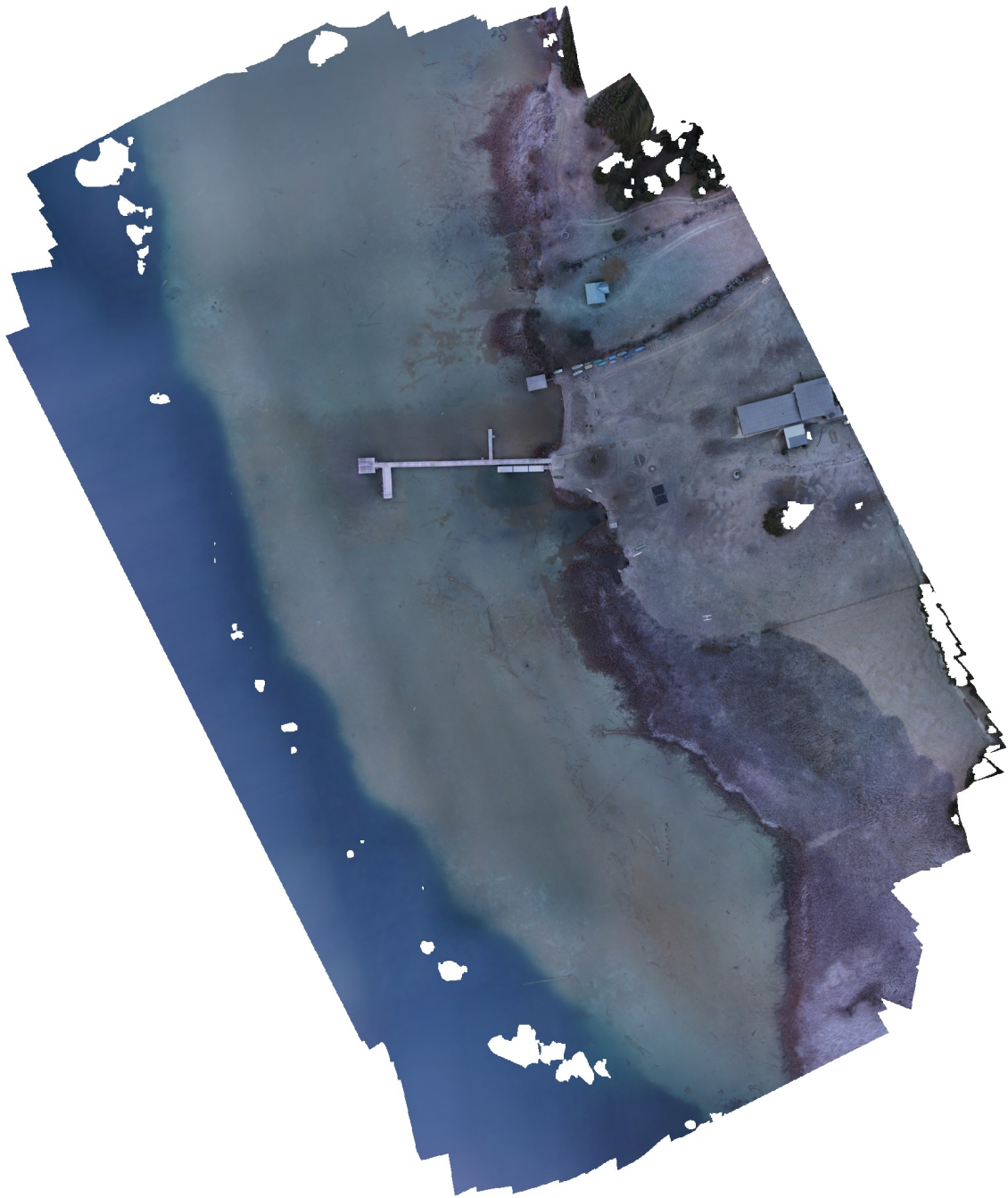
## DEM

Size	20,233 x 23,496
------	-----------------

Coordinate system	MGI / Austria GK Central (EPSG::31255)
<b>Reconstruction parameters</b>	
Source data	Dense cloud
Interpolation	Enabled
Processing time	6 minutes 14 seconds
Software version	1.5.5.9097
File size	374.65 MB
<b>Orthomosaic</b>	
Size	14,420 x 15,050
Coordinate system	MGI / Austria GK Central (EPSG::31255)
Colors	3 bands, uint8
<b>Reconstruction parameters</b>	
Blending mode	Mosaic
Surface	DEM
Enable hole filling	Yes
Processing time	6 minutes 53 seconds
Memory usage	2.32 GB
Software version	1.6.5.11249
File size	1.15 GB
<b>System</b>	
Software name	Agisoft Metashape Professional
Software version	1.6.5 build 11249
OS	Windows 64 bit
RAM	511.87 GB
CPU	Intel(R) Xeon(R) CPU E5-2620 v4 @ 2.10GHz
GPU(s)	Tesla P100-PCI-E-16GB

# Appendix K: Agisoft Metashape Professional Processing Report PO

PO - Pentacam oblique Photos  
18 January 2021



# Survey Data

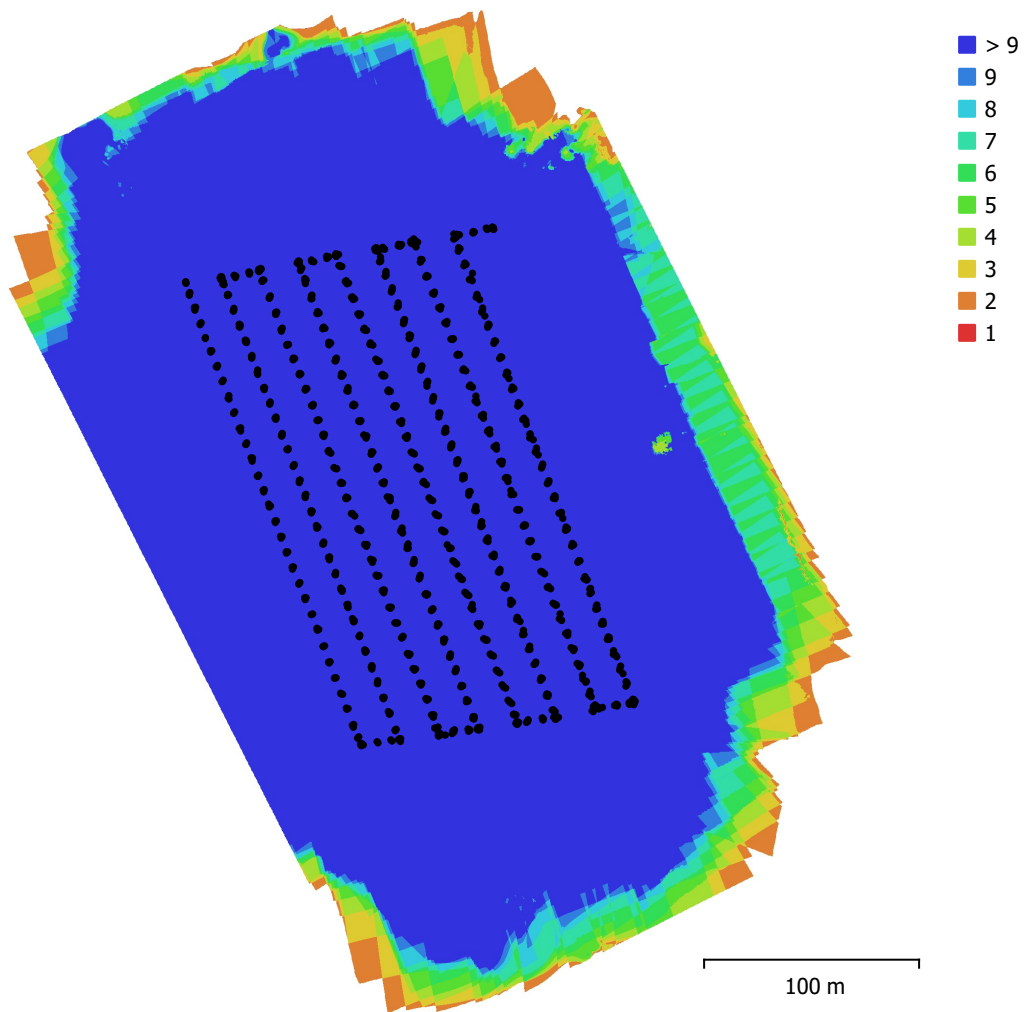


Fig. 1. Camera locations and image overlap.

Number of images:	1,108	Camera stations:	1,107
Flying altitude:	104 m	Tie points:	589,794
Ground resolution:	1.23 cm/pix	Projections:	2,880,360
Coverage area:	0.115 km <sup>2</sup>	Reprojection error:	1.27 pix

Camera Model	Resolution	Focal Length	Pixel Size	Precalibrated
ILCE-QX1	5456 x 3632	35 mm	4.25 x 4.25 $\mu$ m	No

Table 1. Cameras.

# Camera Calibration

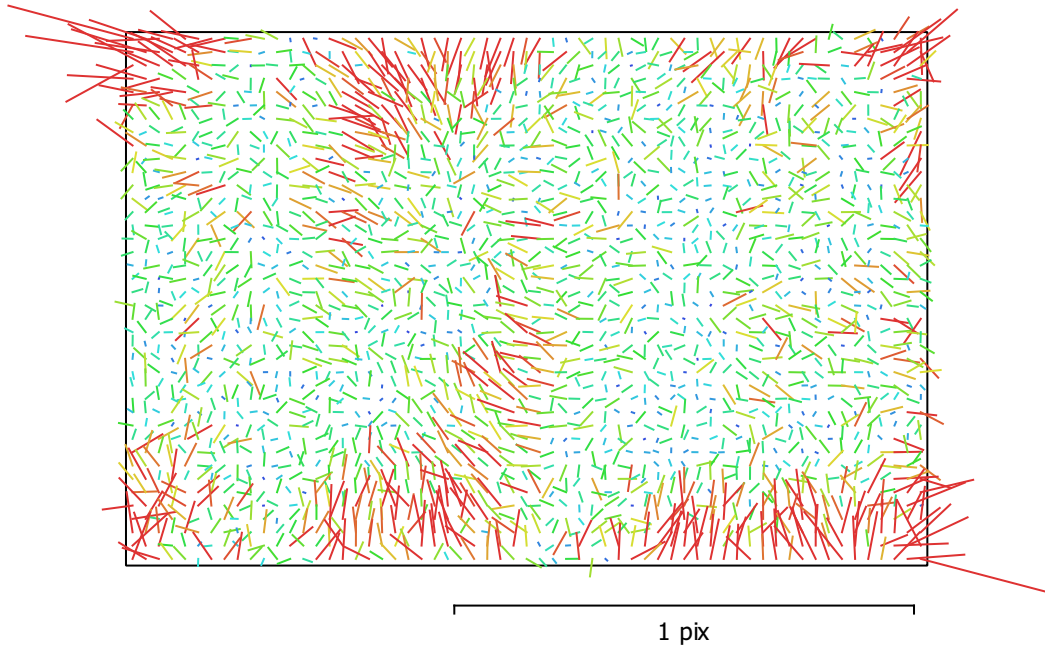


Fig. 2. Image residuals for ILCE-QX1.

## ILCE-QX1

1108 images

Type	Resolution	Focal Length	Pixel Size
<b>Frame</b>	<b>5456 x 3632</b>	<b>35 mm</b>	<b>4.25 x 4.25 <math>\mu</math>m</b>
F:	8501.26		
Cx:	-20.688	B1:	0
Cy:	13.7937	B2:	0
K1:	-0.0562911	P1:	-0.000276418
K2:	0.059549	P2:	-0.000164248
K3:	0.792929	P3:	0
K4:	0	P4:	0

# Ground Control Points

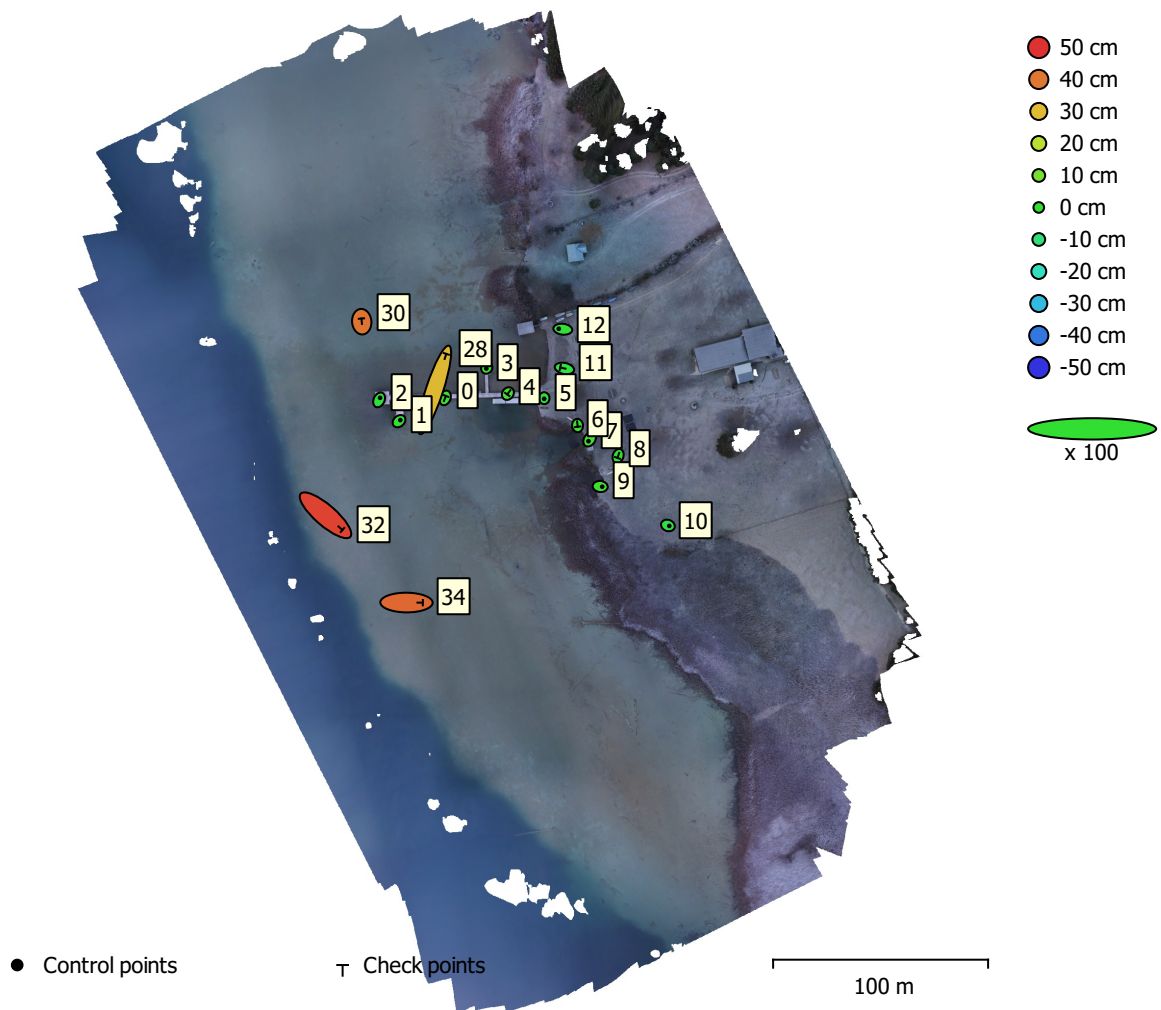


Fig. 3. GCP locations and error estimates.

Z error is represented by ellipse color. X,Y errors are represented by ellipse shape.

Estimated GCP locations are marked with a dot or crossing.

Count	X error (cm)	Y error (cm)	Z error (cm)	XY error (cm)	Total (cm)
8	1.6911	1.04114	1.6073	1.9859	2.55484

Table 2. Control points RMSE.

X - Easting, Y - Northing, Z - Altitude.

Count	X error (cm)	Y error (cm)	Z error (cm)	XY error (cm)	Total (cm)
9	8.28233	12.1537	27.1379	14.7075	30.8671

Table 3. Check points RMSE.

X - Easting, Y - Northing, Z - Altitude.

<b>Label</b>	<b>X error (cm)</b>	<b>Y error (cm)</b>	<b>Z error (cm)</b>	<b>Total (cm)</b>	<b>Image (pix)</b>
1	1.19242	1.01872	0.308135	1.59831	1.284 (71)
2	0.925208	1.93649	-1.26928	2.4934	1.795 (69)
3	-0.370948	-0.44101	0.539766	0.789582	1.298 (69)
5	0.00942271	-0.563623	-0.201892	0.598765	1.032 (70)
7	-1.11832	-1.72564	2.5048	3.24075	0.656 (62)
9	1.87094	-0.19243	1.93489	2.69838	0.490 (59)
10	1.25214	-0.43845	-2.72335	3.02931	0.785 (46)
12	-3.76086	0.405944	-1.09306	3.93747	0.403 (44)
<b>Total</b>	<b>1.6911</b>	<b>1.04114</b>	<b>1.6073</b>	<b>2.55484</b>	<b>1.112</b>

Table 4. Control points.  
X - Easting, Y - Northing, Z - Altitude.

<b>Label</b>	<b>X error (cm)</b>	<b>Y error (cm)</b>	<b>Z error (cm)</b>	<b>Total (cm)</b>	<b>Image (pix)</b>
0	0.685335	1.79828	1.37177	2.36332	1.530 (81)
4	-0.597375	-0.812585	2.61363	2.80147	1.035 (72)
6	0.124386	-1.15103	1.18648	1.65773	0.645 (60)
8	-0.601792	-1.71163	-0.132527	1.81917	0.713 (44)
11	-3.92222	0.840344	-1.96022	4.46458	0.421 (45)
28	10.956	33.5482	30.5561	46.6817	0.765 (49)
30	-0.26528	2.90734	40.395	40.5004	1.189 (34)
32	15.7959	-13.6608	47.5761	51.9578	1.026 (64)
34	15.2043	-0.108716	42.2529	44.9054	1.163 (82)
<b>Total</b>	<b>8.28233</b>	<b>12.1537</b>	<b>27.1379</b>	<b>30.8671</b>	<b>1.043</b>

Table 5. Check points.  
X - Easting, Y - Northing, Z - Altitude.

# Digital Elevation Model

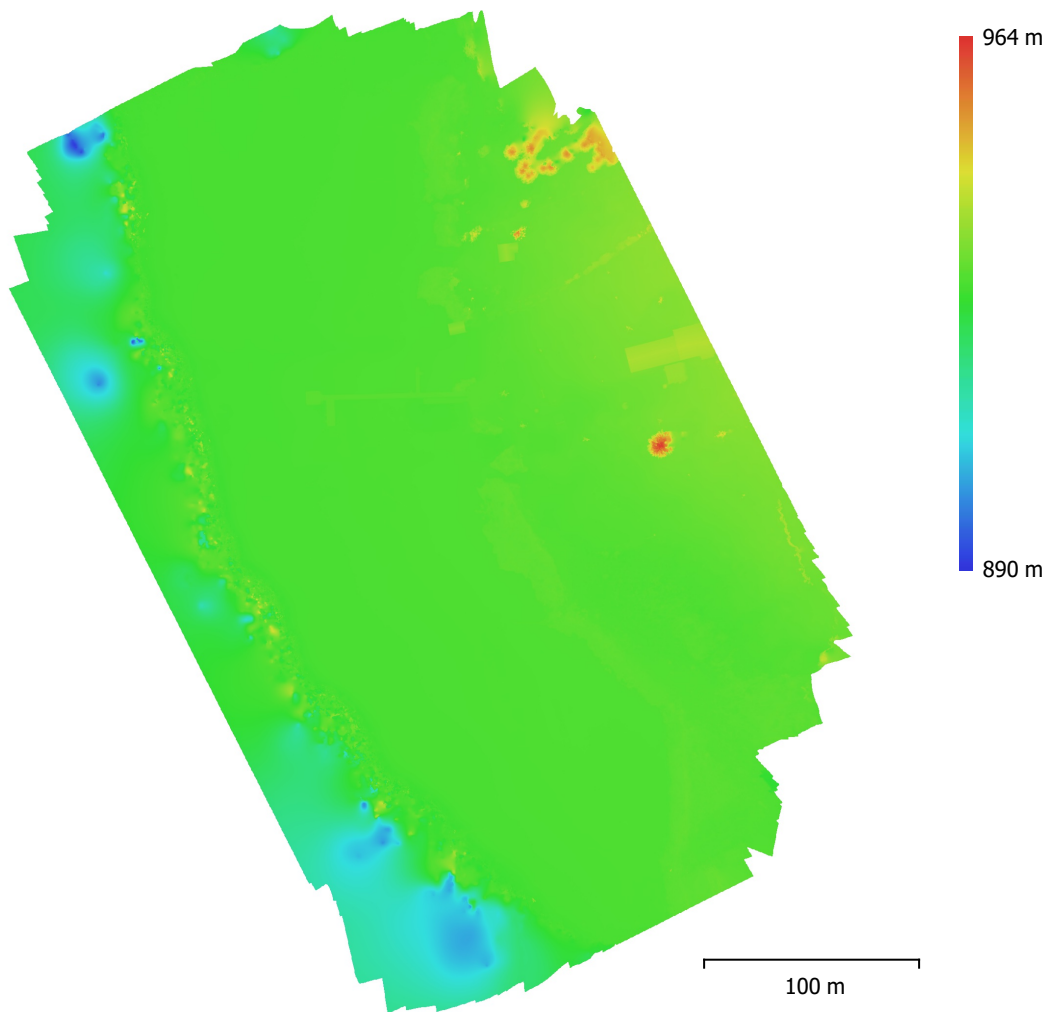


Fig. 4. Reconstructed digital elevation model.

Resolution: 2.45 cm/pix  
Point density: 0.166 points/cm<sup>2</sup>

# Processing Parameters

## General

Cameras	1108
Aligned cameras	1107
Markers	17
Coordinate system	MGI / Austria GK Central (EPSG::31255)
Rotation angles	Yaw, Pitch, Roll

## Point Cloud

Points	589,794 of 654,628
RMS reprojection error	0.181533 (1.27415 pix)
Max reprojection error	0.548461 (37.3149 pix)
Mean key point size	6.46354 pix
Point colors	3 bands, uint8
Key points	No
Average tie point multiplicity	6.23608

## Alignment parameters

Accuracy	High
Generic preselection	Yes
Key point limit	40,000
Tie point limit	4,000
Adaptive camera model fitting	No
Matching time	16 hours 55 minutes
Alignment time	21 minutes 29 seconds
Software version	1.5.5.9097
File size	77.81 MB

## Depth Maps

Count	1068
-------	------

## Depth maps generation parameters

Quality	High
Filtering mode	Mild
Processing time	12 hours 33 minutes
Software version	1.5.5.9097
File size	5.07 GB

## Dense Point Cloud

Points	201,010,844
Point colors	3 bands, uint8

## Depth maps generation parameters

Quality	High
Filtering mode	Mild
Processing time	12 hours 33 minutes

## Dense cloud generation parameters

Processing time	10 hours 3 minutes
Software version	1.5.5.9097
File size	2.61 GB

## DEM

Size	18,576 x 21,706
Coordinate system	MGI / Austria GK Central (EPSG::31255)

## Reconstruction parameters

Source data	Dense cloud
Interpolation	Enabled
Processing time	8 minutes 33 seconds
Memory usage	316.19 MB

Software version	1.6.5.11249
File size	604.06 MB
<b>Orthomosaic</b>	
Size	19,623 x 23,326
Coordinate system	MGI / Austria GK Central (EPSG::31255)
Colors	3 bands, uint8
<b>Reconstruction parameters</b>	
Blending mode	Mosaic
Surface	DEM
Enable hole filling	Yes
Processing time	35 minutes 51 seconds
Memory usage	3.37 GB
Software version	1.6.5.11249
File size	6.02 GB
<b>System</b>	
Software name	Agisoft Metashape Professional
Software version	1.6.5 build 11249
OS	Windows 64 bit
RAM	511.87 GB
CPU	Intel(R) Xeon(R) CPU E5-2620 v4 @ 2.10GHz
GPU(s)	Tesla P100-PCI-E-16GB